Simulation of mechanical properties of carbon nanotubes and their interaction with polymers

Mingjun Yang

A thesis submitted for the degree of Doctor of Philosophy.
The University of Edinburgh.
September 2005

Abstract

Carbon nanotubes are fullerene-related structures, which are entirely composed of carbon atoms. We present molecular mechanics (MM) simulations of mechanical properties of single-walled carbon nanotubes (SWNT) and molecular dynamics (MD) simulations of interactions between polymers and SWNT.

A SWNT is usually thought of as a perfect graphene sheet wrapped up into a cylinder. However, in practical applications defects on SWNT are very common. In our study, a molecular mechanics approach is applied to study the mechanical properties of "zigzag" and "armchair" SWNT with or without defects under tensile and compressive load. Three kinds of defects are studied: defects caused by chemical functionalization, topological defects, and vacancies. In our study, the influence of defects on mechanical properties of SWNT is investigated. Our study shows that the elastic modulus of SWNT is slightly influenced by these defects, while the buckling and fracture strength are greatly affected. The buckling strength of all the SWNT deteriorates with increasing defect concentration. The defects greatly decrease the fracture strength of SWNT, and we use the Weibull strength distribution to describe the fracture data of defected SWNT. Furthermore, a weakest link model is used to bridge the scale gap between the length of SWNT in simulations and that of SWNT in experiments.

Carbon nanotubes have exceptional mechanical properties and large aspect ratio, which make them ideal candidates as ultra-strong reinforcers for composites. Good interfacial binding is a necessary condition for successful load transfer across the interface between carbon nanotubes and polymer matrix. A series of MD simulations of the interaction between polymers (PS, PPA, PmPV and PPV) and SWNT are carried out, and the results indicate that the interaction between carbon nanotubes and polymers is strongly influenced by the specific monomer structure. Among the four polymers, the intermolecular interactions are strongest for conjugated polymers with aromatic rings on the polymer backbone, as these rings are able to align parallel to the nanotube surface and thereby provide strong interfacial adhesion. In the presence of well-separated SWNT, different polymer chains get disentangled and align along the SWNT to cover the nanotube surface ("wrapping"). This phenomenon is most pronounced for PmPV, which combines certain flexibility in the backbone structure, flexible side-chains and strong interaction with the nanotube surface.

Declaration of originality

I hereby declare that unless stated otherwise in the text, the research recorded in this thesis and the thesis itself was composed and originated entirely by myself in the Institute for Materials and Processes, School of Engineering and Electronics & Centre for Materials Science and Engineering, The University of Edinburgh. Some of the material used in this thesis has been published in the following paper:

M. Yang, V. Koutsos, M. Zaiser, *Interaction between polymers and carbon nanotubes - a molecular dynamics study*, Journal of Physical Chemistry B, 109, 2005, 10009-10014

Mingjun Yang

Acknowledgments

This work was conducted on an Overseas Research Students Award Scheme (ORSAS) scholarship from Universities UK, with additional financial support by the School of Engineering and Electronics, University of Edinburgh. I am grateful to both organisations for their support.

I would like to thank my supervisors, Michael Zaiser and Vasileios Koutsos, for their advice, help and encouragement over the last three years.

I would also like to thank Mark J Biggs and Dusan Djurdjevic for providing computational facilities, and the administrative help of Avril Davies has been invaluable.

Most of all I would like to thank my wife, Ying Yuan. Her love and companionship brighten every day of my life.

Contents

Declaration of originality . . . iii
Acknowledgments . . . iv
Contents . . . v
List of figures . . . viii
List of tables . . . xi
Acronyms and abbreviations . . . xii

1 Introduction **1**
1.1 Carbon nanotubes . . . 1
1.1.1 Structure of carbon nanotubes . . . 1
1.1.2 Synthesis of carbon nanotubes . . . 4
1.1.3 Mechanical properties of carbon nanotubes . . . 6
1.1.4 Applications of carbon nanotubes . . . 9
1.2 Objectives of this thesis . . . 10
1.3 Thesis overview . . . 10

2 Brief introduction to molecular mechanics and molecular dynamics **12**
2.1 Introduction . . . 12
2.2 Molecular mechanics . . . 13
2.2.1 The Born-Oppenheimer approximation . . . 13
2.2.2 Force field . . . 14
2.2.3 Energy minimisation . . . 21
2.3 Molecular dynamics . . . 25
2.3.1 Time integration algorithm . . . 25
2.3.2 Integration time step . . . 27
2.3.3 Canonical ensemble and thermostat methods . . . 27
2.4 Molecular simulation of carbon nanotubes . . . 28
2.5 Summary . . . 29

3 Young's modulus and buckling strength of SWNT with/without defects **30**
3.1 Introduction . . . 30
3.2 Simulation of SWNT under axial load . . . 30
3.2.1 Method . . . 30
3.2.2 Modified MM3 force field . . . 32
3.2.3 Potential and stress of SWNT . . . 34
3.3 Young's modulus and Poisson's ratio of SWNT . . . 36
3.3.1 Calculation of Young's modulus and Poisson's ratio of SWNT . . . 36
3.3.2 Effective longitudinal Young's modulus of SWNT . . . 37
3.3.3 Surface longitudinal Young's modulus of SWNT . . . 37
3.3.4 Poisson's ratio of SWNT . . . 38
3.4 Buckling of SWNT . . . 40
3.4.1 SWNT under compressive loading . . . 40

3.4.2 Buckling strength of SWNT 40
3.4.3 Buckling modes of SWNT under compressive load 41
3.4.4 Critical strain of SWNT buckling 45
3.5 Defects of SWNT 47
3.6 Simulation of SWNT with defects under axial load 48
3.7 Influence of defects on Young's modulus and buckling strength of SWNT . . . 49
3.7.1 Influence of defects on Young's modulus of SWNT 49
3.7.2 Influence of defects on buckling strength of SWNT 50
3.7.3 Influence of number of defects 51
3.8 Summary 52

4 Size effect in tensile fracture of SWNT with defects 53
4.1 Introduction 53
4.2 Models 53
4.3 Modified Brenner's potential 54
4.3.1 Potential energy and stress of SWNT with original Brenner's potential . 54
4.3.2 Bond length and angle of SWNT with original Brenner's potential . . . 55
4.3.3 Potential energy and stress of SWNT with modified Brenner's potential 56
4.3.4 The influence of cut-off on potential energy and stress of SWNT 57
4.3.5 Bond length and angle of SWNT with modified Brenner's potential . . 58
4.4 Tensile failure of SWNT with/without defect(s) 59
4.4.1 Elongation of SWNT 59
4.4.2 Fracture strength of SWNT with defects 59
4.4.3 Fracture strength distribution of simulated SWNT 60
4.5 Weibull distribution fitting of fracture strength of SWNT 61
4.5.1 Weibull strength distribution 61
4.5.2 Determination of the parameters in Weibull strength distribution 61
4.5.3 Weibull distribution fitting of SWNT strength from simulations 62
4.6 Size effect of SWNT fracture strength 66
4.6.1 Weakest link model 66
4.6.2 Size effect in fracture strength of defected carbon nanotubes 67
4.7 Summary 69

5 MD simulations of interactions between SWNT and polymers 70
5.1 Introduction 70
5.2 Interfacial interaction in polymer composites 70
5.3 Simulation method 71
5.3.1 Model 71
5.3.2 Parameters and thermostat algorithm for MD simulations 72
5.3.3 Boundary conditions 76
5.4 Interaction between SWNT and polymers 77
5.4.1 Simulation of interaction between SWNT and polymers 77
5.4.2 Temperature dependence of the intermolecular interactions 78
5.4.3 Influence of SWNT diameter on the intermolecular interactions 78
5.5 Morphology of polymers on SWNT surface 79
5.5.1 Dihedral angles between graphene surface and polymer aromatic rings . 80
5.5.2 Dihedral between surface of SWNT and that of polymer aromatic rings 83

5.5.3 The change of mean radius of polymers 84
5.6 "Wrapping" of SWNT by polymers 86
5.6.1 Simulation of interaction between SWNT and aggregated polymers . . 86
5.6.2 Polymer wrapping of SWNT 87
5.6.3 Intermolecular interaction between SWNT and aggregated polymers . . 87
5.7 Summary 87

6 Conclusions **90**
6.1 Summary 90
6.1.1 Mechanical properties of SWNT with/without defects 90
6.1.2 Size dependence of fracture strength of SWNT with defects 90
6.1.3 Interaction between SWNT and polymers 91
6.2 Future work 91
6.2.1 Computer simulation of full-size defected carbon nanotubes 91
6.2.2 Computer simulation of carbon nanotubes dispersion 92

A Ensembles and ensemble averages in MD simulations **93**
A.1 Ensembles 93
A.2 Ensemble averages in MD simulations 94

B Thermostat algorithms of molecular dynamics **96**
B.1 Andersen thermostat 96
B.2 Berendsen thermostat 97
B.3 Nose-Hoover thermostat 97

C Molecular simulation packages **100**
C.1 The TINKER simulation package 100
C.2 Brenner's code 103

References **105**

List of figures

1.1 SWNT and MWNT structures . . . 2
1.2 Definition of roll-up vector as linear combinations of base vectors **a** and **b** . . . 2
1.3 Roll-up vectors for zigzag and armchair SWNT . . . 3
1.4 Structure of SWNT (a): zigzag SWNT (b): armchair SWNT . . . 4
1.5 Fracture of SWNT, this image is courtesy of MF Yu *et al* [33] . . . 8
1.6 Buckling of a carbon nanotube, this image is courtesy of MR Falvo *et al* [37] . 9

2.1 Bond potential function E_{bond} . . . 15
2.2 Bond angle potential function E_{angle} . . . 15
2.3 Dihedral angle potential function E_{dih} . . . 15

3.1 Computation scheme for SWNT elongation and compression . . . 31
3.2 SWNT under axial load . . . 31
3.3 The relationship between l_0 and C-C bond length of graphite . . . 32
3.4 Bond lengths and bond angles around a representative atom: (a) for armchair SWNT and (b) for zigzag SWNT . . . 33
3.5 Bond lengths around a representative atom: (a) for armchair (n,n) nanotube and (b) for zigzag (n,0) nanotube. . . . 34
3.6 Bond angles around a representative atom: (a) for armchair (n,n) SWNT and (b) for zigzag (n,0) SWNT. . . . 34
3.7 Potential energy of SWNT under axial load: (a) elongation and (b) compression 35
3.8 Stress of SWNT under axial load: (a) elongation and (b) compression . . . 35
3.9 Effective longitudinal Young's modulus of SWNT . . . 37
3.10 Surface longitudinal Young's modulus of SWNT . . . 38
3.11 Poisson's ratio of armchair (6,6) and zigzag (10,0) SWNT . . . 39
3.12 Poisson's ratio of SWNT . . . 39
3.13 Buckling of SWNT . . . 40
3.14 Buckling strength of SWNT . . . 41
3.15 Cross sections of SWNT . . . 42
3.16 Buckling section gyration radius of zigzag(10,0) SWNT d=7.85 Å . . . 43
3.17 Buckling section gyration radius of zigzag(25,0) SWNT d=19.6 Å . . . 43
3.18 Buckling section gyration radius of armchair (6,6) SWNT d=8.15 Å . . . 45
3.19 Critical strain of SWNT buckling . . . 46
3.20 Defects on SWNT (segment): (a) functionalization defect, (b) 5-7-7-5 defect, (c) vacancy . . . 47
3.21 The relationship between defect site and buckling site: (a) zigzag (6,0) SWNT (diameter: 4.78 Å), (b) zigzag (16,0) SWNT (diameter: 12.5 Å). . . . 48
3.22 Young's modulus of functionalized SWNT . . . 49
3.23 Young's modulus of SWNT with 5-7-7-5 defects . . . 50
3.24 Young's modulus of SWNT with vacancies . . . 50
3.25 Buckling stress of functionalized SWNT:(a) armchair SWNT, (b) zigzag SWNT 51

3.26 Buckling stress of SWNT with 5-7-7-5 defect: (a) armchair SWNT, (b) zigzag SWNT 51
3.27 Buckling stress of SWNT with vacancy: (a) armchar SWNT, (b) zigzag SWNT 52
3.28 Influence of number of defects (functionalisation defects): (a) Young's modulus, (b) buckling strength 52

4.1 Potential energy of SWNT under tensile load ((8,0) zigzag SWNT) 54
4.2 Stress of SWNT under tensile load (zigzag (8,0) SWNT) 55
4.3 Bond length and angle of SWNT 55
4.4 Bond length and bond angle under tensile load with original Brenner's potential 56
4.5 Potential energy of SWNT under tensile load with modified Brenner's potential 56
4.6 Stress of SWNT under tensile load with modified Brenner's potential 57
4.7 Potential of SWNT under elongation with different cut-off distance 57
4.8 Stress of SWNT under elongation with different cut-off distance 58
4.9 Bond length and bond angle under tensile load with modified Brenner's potential 58
4.10 Defected SWNT under tensile load 59
4.11 Tensile failure of SWNT with/without defect(s) (Zigzag (8,0)) defect concentration $\approx$7.5% 59
4.12 Weibull strength distribution of SWNT with functionalization defects 63
4.13 Weibull strength distribution of SWNT with topological defects 64
4.14 Weibull strength distribution of SWNT with vacancies 65
4.15 Weakest-link model 67
4.16 normalised material strength of defected SWNT of different length: SWNT with functionalization defects contain 6.0% defects; SWNT with topological defects contain 2.0% defects; SWNT with vacancies contains 1.5% defects (The SWNT in experiment is about 10 μm long, and the fracture strength is from 13 $\sim$ 52 GPa) 69

5.1 Chemical structure of the investigated polymers 73
5.2 Potential energy of graphene and polystyrene with different thermostat algorithms: (a) graphene unstrained, (b) graphene fixed 74
5.3 Intermolecular interaction between graphene and polystyrene with different thermostat algorithms: (a) graphene unstrained, (b) graphene fixed 75
5.4 Temperature of graphene and polystyrene with different thermostat algorithms: (a) graphene unstrained, (b) graphene fixed 75
5.5 Intermolecular interaction between SWNT and polymers 77
5.6 Intermolecular interaction as a function of temperature 78
5.7 Intermolecular interaction as a function of diameter 79
5.8 PS configurations: (a) before interacting with graphene, (b) interacting with graphene 80
5.9 PmPV configurations: (a) before interacting with graphene, (b) interacting with graphene 80
5.10 Definition of the dihedral angle between the surface of graphene and the plane of a polymer aromatic ring 81
5.11 Dihedral between the surface of graphene and that of aromatic rings of polymer: (a)PS (4 repeating units, containing 4 aromatic rings), (b) PmPV (2 repeating units, containing 4 aromatic rings) 81

5.12 Dihedral distribution: (a)PS (4 repeating units, containing 4 aromatic rings), (b) PmPV (2 repeating units, containing 4 aromatic rings) 82
5.13 Dihedral distribution: (a)PS (14 repeating units, containing 14 aromatic rings), (b) PmPV (7 repeating units, containing 14 aromatic rings) 83
5.14 Probability density of dihedral: (a)PS (14 repeating units, containing 14 aromatic rings), (b) PmPV (7 repeating units, containing 14 aromatic rings) 83
5.15 Definition of the dihedral angle between the surface of a carbon nanotube and the plane of a polymer aromatic ring 84
5.16 Probability density of the dihedral between polymer aromatic ring and carbon nanotube surface 85
5.17 Change of the mean radius after the interaction with a carbon nanotube 86
5.18 MD simulation snapshots of the wrapping of a SWNT of 11.8 Å in diameter by different polymers (section view) 88
5.19 Time evolution of polymer-polymer and polymers-carbon nanotube interactions during wrapping 89

List of tables

1.1 Strength of different materials 6

2.1 MM3 force field parameter set for carbon nanotube (none torsion-stretch interaction) [53] 18
2.2 Brenner's potential parameter set for carbon [59] 20
2.3 The characteristic timescales in molecules 27

3.1 Different buckling modes of armchair SWNT under compressive load 44
3.2 Different buckling modes of ziagzag SWNT under compressive load 44

4.1 Types of samples used in simulations 53
4.2 Fracture probability of SWNT with functionalization defects 60
4.3 Fracture probability of SWNT with topological defects 60
4.4 Fracture probability of SWNT with vacancies 60
4.5 normalised materials strength and Weibull modulus of SWNT with defects . . . 62
4.6 normalised strength of SWNT with defects:SWNT with functionalization defects contain 6.0% defects; SWNT with topological defects contain 2.0% defects; SWNT with vacancies contains 1.5% defects 68

5.1 Comparison of simulations with different thermostat algorithms 76

Acronyms and abbreviations

AFM	Atomic force microscopy
CVD	Chemical vapour deposition
MD	Molecular dynamics
MM	Molecular mechanics
MWNT	Multi-walled carbon nanotube
NMR	Nuclear magnetic resonance
REBO	Reactive empirical bond order
RMS	Root-mean-square
STM	Scanning tunnelling microscopy
STS	Scanning tunnelling spectroscopy
SWNT	Single-walled carbon nanotube
TEM	Transmission electron microscopy

Chapter 1
Introduction

Carbon nanotubes are particularly important because of their great strength, and among the carbon nanotubes there is a subset that I believe is transcendentally important: the single-wall carbon nanotubes, which are actually giant fullerenes. The reason they have this transcendental importance, at least at the moment, is that the properties you actually measure for these things are very close and sometimes exactly the properties you expect for a perfect fullerene, where no single carbon is missing from the structure.

Dr. Richard Smalley
1996 Nobel Laureate

The discovery of carbon nanotubes is mostly regarded as one of the most fundamental scientific events in the last twenty years. The expected structural perfection, exceptional electrical and mechanical properties of carbon nanotubes make them potential candidates for a wide range of applications such as making molecular devices, reinforcing polymer composites, etc. This thesis is about the molecular simulation of mechanical properties of single-walled carbon nanotubes (SWNT), influence of defects on SWNT mechanical properties, fracture statistics of defected SWNT and interfacial interaction between SWNT and polymers.

1.1 Carbon nanotubes

1.1.1 Structure of carbon nanotubes

Carbon nanotubes are fullerene-related structures which were discovered in 1991 by Sumio Iijima when he used a high-resolution transmission electron microscope (TEM) to study the soot created in an electrical discharge between two carbon electrodes [1]. A carbon nanotube is usually thought of as one or more graphene cylinders, and like graphite the whole structure of a perfect carbon nanotube solely consists of sp^2 carbon atoms. According to the number of graphene cylinders forming a carbon nanotube, the carbon nanotubes can be divided into single-walled nanotubes (SWNT) and multi-walled nanotubes (MWNT). SWNT consist of only one

graphene cylinder, while MWNT consist of several concentrically arranged graphene cylinders. Both SWNT and MWNT structures are shown in Figure 1.1,

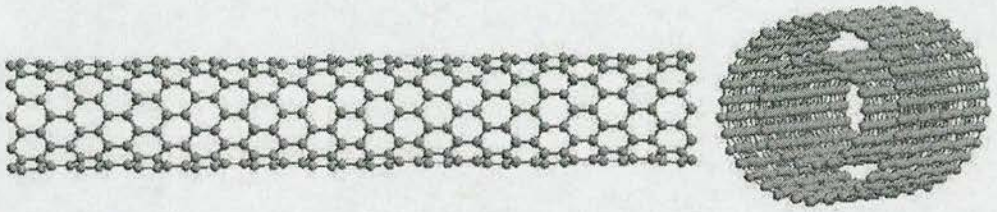

Figure 1.1: *SWNT and MWNT structures*

By thinking of each graphene cylinder as a result of rolling a graphene sheet and specifying the direction of rolling and the circumference of the cross-section, the structure is conveniently expressed in terms of a one-dimensional unit cell. In Figure 1.2 there is a graphene sheet with defined roll-up vector **r**. After rolling to form a carbon nanotube, the two end atoms coincide. One thing which should be pointed out here is that **r** can be expressed as a linear combination of base vector **a** and **b** (dashed line in Figure 1.2) of the hexagon [2, 3] as in Equation 1.1,

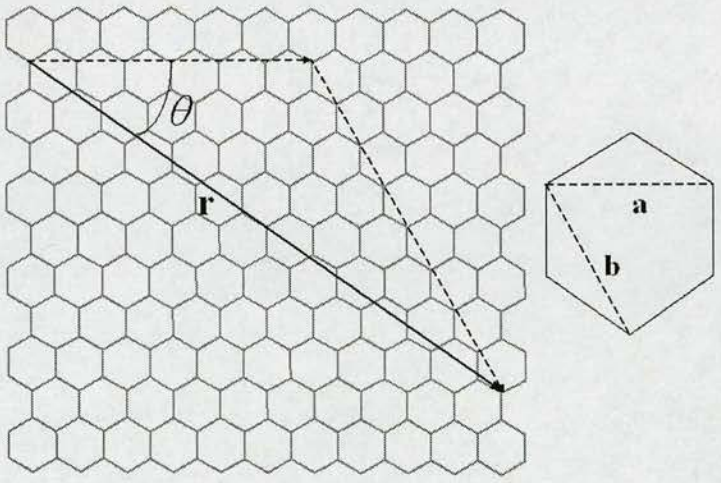

Figure 1.2: *Definition of roll-up vector as linear combinations of base vectors **a** and **b***

$$\mathbf{r} = n\mathbf{a} + m\mathbf{b}, \tag{1.1}$$

where n and m are integers. Different types of carbon nanotube are thus uniquely defined by the values of n and m. For example, (4,4), (10,8), (12,12) have unique geometric structures,

and for a SWNT in equilibrium, its diameter is determined by its geometric type defined in Equation 1.1.

Three major categories of carbon nanotubes can also be defined based on the chiral angle θ in Figure 1.2.

$$\begin{aligned} \theta &= 0°, && \text{"zigzag"} \\ 0° < \theta &< 30°, && \text{"chiral"} \\ \theta &= 30°, && \text{"armchair"} \end{aligned}$$

Armchair carbon nanotubes are formed when $n = m$ and the chiral angle θ is 30°. Zigzag carbon nanotubes are formed when either n or m is zero and the chiral angle is 0°. All other nanotubes, with chiral angles intermediate between 0° and 30°, are known as chiral nanotubes.

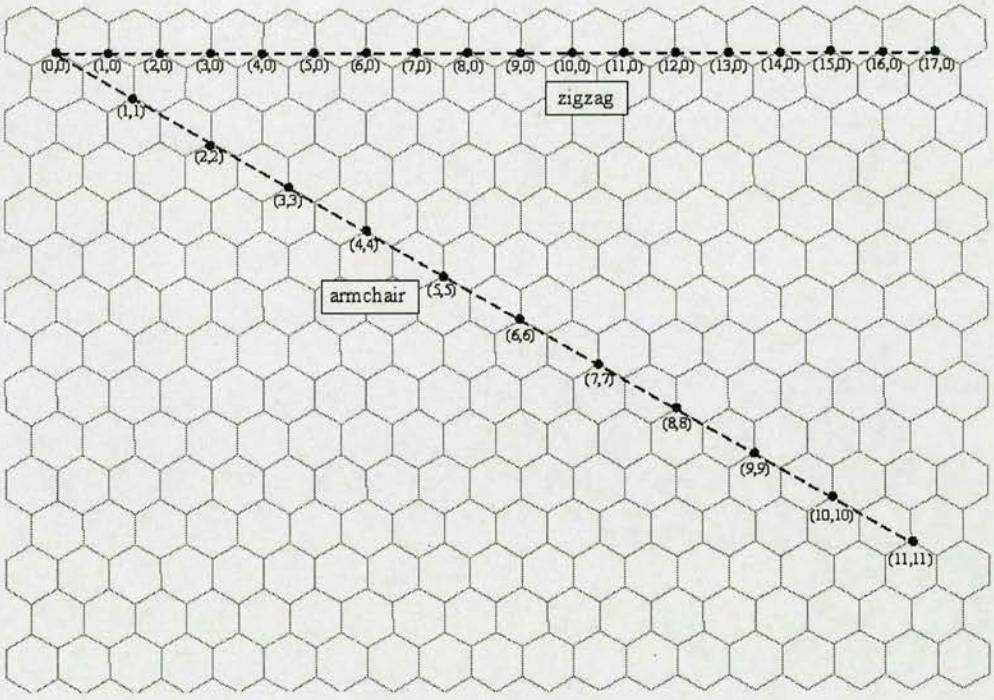

Figure 1.3: *Roll-up vectors for zigzag and armchair SWNT*

Carbon nanotubes exhibit unique electronic properties in that they can be metallic or semiconducting depending on their chirality. It was predicted theoretically that according to electronic properties, the carbon nanotubes have two major classes: on one hand the moderate band gap nanotubes that do not satisfy the $m-n = 3\times$integer condition in the graphene, and on the other hand the small band gap and truly metallic serpentine conformation nanotubes that do satisfy

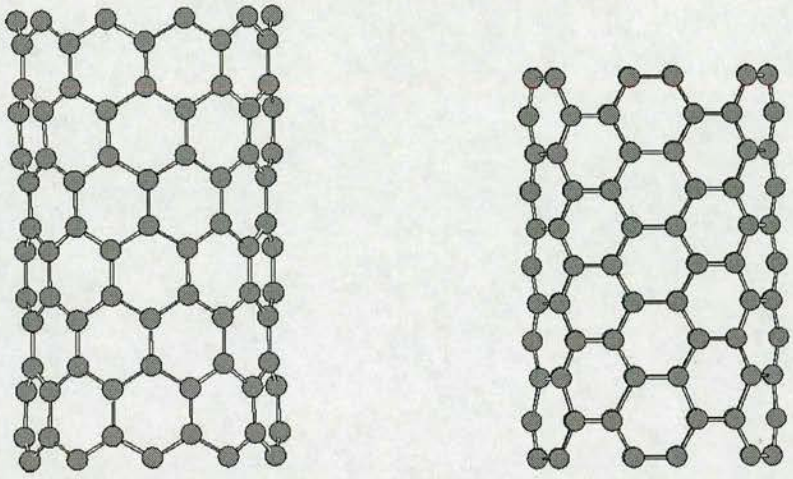

(a) (b)

Figure 1.4: *Structure of SWNT (a): zigzag SWNT (b): armchair SWNT*

this condition [4–6]. Recent scanning tunnelling microscopy (STM), scanning tunnelling spectroscopy (STS) and ^{13}C nuclear magnetic resonance (NMR) measurements on SWNT support this prediction [7–11]. This novel electronic property of carbon nanotubes allows formation of semiconductor-semiconductor and semiconductor-metal junctions useful in molecular device fabrication.

Carbon nanotube diameters range from about 3 Å to larger than 30 Å for SWNT, and from about 14 to at least 1000 Å for MWNT [12–14]. Thus carbon nanotubes, in particular SWNT, may reach very high aspect ratio (length-to-diameter ratio), which together with their extraordinary strength makes carbon nanotubes ideal candidates as ultra-strong reinforcers for potential composites [15].

1.1.2 Synthesis of carbon nanotubes

Arc-discharge, laser ablation and chemical vapour deposition (CVD) have been the three main methods used for carbon nanotube synthesis [16]. The first two methods employ solid-state carbon precursors to provide carbon sources needed for carbon nanotube growth and involve carbon vaporisation at high temperatures [1, 17]. For the method of arc-discharge, the temperature is greater than 3000 °C, while for laser ablation the temperature is around 1000 °C. These two methods are well established in producing high-quality and nearly perfect nanotube structures, however, they have fatal shortcomings for further large-scale application — the amount

of carbon nanotubes produced is limited and the final product contains substantial amounts of byproducts [18].

Different from the arc-discharge and laser ablation methods, the CVD method utilises hydrocarbon gases as source for carbon atoms and metal catalyst particles as "seeds" for nanotube growth that takes place at relatively lower temperature (500 –1000 °C) [19–21]. This technique makes it possible to produce carbon nanotube in large scale, and is the most promising synthesis route for economically producing large quantities of nanotubes. In 2002, Rodney Andrews and his colleagues have developed a low-cost CVD process for the continuous production of aligned MWNT [22].

These three methods sometimes cannot satisfy applications for certain purposes, and there has been a lot of effort to improve these methods. For instance, the original methods of making carbon nanotubes can produce only small amounts of SWNT. In 1997, the original electric-arc technique used to generate fullerenes and MWNT was improved by C. Journet *et al.* to produce high yields (70 –90%) of SWNTs by laser ablation of carbon targets [23]. Later, with condensation of a laser-vaporised carbon-nickel-cobalt mixture at 1200 °C, Andreas Thess *et al.* made ropes of SWNT in a two-dimensional triangular lattice with a lattice constant of 17 Å [24].

There is another problem in the synthesis of carbon nanotubes with these three original methods: all the above synthesis methods for SWNT result in major concentrations of impurities. To solve this problem, in 2004, Kenji Hata *et al.* improved the method of CVD to make SWNT by adding water to stimulate catalytic activity and enhance the lifetime of catalysts. In this way, they made impurity-free SWNT with carbon purity above 99.98% [25].

A lot of efforts have also been made to produce macroscopic fibers of carbon nanotubes. In 2002, long nanotube strands, up to several centimetres in length, consisting of aligned SWNT were synthesised by the catalytic pyrolysis of *n*-hexane with an enhanced vertical floating technique [26]. Later in 2004, macroscopic fibers composed solely of SWNT were also produced through conventional spinning. In this method, fuming sulfuric acid is used to charge SWNT and promotes their ordering into an aligned phase of individual mobile SWNT surrounded by acid anions, and then the ordered dispersion was extruded via solution spinning into continuous lengths of macroscopic SWNT fibers [27].

1.1.3 Mechanical properties of carbon nanotubes

The bonding structure of carbon nanotubes provides them with unique mechanical properties. According to theoretical estimates, carbon nanotubes are the strongest known material as far as tensile strength is concerned [28]. The main mechanical properties of different materials are shown in Table 1.1.

Materials	Young's modulus (GPa)	Tensile Strength (GPa)	Density(g/cm^3)
SWNT	1250	250	1.4
MWNT	1800	250	2.6
Diamond	600	130	3.5
Kevlar	186	3.6	7.8
Steel	208	1.0	7.8
Wood	16	0.008	0.6

Table 1.1: *Strength of different materials*

1.1.3.1 Young's modulus

The Young's modulus is a material property that describes elastic stiffness and is one of the most important mechanical properties in materials study. Experimental analysis of Young's modulus of carbon nanotubes has been mostly made by assuming the carbon nanotubes to be elastic beams [2, 29]. Assuming small deformations, the equation of motion for a beam is

$$\rho A \frac{\partial^2 u}{\partial t^2} + YI \frac{\partial^4 u}{\partial x^4} = q(x), \tag{1.2}$$

where u is the displacement, ρ is the density, A the cross-sectional area, Y Young's modulus, I the moment of inertia, and $q(x)$ a distributed applied load. This equation is derived assuming that displacements are small and that sections of the beam normal to the central axis in the unloaded state remain normal during bending. These assumptions are usually valid for small deformations of long, thin beams, although deviations from this linear theory are probable for many applications of carbon nanotubes [30].

The natural frequency of the i^{th} mode of vibration is then given by

$$\omega_i = \frac{\beta_i^2}{L^2} \sqrt{\frac{EI}{\rho A}}, \tag{1.3}$$

where β_n is the root of an equation that is dictated by the boundary conditions. For a beam clamped at one end and free at the other, this equation is

$$\cos\beta_n \cosh\beta_n + 1 = 0. \tag{1.4}$$

Thus, the frequencies of the first three modes of vibration can be computed from Equation(1.4) as $\beta_1 \approx 1.875$, $\beta_2 \approx 4.694$, $\beta_3 \approx 7.855$ for the first three modes, respectively, and $\beta_n \approx (n + 1/2)\pi$ for larger n. The undamped vibration frequency is

$$\omega_n = 2\pi f_n = \frac{\beta_n^2}{2L^2}\sqrt{\frac{Y(a^2 + b^2)}{\rho}}. \tag{1.5}$$

Measurements on vibrating carbon nanotubes can, therefore, be used to estimate Young's modulus. Using this method, the Young's modulus of carbon nanotubes was found at an average of about 1.8 TPa for 11 samples of MWNT and 1.25 TPa for 27 samples of SWNT by observing their freestanding vibration in TEM [29, 31].

Rather than relying on estimates of thermal vibrations, methods using electromechanical excitation and static beam bending have also used to measure Young's moduli of carbon nanotubes [30, 32].

1.1.3.2 Tensile strength

The tensile strength is the maximum resistance to fracture. It is equivalent to the maximum load that can be carried by a material when the load is applied in simple tension. The tensile strength of carbon nanotubes is predicted to be as high as 250 GPa. In experiment, the stress-strain response and strength-at-failure of carbon nanotubes were measured with SEM and AFM [33, 34]. First, a manipulation tool built was used as a mechanical loading device, which operated inside a SEM. Afterwards, individual carbon nanotubes were picked up and attached at each end of a section length onto the opposite tips of AFM cantilever probes. Each nanotube section was then stress-loaded and observed in situ in the SEM. The AFM probes used in these experiments provide a sharp end for picking up and mounting each nanotube, and they act as force sensors through the imaging of the cantilever deflection. By recording the whole tensile-loading experiment, both the deflection of the cantilever and the length change of the nanotube were simultaneously obtained. In this way, Yu et.al [33, 34] measured the mechanical

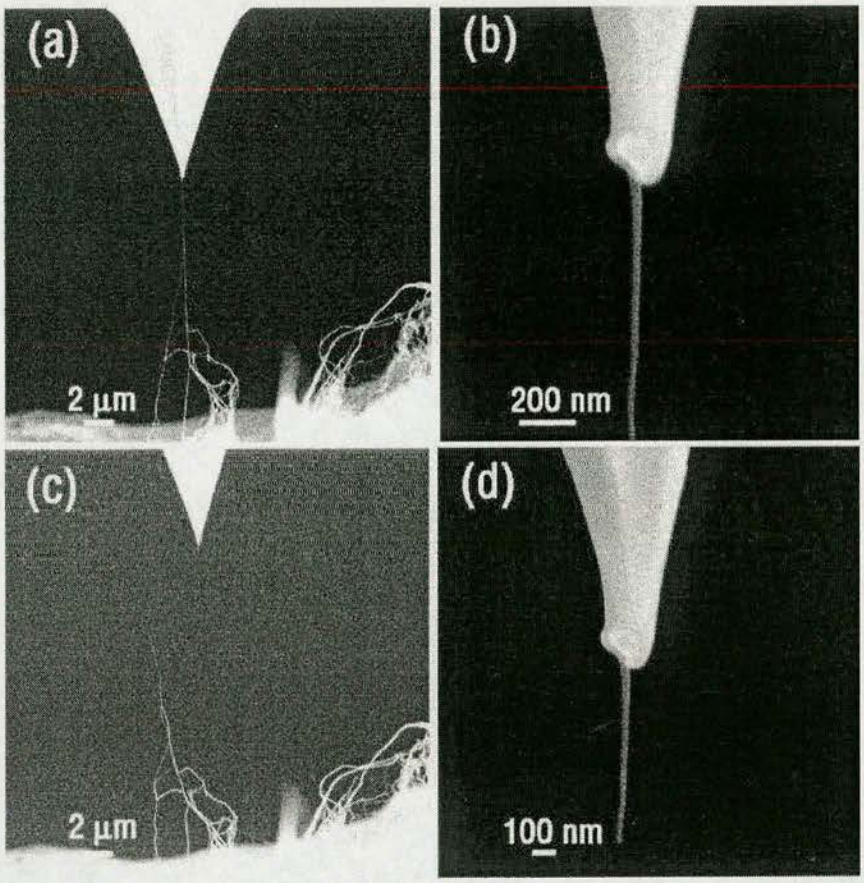

Figure 1.5: *Fracture of SWNT, this image is courtesy of MF Yu et al [33]*

response of SWNT and MWNT under tensile load. For SWNT, the values of tensile strength range from 13 to 52 GPa (mean 30 GPa). MWNT broke in the outermost layer, and the tensile strength of this layer ranged from 11 to 63 GPa for the set of 19 MWNT which were loaded. There is a huge difference between the tensile strength predicted by theoretic calculations and that measured from experiments, which very likely depends on the distribution of defects and geometric factors [35].

1.1.3.3 Buckling of carbon nanotubes

A material may fail to support its load in compression, and buckling is the most common mode of failure under compressive load. Leonhard Euler long ago showed that there is a critical load for buckling of a slender column. Experiments and theory have addressed structural instability of carbon nanotubes under axial compression, bending or torsion [36–42]. It has been shown

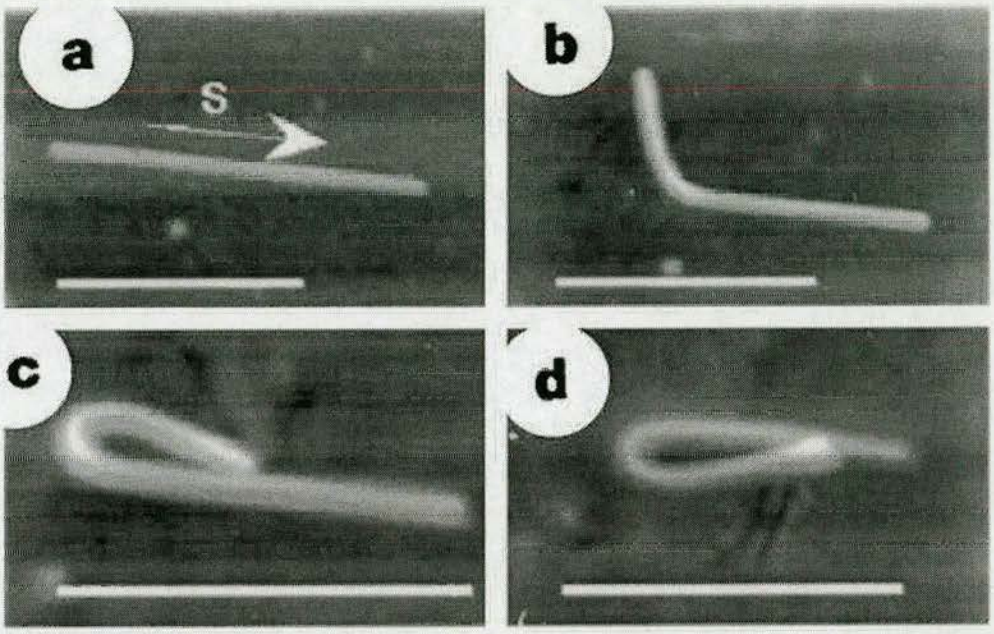

Figure 1.6: *Buckling of a carbon nanotube, this image is courtesy of MR Falvo et al [37]*

that buckling of carbon nanotubes can occur in both axial and transversal directions [43]. Such instability is characterised by the collapse of the cross-section and confirmed by TEM and AFM experiment observations as shown in Figure 1.6. It was shown that carbon nanotubes can be bent repeatedly through large angles using the tip of an AFM, without undergoing catastrophic failure [37]. Buckling can either occur in the whole structure or locally, depending on diameter and length of the nanotubes [44, 45].

1.1.4 Applications of carbon nanotubes

Because of their unique mechanical and electrical properties, carbon nanotubes have a lot of potential applications in many fields. For example, intramolecular junctions in carbon nanotubes have already been made, which are potentially ideal structures for building robust, molecular electronics [46]. The development of methods for the routine synthesis of carbon nanotubes has generated intense interest in exploiting their remarkable mechanical properties in more general applications [22]. The conductivity, strength, elasticity, toughness, and durability of polymer composites may all be substantially improved by the addition of nanotubes. The very high aspect ratio of carbon nanotubes enables them to be aligned with one axis of the composite. In other applications, their high axial electrical conductivity offers the potential for fabricating

conducting polymers. It has been reported that by using only 1 wt% MWNT reinforcement the elastic stiffness of polymer-matrix nanocomposites was improved by 40% over that of the bare polymer-matrix materials and strength values were improved by nearly 25% [47].

1.2 Objectives of this thesis

Up to now, most studies on mechanical properties of carbon nanotubes have focused on nanotubes without any defect, which were usually thought of as perfect cylinder-like structures. However, recent studies indicate that carbon nanotubes are probably not as perfect as they were thought to be. In practical applications, defects such as pentagons, heptagons, vacancies or functionalization defects are very common. They might result from synthesis [48–51], or be deliberately introduced in order to modify properties of carbon nanotubes [52, 53]. Since such defects may significantly change the mechanical properties, an accurate assessment of their influence is essential for potential applications of carbon nanotubes such as composite reinforcement.

Another concern on carbon nanotubes is about their interfacial bonding in polymer composite applications. Good interfacial bonding is required to achieve load transfer across the carbon nanotube-matrix interface, a necessary condition for improving the mechanical properties of the composite. It is important to characterise fully the polymer morphology and bonding strength around the interfacial region between nanotubes and polymers.

Therefore, the objectives of this thesis are to use state-of the-art molecular simulation methods to investigate the mechanical properties of carbon nanotubes with or without defects, and the interaction between nanotubes and polymers.

1.3 Thesis overview

The thesis is divided separated into five main parts:

Chapter 1 Here we present an introduction to carbon nanotubes including their properties and applications, and the objectives of our study are stated.

Chapter 2 In this chapter, we briefly talk about the principles of molecular mechanics and molecular dynamics. The main simulation methods and force fields used in our study are ex-

plained.

Chapter 3 In this chapter, we use molecular mechanics to study the buckling of single-wall carbon nanotubes with/without defect(s) under compressive load. Three kinds of defects including functionalization defects, topological defects and vacancies are introduced onto carbon nanotubes. Carbon nanotubes of various diameter are studied, and the influence of defects on their buckling strength is investigated.

Chapter 4 In this chapter, we use molecular mechanics simulations to study the fracture behaviour of carbon nanotubes with/without defects under tensile load. Size dependence of fracture strength of carbon nanotubes with defects is studied with extreme order statistics, and a relationship between length of carbon nanotubes and their fracture strength is established. This study reasonably explains the difference between fracture strength measured in experiments and that obtained from theoretical calculations on ideal carbon nanotubes.

Chapter 5 In this chapter, we use molecular dynamics simulations to study the interaction between single wall carbon nanotubes and polymers including flexible polymers and rigid conjugated polymers. The conformation of different polymers interacting with carbon nanotubes is investigated and the interaction energy is calculated. The results indicate that flexible polymers with conjugated backbone might have strong interaction with carbon nanotubes, and they are promising candidate matrix materials in making carbon nanotube reinforced polymer composites.

Chapter 6 In this chapter, we summarise our work, and suggest directions for future work on the subject.

Chapter 2
Brief introduction to molecular mechanics and molecular dynamics

2.1 Introduction

Molecular mechanics (MM) can be based on quantum mechanics via the Born-Oppenheimer approximation. According to this approximation, the electronic motions are completely ignored and the energy of a molecular system is calculated as a function of the nuclear positions only. In molecular mechanics, the interatomic interactions of molecules are usually described by an empirical potential energy function (force field), which depends on the structure (geometry) of the molecule. In practise, the challenge and success of molecular mechanics rely on both effective formulation of the potential energy function and the application of suitable search algorithms to find conformations of minimal energy.

Molecular dynamics (MD) is a method based on molecular mechanics to study the time evolution of a molecular system. The evolution is based on the Newton's law, $F = ma$, and the forces are obtained as gradients of a certain potential which is a function of the geometry of the molecular system. As a counterpart to experiment, molecular dynamics simulations are used to estimate equilibrium and dynamics properties of complex systems that cannot be calculated analytically.

Molecular mechanics is different from molecular dynamics since molecular mechanics ignores the temporal evolution of the system and instead focuses on finding particular geometries and their associated energies or other static properties such as equilibrium structures, etc. It only provides an absolute result in term of energy regardless of temperature, pressure, etc, which is insufficient for understanding certain phenomena since molecules continuously interact among themselves and with surrounding molecules. In contrast to molecular mechanics, molecular dynamics follows the dynamics of a molecular system in space and time, thereby, we can obtain a rich amount of information concerning structural and dynamic properties including molecular geometries and energies; deformation of macromolecules, etc.

In our study, we use both molecular mechanics and molecular dynamics. Molecular mechanics is used to study the compression and elongation of carbon nanotubes since the changes of their potential energy are the key factor in determining their mechanical behaviour under external load. By contrast, we use molecular dynamics to study the interaction between carbon nanotubes and polymers since we want to understand influence of temperature, continuous change of configuration, etc.

2.2 Molecular mechanics

2.2.1 The Born-Oppenheimer approximation

The complete mathematical description of a molecule, including both quantum mechanical and relativistic effects, is a formidable problem, due to the small scales and large velocities of electrons and neutrons. However, for most applications, these intricacies are ignored and the relativistic and quantum effects can be implicitly incorporated into functions based on empirical data.

Since no complete relativistic quantum mechanical theory is suitable for the description of molecules, we shall only consider situations where the potential energy is independent of time, which enables the Schrödinger equation to be written in nonrelativistic, time-independent form [54]:

$$\mathcal{H}\psi(r, R) = E\psi(r, R), \tag{2.1}$$

where $\mathcal{H}$ is the Hamiltonian for the system, ψ is the wavefunction, and E is the potential energy. In general, ψ is a function of the coordinates of the nuclei (R) and of the electrons (r).

However, the Schrödinger equation is still too complex and can only be solved for very small systems, so approximations are made. Noting that the electrons are several thousands of times lighter than the nuclei and therefore move much faster, Born and Oppenheimer (1927) proposed what is known as the Born-Oppenheimer approximation: the motion of the electrons can be decoupled from that of the nuclei, and the total wavefunction for the molecule can be written in the following form:

$$\psi(r, R) = \psi(r)\psi(R). \tag{2.2}$$

As a result, the Born-Oppenheimer approximation gives two separate equations. The first equa-

tion describes the electronic motion:

$$\mathcal{H}\psi(r;R) = E(R)\psi(r;R) \tag{2.3}$$

and depends only parametrically on the positions of the nuclei. Note that this equation defines an energy $E(R)$, which is a function of the coordinates of the nuclei only. This energy $E(R)$ is usually called the potential energy surface.

The second equation then describes the motion of the nuclei on this potential energy surface $E(R)$:

$$\mathcal{H}\psi(R) = E(R)\psi(R). \tag{2.4}$$

The direct solution of Equation 2.3 is the province of *ab initio* quantum chemical calculations. Semiempirical calculations also solve Equation 2.3, but it approximates many of the integrals with empirically fit functions.

Most times we are content simply to know the potential energy contributed by the electrons as function of the distance between the nuclei. That is, in many systems the only significant impact that the electrons have on nuclear position is to make a contribution to the potential energy $E(R)$ of the system. If we know the positions of the nuclei of a molecular system we can determine the potential energy of the system. This is effectively, a Newtonian potential energy function (not quantum mechanical), despite the fact that the particular value of $E(R)$ at a particular point could be computed from Schrödinger's equation.

2.2.2 Force field

Because the gradient of the potential energy function $E(R)$ defines a conservative force field, MM methods are also called "force field" methods. While it would in principle be possible to determine $E(R)$ by solving Schrödinger's equation, in practice it is usual to use available experimental data and to infer the nature and shape of $E(R)$ by interpolation. A force field is normally based upon a rather simple model of the interactions within a system with contributions from processes such as the stretching of bonds, the opening and closing of bond angles and the rotations about single bonds. A simple force field could have the following potential

energy function:

$$E_{pot} = \sum_{bonds} E_{bond}(i,j) + \sum_{angles} E_{angle}(i,j,k) + \sum_{dihedrals} E_{dih}(i,j,k,l) + \sum_{atompairs} E_{ij}(i,j), \tag{2.5}$$

where i,j,k and l are atoms involved in the respective interactions, and E_{bond}, E_{angle}, E_{dih}, and E_{ij} are empirical potential functions representing chemical bonds, bond angles, dihedral angles and non-bond pairwise interactions. The first three are regarded as intra-molecular interactions and the last as inter-molecular interactions. Now the forces can be written in terms of potential energy functions of various structural features such as bond lengths, bond angles, non bonded interactions etc. For example, the potential functions can be as follows:

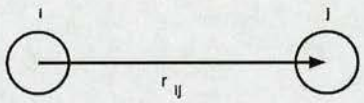

Figure 2.1: *Bond potential function* E_{bond}

- $$E_{bond}(r_{ij}) = \frac{1}{2}k(r_{ij} - r_0)^2; \tag{2.6}$$

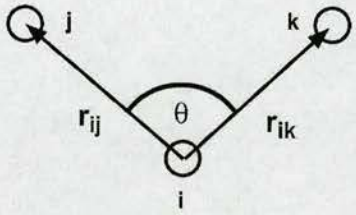

Figure 2.2: *Bond angle potential function* E_{angle}

- $$E_{angle}(\theta_{jik}) = \frac{k}{2}(\theta_{jik} - \theta_0)^2; \tag{2.7}$$

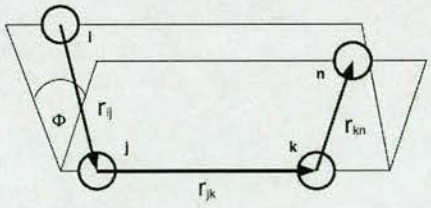

Figure 2.3: *Dihedral angle potential function* E_{dih}

- $$E_{dih}(\phi_{ijkn}) = \frac{1}{2}k(\phi_{ijkn} - \phi_0)^2; \tag{2.8}$$

- Non-bond pairwise potential function E_{ij} (the standard Lennard Jones potential)

$$E_{ij}(r_{ij}) = 4\epsilon\left[(\frac{\sigma}{r_{ij}})^{12} - (\frac{\sigma}{r_{ij}})^6\right]; \tag{2.9}$$

These functions together with the parameters required to fit the potential energy define a force field. Many different kinds of force fields have been developed over the years, and some have more complicated functions and include additional energy terms that describe other kinds of conformations. The goal of a force field is to describe entire classes of molecules with reasonable accuracy. In a sense, the force field interpolates and extrapolates from empirical data or *ab initio* computations of a small set of samples used to parameterise the force field to a larger set of related models, and it returns the energy of a system as a function of the conformation of the system. Since force fields are combinations of potential energy terms, they are also sometimes referred to as potentials.

Parameterisation of force fields ensures that calculations produce appropriate molecular geometries and interaction energies for a set of model compounds that are appropriate for the force field. Force field parameters are optimised such as to reproduce the increasing body of experimental information ranging from molecular geometries (from crystal and solution studies) to many other properties: measurements of vibrational frequencies, heats of formation, intermolecular energies and geometries, torsional barriers, and more.

Generally, force fields are used within the class of compounds for which the parameters had been fitted. In the following, we will talk about MM3 force field and Brenner's potential, which are used in our study [54].

2.2.2.1 MM3 force field

MM3 force field has been developed by Allinger and coworkers [55] from 1989 based on MM2 force field, which was first formulated during the 1976-1977 period. The functions that describe the force field are as follows:

- Bond stretching

$$E_s = 71.94k_s(l - l_0)^2 \left[1 - 2.55(l - l_0) + (7/12)2.55(l - l_0)^2\right], \tag{2.10}$$

- Angle bending

$$\begin{aligned} E_\theta &= 0.021914(k_\theta)(\theta - \theta_0)^2[1 - 0.014(\theta - \theta_0) + 5.6(10^{-5}) \times \\ &\quad (\theta - \theta_0)^2 - 7.0(10^{-7})(\theta - \theta_0)^3 + 9.0(10^{-10})(\theta - \theta_0)^4], \end{aligned} \tag{2.11}$$

- Torsion

$$\begin{aligned} E_\omega &= (V_1/2)(1 + \cos\omega) + (V_2/2)(1 - \cos 2\omega) + \\ &\quad (V_3/2)(1 + \cos 3\omega), \end{aligned} \tag{2.12}$$

- Stretch-bending interaction

$$E_{s\theta} = 2.51118K_{s\theta}\left[(l - l_0) + (l' - l_0')\right](\theta - \theta_0), \tag{2.13}$$

- Torsion-stretch interaction

$$E_{\omega s} = 11.995(K_{\omega s}/2)(l - l_0)(1 + \cos 3\omega), \tag{2.14}$$

- Bend-bend interaction

$$E_{\theta\theta'} = -0.021914K_{\theta\theta'}(\theta - \theta_0)(\theta' - \theta_0'), \tag{2.15}$$

- van der Waals' interactions

$$E_{vdw} = \epsilon\left\{-2.25(r_v/r)^6 + 1.84(10)^5 \exp[-12.00(r/r_v)]\right\}, \tag{2.16}$$

The parameters are determined beginning with the necessary bending and stretching parameters, taking them to be equal to the spectroscopic force constants, and then calculating many known structures to obtain values for l_0, θ_0, etc. Having then good geometries for the molecules, the vibrational spectra were examined, and the force parameters were further adjusted. Small

further modifications of the structural parameters were then made to refine the calculated values for these data as well as possible. Simultaneously, heats of formation, crystal structures, and van der Waals' parameters were examined [55].

In our study, most of atoms are sp^2 hybridised carbon atoms of graphite or carbon nanotube. The parameters are as shown in Table 2.1.

(A) Bond stretching

atoms	l_0	k_s
C-C	1.3320	7.5000

(B) Angle bending

atoms	k_θ	θ_0
C-C-C	0.7600	122.000

(C) Torsion

atoms	V_1	V_2	V_3
C-C-C-C	-0.670	10.000	0.000

(D) Stretch-bending interaction

atoms	K_{sb}
C-C-C	0.1300

(E) Bend-bend interaction

atoms	$K_{\theta\theta'}$
C-C-C	0.2400

(F) van der Waals' interaction

atoms	ϵ	r_v
CC	1.9600	0.056

Table 2.1: *MM3 force field parameter set for carbon nanotube (none torsion-stretch interaction) [53]*

2.2.2.2 Brenner's potential

Following the earlier Abell-Tersoff bond order potential [56–59], the reactive empirical bond order (REBO) potential has been developed by Donald W Brenner *et al.* since 1985 [60, 61], and Brenner's REBO potential is usually referenced as Brenner's potential. This potential is characterised by the quantum-mechanical concept of bond order formalism, and it is of particular utility in modelling graphite and carbon nanotube structures. The potential, though limited

to the elements carbon and hydrogen, has the great advantage that it can handle transition states and unstable structures. Thus, given essentially arbitrary coordinates of the carbon and hydrogen atoms in a system without specifying bond connections, Brenner's potential will return the energy of the system. Unlike normal force fields, Brenner's potential allows formation and destruction of bonds, which makes it possible to trace the energy of carbon nanotubes during fracture.

Beginning with a local basis of unperturbed atomic orbitals, Abell showed that the chemical binding energy E_b can be simply written as a sum over nearest neighbours in the form [56]

$$E_b = \sum_i \sum_{j>i} \left[V^R(r_{ij}) - \overline{B}_{ij} V^A(r_{ij}) \right] . \tag{2.17}$$

The functions $V^R(r)$ and $V^A(r)$ are pair-additive interactions that represent all interatomic repulsions (core-core, etc) and attraction from valence electrons, respectively. The quantity r_{ij} is the distance between pairs of nearest-neighbour atoms i and j, and $\overline{B}_{ij}$ is a bond order between atom i and j that is derivable from Huckel or similar level electronic structure theory.

Tersoff introduced this important concept into the modelling of Group IV elements such as C, Si, and Ge, and the result showed that the bond structure of complex molecules of these elements is well represented. In Tersoff-Abell bond order formalism, the energy of the system is a sum of the energies of each bond. The energy of each bond is composed of a repulsive part and an attractive part. A bond order function is embedded in the formulation. The bond order depends on the local atomic environment [57, 58].

Brenner modified the Tersoff potential by introducing additional terms into the bond order function. The main purpose of these extra terms is to correct the overbinding of radicals. Compared with the Tersoff potential, Brenner's potential shows robustness in the treatment of conjugacy, and it allows for forming and breaking bonds with the correct representation of bond order. The forms:

$$V_R(r_{ij}) = f_{ij}(r_{ij}) D_{ij}^{(e)} / (S_{ij} - 1) e^{-\sqrt{2S_{ij}}\beta_{ij}(r - R_{ij}^{(e)})} \tag{2.18}$$

and

$$V_A(r_{ij}) = f_{ij} D_{ij}^{(e)} S_{ij} / (S_{ij} - 1) e^{-\sqrt{2/S_{ij}}\beta_{ij}(r - R_{ij}^{(e)})} \tag{2.19}$$

are used for the pair terms. The function $f_{ij}(r)$, which restricts the pair potential to nearest

neighbours, is given by

$$f_{ij}(r) = \begin{cases} 1 & r < R_{ij}^{(1)}, \\ \frac{1}{2}\left[1 + \cos\left[\frac{\pi(r - R_{ij}^{(1)})}{R_{ij}^{(2)} - R_{ij}^{(1)}}\right]\right] & R_{ij}^{(1)} \leq r \leq R_{ij}^{(2)}, \\ 0 & r > R_{ij}^{(2)}. \end{cases} \tag{2.20}$$

The parameters for carbon are as shown in Table 2.2.

parameter	value
$R^{(e)}$	1.315×10^{-10} m
D_e	6.325 eV
β	1.5×10^{10} m^{-1}
S	1.29
$R^{(1)}$	1.7×10^{-10} m
$R^{(2)}$	2.0×10^{-10} m

Table 2.2: *Brenner's potential parameter set for carbon [59]*

The parameter $\overline{B}_{ij}$ in Equation 2.17 is the bond order parameter, which can be calculated from

$$\overline{B}_{ij} = \frac{1}{2}(B_{ij} + B_{ji}), \tag{2.21}$$

where

$$B_{ij} = \left[1 + \sum_{k(\neq i,j)} G(\theta_i jk) f(r_{ik})\right]^{-\delta}, \tag{2.22}$$

δ=0.80469, r_{ik} is the distance between atoms i and k, f_c is the cutoff function in Equation 2.20, θ_{ijk} is the angle between bonds i-j and i-k, the function G is given by

$$G(\theta) = a_0\left[1 + \frac{c_0^2}{d_0^2} - \frac{c_0^2}{d_0^2 + (1 + \cos\theta)^2}\right], \tag{2.23}$$

and the constants $a_0 = 0.011304$, $c_0 = 19$, $d_0 = 2.5$. It is straightforward to show that B_{ij} is very close to 1. For $\theta = 2\pi/3$, as in the equilibrium structure of a graphene, the coefficient $\overline{B}_{ij} = 0.95$.

2.2.3 Energy minimisation

In MM calculations, we are especially interested in finding minima of the energy surface of a molecular system. Minimum energy configurations of a molecule correspond to stable states, and any movement away from a minimum gives an unfavourable configuration with a higher energy. There might be a very large number of minima on the energy surface. The minimum with the very lowest energy is known as the global energy minimum. To identify those optimal geometries of the system that correspond to minimum points on the energy surface we use a minimisation algorithm [54].

The minimisation problem can be formally stated as follows: given a function f with depends on one or more independent variables x_1, x_2,...,x_i, find the values of those variables where f has a minimum value. At a minimum point the first derivative of the function with respect to each of the variables is zero and the second derivatives are all positive:

$$\frac{\partial f}{\partial x_i} = 0; \qquad \frac{\partial^2 f}{\partial x_i^2} > 0. \tag{2.24}$$

In molecular mechanics computations the variables x_i are usually the Cartesian coordinates of the particles, where the energy is a function of $3N$ variables (N is the number of the particles). For analytical functions, the minimum of a function can be found using standard calculus. However, this is not generally possible for molecular systems due to the complicated way in which the energy varies with coordinates. Instead, minima are located using numerical methods which gradually change the coordinates to produce configurations with lower and lower energies until the minimum is reached.

The minimisation algorithms in molecular mechanics usually use derivatives of the energy with respect to the coordinates. There are also some non-derivative minimisation methods, but they are out of use simply because of computation efficiency. Derivatives can be useful because they provide information about the shape of the energy surface, and if used properly they can significantly enhance the efficiency with which the minimum is located. The direction of the first derivative of the energy (the gradient) indicates where the minimum lies and the magnitude of the gradient indicates the steepness of the local slope. The energy of the system can be lowered by moving each atom in response to the force acting on it; the force is equal to minus the gradient. Second derivatives indicate the curvature of the function, information that can be

used to predict where the function will change direction. Most of the optimisation algorithms require the repeated computation of

- The function value (optimisation criterion)
- The gradient vector (first-order partial derivatives)
- For some algorithms, the Hessian matrix (second-order partial derivatives)
- Values of linear and nonlinear constraints
- The first-order partial derivatives (Jacobian) of nonlinear constraints

We will talk about the algorithms of "conjugate gradients minimisation" and "Newton-Raphson method", whose variant, the Quasi-Newton method is used in our molecular mechanics calculations.

2.2.3.1 Conjugated gradient minimisation

The gradient of the energy with respect to the coordinates provides information that can be very useful in energy minimisation. The direction of the gradient indicates where the minimum lies and the magnitude of the gradient indicates the steepness of the local slope. The energy of the system can be lowered by moving each atom in response to the force acting on it; the force is equal to minus the gradient. We can expand the function of potential energy into a Taylor series expansion around the point $\mathbf{x}_k$ [54]:

$$E(\mathbf{x}) = E(\mathbf{x}_k) + (\mathbf{x} - \mathbf{x}_k)\mathbf{E}'(\mathbf{x}_k) + (\mathbf{x} - \mathbf{x}_k)^2\mathbf{E}(\mathbf{x}_k)/2 + \ldots, \tag{2.25}$$

where the potential energy $E(\mathbf{x})$ is a function of $3N$ Cartesian coordinates; the vector $\mathbf{x}$ contains $3N$ components and $\mathbf{x_k}$ corresponds to the current configuration of the system; $\mathbf{E}'(\mathbf{x}_k)$ is a $3N \times 1$ matrix (i.e. a vector) which is the partial derivative of E with respect to the appropriate coordinate,$\partial E/\partial x_i$. The gradient at point k is also written as $\mathbf{g}_k$ ($\mathbf{g}_k$=$\mathbf{E}'(\mathbf{x}_k)$). Each element $\mathbf{E}''_{ij}(\mathbf{x}_k)$ of the matrix $\mathbf{E}''(\mathbf{x}_k)$ is the partial second derivative of the energy function with respect to the two coordinates x_i and x_j, $\mathbf{E}''_{ij}$ ($\mathbf{E}''_{ij} = \partial^2 E/\partial x_i \partial x_j$). $\mathbf{E}''(\mathbf{x}_k)$ is thus of dimension $3N \times 3N$ and is known as the *Hessian* matrix of the force constant matrix.

The conjugate gradients method moves in a direction $\mathbf{e}_k$ from point $\mathbf{x}_k$ where $\mathbf{e}_k$ is computed from the gradient at the point and the previous direction vector $\mathbf{e}_{k-1}$:

$$\mathbf{e}_k = -\mathbf{g}_k + \gamma_k \mathbf{e}_{k-1}. \tag{2.26}$$

γ_k is a scalar constant given by

$$\gamma_k = \frac{\mathbf{g}_k \cdot \mathbf{g}_k}{\mathbf{g}_{k-1} \cdot \mathbf{g}_{k-1}}. \tag{2.27}$$

In the conjugate gradient method all of the directions and gradients satisfy the following relationships:

$$\mathbf{g}_i \cdot \mathbf{g}_j = 0; \qquad \mathbf{e}_i \cdot \mathbf{E}''_{ij} \cdot \mathbf{e}_j = 0; \qquad \mathbf{g}_i \cdot \mathbf{e}_j = 0. \tag{2.28}$$

A set of conjugate directions has the property that for a quadratic function of M variables, the minimum will be reached in M steps.

2.2.3.2 Newton-Raphson method

The Newton-Raphson uses not only the first derivative (the gradient), but also the second derivatives to locate the minimum. Second derivatives provide information about the curvature of the function. The Newton-Raphson method is the simplest second-order method. Recall our Tayler series expansion about $\mathbf{x}_k$, Equation(2.25):

$$E(\mathbf{x}) = E(\mathbf{x}_k) + (\mathbf{x} - \mathbf{x}_k)\mathbf{E}'(\mathbf{x}_k) + (\mathbf{x} - \mathbf{x}_k)^2 \mathbf{E}(\mathbf{x}_k)/2 + \ldots.$$

The first derivative of $V(x)$ is:

$$\mathbf{E}'(\mathbf{x}) = \mathbf{E}'(\mathbf{x}_k) + (\mathbf{x} - \mathbf{x}_k)\mathbf{E}''(\mathbf{x}_k). \tag{2.29}$$

If the function is purely quadratic, the second derivative is the same everywhere, and so $\mathbf{E}''(\mathbf{x}) = \mathbf{x_k}$.

At the minimum ($\mathbf{x} = \mathbf{x}^*$), $\mathbf{E}'(\mathbf{x}^*) = 0$ and so

$$\mathbf{x}^* = \mathbf{x}_k - \mathbf{E}'(\mathbf{x}_k)\mathbf{E}''^{-1}(\mathbf{x}_k), \tag{2.30}$$

$\mathbf{E}''^{-1}(\mathbf{x}_k)$ is the inverse Hessian matrix of second derivatives which must therefore be inverted.

The Newton-Raphson method is usually very reliable, works well with boundary and general linear constraints, and generally converges after a few iterations to a precise solution. However, this technique needs to compute a Hessian matrix in each iteration. One needs at least $4(n(n+1)/2)t$ bytes of work memory (n = the number of manifest variables, t = the number of parameters to estimate) to store variables. Computing the approximate Hessian in each iteration can be very time and memory demanding, especially for large molecular systems. The Newton - Raphson method is thus more suited to small molecules (usually less than 100 atoms). For large molecular systems a quasi-Newton technique, a variant on the Newton-Raphson method, especially with Broyden-Fletcher-Goldfarb-Goldfarb-Shanno (BFGS) update [62], can be far more efficient. The Quasi-Newton method is the main method used to optimise the molecular structure in our simulations.

2.2.3.3 Quasi-Newton method

The calculation of the inverse Hessian matrix is a potentially time-consuming operation which is a significant drawback of the Newton-Raphson method. The quasi-Newton method gradually builds up the inverse Hessian matrix in successive iterations. That is, a sequence of matrices $\mathbf{H}_k$ is constructed that has the property [54]

$$\lim_{k\to\infty} \mathbf{H}_k = \mathbf{E}''^{-1}. \tag{2.31}$$

At each iteration k, the new positions $\mathbf{x}_{k+1}$ are obtained from the current positions $\mathbf{x}_k$, the gradient $\mathbf{g}_k$ and the current approximation to the inverse Hessian matrix $\mathbf{H}_k$:

$$\mathbf{x}_{k+1} = \mathbf{x}_k - \mathbf{H}_k\mathbf{g}_k, \tag{2.32}$$

$$\mathbf{H}_{k+1} = \mathbf{H}_k + \frac{(\mathbf{x}_{k+1} - \mathbf{x}_k) \otimes (\mathbf{x}_{k+1} - \mathbf{x}_k)}{(\mathbf{x}_{k+1} - \mathbf{x}_k) \cdot (\mathbf{g}_{k+1} - \mathbf{g}_k)} + \ldots. \tag{2.33}$$

Finally, we have to point out that no algorithm for optimisation exists that will always find the global optimum in a reasonable amount of time. We can only hope to find an approximation to the true minimum or saddle point. It is therefore necessary to have some means to decide if the approximation is sufficiently close to the minimum and so the optimisation can be terminated, otherwise, most minimisation calculations will keep going forever, moving ever closer to the minimum. A simple strategy is to monitor the energy from one iteration to the next and to

stop when the difference in energy between successive steps falls below a specified value. An alternative is to monitor the change in coordinates and to stop when the difference between successive configurations is sufficiently small. A third method is to calculate the root-mean-square (rms) gradient. This is obtained by adding the squares of the gradients of the energy with respect to the coordinates, dividing by the number of coordinates and taking the square root:

$$\text{rms} = \sqrt{\frac{\mathbf{g}^T\mathbf{g}}{3N}}. \tag{2.34}$$

2.3 Molecular dynamics

Molecular dynamics (MD) is a computer simulation technique where successive configurations of a system are generated by integrating Newton's laws of motion. The result of a molecular dynamics calculation is a time evolution of the positions and velocities of the atoms in the system. A trajectory is obtained by solving the differential equations

$$\frac{d^2x_i}{dt^2} = \frac{F_{x_i}}{m_i}. \tag{2.35}$$

This equation describes the motion of a atom of mass m_i along one coordinate (x_i) with F_{x_i} being the force on the atom in that direction.

2.3.1 Time integration algorithm

The Equation 2.35 cannot be solved analytically for a real molecular system. The force on each atom will change whenever the atom changes its position, or whenever any of the other atoms with which it interacts changes position, therefore, the motions of all atoms are coupled together. Under such circumstances, the equations of motion are integrated using time integration algorithms.

Time integration algorithms in MD are based on the finite difference method, where time is discretized on a finite grid, the time step Δt being the distance between consecutive points on the grid. Knowing the positions and some of their time derivatives at time t, the integration scheme gives the same quantities at a later time $t + \Delta t$. By iterating the procedure, the time trajectory of the system can be approximated.

There are several algorithms used in molecular dynamics. Here we mainly discuss two integra-

tion algorithms: Verlet algorithm and Beeman algorithm.

2.3.1.1 Verlet algorithm

Among all the integration algorithms in molecular dynamics, the Verlet algorithm is the most widely used [54]. It uses the positions and accelerations at time t, and the positions from the previous step, $\mathbf{r}(t-\Delta t)$ to calculate the new positions at $t+\Delta t$, $\mathbf{r}(t+\Delta t)$ [63].

$$\mathbf{r}(t+\Delta t) = \mathbf{r}(t) + \Delta t\mathbf{v}(t) + \frac{1}{2}\Delta t^2\mathbf{a}(t) + \ldots, \tag{2.36}$$

$$\mathbf{r}(t-\Delta t) = \mathbf{r}(t) - \Delta t\mathbf{v}(t) + \frac{1}{2}\Delta t^2\mathbf{a}(t) - \ldots. \tag{2.37}$$

Adding up Equations 2.36 and 2.37 gives for the new positions and velocities

$$\mathbf{r}(t+\Delta t) = 2\mathbf{r}(t) - \mathbf{r}(t-\Delta t) + \Delta t^2\mathbf{a}(t). \tag{2.38}$$

The velocities do not explicitly appear in the Verlet integration algorithm. The velocities can be calculated as in Equation 2.39 or 2.40.

$$\mathbf{v}(t) = \left[\mathbf{r}(t+\Delta t) - \mathbf{r}(t-\Delta t)\right]/2\Delta t, \tag{2.39}$$

$$\mathbf{v}(t+\frac{1}{2}\Delta t) = \left[\mathbf{r}(t+\Delta t) - \mathbf{r}(t)\right]/\Delta t. \tag{2.40}$$

The Verlet method is overall second-order accurate. This is because Equation 2.38 is an approximation to Equation 2.35. Though the same trajectory positions are followed in theory, differences are realised in practise among Verlet variants due to finite computer arithmetic. Local accuracy together with stability considerations affect global measurements, like the kinetic temperature.

2.3.1.2 Beeman's algorithm

Like a lot of other integration algorithms, this algorithm is closely related to the Verlet algorithm [64].

$$\mathbf{r}(t+\Delta t) = \mathbf{r}(t) + \mathbf{v}(t)\Delta t + \frac{2}{3}\mathbf{a}(t)\Delta t^2 - \frac{1}{6}\mathbf{a}(t-\Delta t)\Delta t^2, \tag{2.41}$$

$$\mathbf{v}(t+\Delta t) = \mathbf{v}(t) + \frac{1}{3}\mathbf{a}(t+\Delta t)\Delta t + \frac{5}{6}\mathbf{a}(t)\Delta t - \frac{1}{6}\mathbf{a}(t-\Delta t)\Delta t. \tag{2.42}$$

Comparing to the Verlet algorithm, it has more complex expressions and is therefore computationally more demanding, while the advantage of this algorithm is that it provides a more accurate expression for the velocities and better energy conservation. Our MD simulation utilises Beeman's algorithm as integration algorithm.

2.3.2 Integration time step

After we decide the integration algorithm for molecular dynamics, one thing left in the time integration algorithm is the choice of time step Δt. If Δt is too small the trajectory of molecular dynamics will be limited to a small part of the phase space; if Δt is too large it will cause instability of the integration algorithm. The time step should be chosen to be at least an order of magnitude smaller than the length of the time corresponding to the fastest motion in study. The characteristic timescales of internal motion in molecules are shown in Table 2.3 [63].

Internal Motion	Timescale (seconds)
Light-atom bond stretch	10^{-14}
Double-bond stretch	2×10^{-14}
Light-atom angle bend	2×10^{-14}
Heavy-atom bond stretch	3×10^{-14}
Heavy-atom angle bend	5×10^{-14}

Table 2.3: *The characteristic timescales in molecules*

Therefore, in our molecular dynamics simulation a time step of 1 fs (10^{-15} second) is used.

2.3.3 Canonical ensemble and thermostat methods

An experiment is usually made on a macroscopic sample that contains an extremely large number of atoms or molecules sampling an enormous number of conformations. In contrast, from molecular dynamics simulation we can only calculate averages defined in terms of ensemble averages, which are averages taken over a large number of replicas of the system considered simultaneously. (More details are given in the Appendix "Ensembles and ensemble averages in MD simulations".)

In MD simulations there are several different types of thermodynamic ensembles. The microcanonical ensemble (NVE) may be considered as the natural ensemble for MD simulations. If no time dependent external forces are considered, the system's Hamiltonian is constant, imply-

ing that the system's dynamics evolves on a constant energy surface. In practise, this theoretical condition is generally violated due to limited accuracy of the integration algorithms and round-off errors, and long time corrections therefore are expected, otherwise, after a certain time, roundoff errors will be dominant. The simplest extension of the microcanonical ensemble is the (NVT) canonical ensemble, where the number of atoms, the volume and the temperature are fixed to prescribed values. The temperature T is, in contrast to N and V, an intensive parameter. The extensive counterpart would be the kinetic energy of the system [65].

Several thermostat methods have been proposed to control the temperature during MD simulation. With these methods, the molecular system is coupled to a heat bath to ensure that the average system is maintained close to the requested temperature with a certain fluctuation. When this is done the equations of motion are modified and the system no longer samples the microcanonical ensemble (NVE). Instead, trajectories in the canonical ensemble (NVT) or something close are generated. There are three thermostat methods that are widely used: Andersen, Berendsen and Nose-Hoover thermostats (More details are given in the Appendix "Thermostat algorithms of MD simulations"). Of these only the Nose-Hoover algorithm generates trajectories in the genuine canonical ensemble (NVT), and is used in our MD simulations [54, 66].

2.4 Molecular simulation of carbon nanotubes

In recent years, modelling methods based on molecular simulation have become a useful tool in scientific research. To some extent, molecular simulations have filled the long existing gap between experimental and theoretical divisions of natural sciences such as physics, chemistry and pharmacy. The structure of carbon nanotubes is well defined, and suitable for molecular simulation. The earliest molecular simulations of carbon nanotubes were reported in the mid-90s of the last century [67] and since then a lot of simulations have been implemented to investigate the properties and applications of carbon nanotubes.

In general, there are three categories of molecular simulation methods for carbon nanotube (or carbon nanotube-organic molecule) systems: *ab initio* quantum mechanics [68, 69], reactive empirical bond order (REBO) potentials [61, 70], and classical molecular dynamics (MD) [71–73]. *Ab initio* quantum mechanics calculations are a common approach and usually give more accurate results than the other two methods, but they are computationally expensive for large

molecular systems. Calculations based on REBO potentials and classical MD are much faster than those using *ab initio* quantum mechanics. For studies where no change in intramolecular chemical bonding takes place, classic MD is effective to simulate carbon nanotubes. However, it is unable to investigate some radical deformations of carbon nanotubes involving chemical bond construction and destruction such as the fracture and buckling of carbon nanotubes, in which case, the calculation should be based on REBO potentials.

2.5 Summary

Molecular simulation already has become an indispensable tool in materials design, drug discovery and more. Because of their small size at a scale of around a nanometre, the study of carbon nanotubes becomes a big challenge for traditional methods. Simulation methods such as MM and MD are promising approaches to investigate the mechanical properties of carbon nanotubes. In this chapter, we mainly talked about the basic principles of MM and MD. The techniques used in our simulations of carbon nanotubes are stated, especially, MM3 force field and REBO potential (Brenner's potential) are explained in detail.

Chapter 3
Young's modulus and buckling strength of SWNT with/without defects

3.1 Introduction

A lot of theoretical study of elastical properties of defect free SWNT have been carried out with continuum theory [74, 75]. In this chapter, we mainly focus on SWNT with atomic defects. The atomic defects have great influence on the elastical properties of SWNT, and SWNT always tend to fail around defect sites. The continuum model is unable to describe defects at a atomic scale. From previous research [45, 76, 77], MM based on MM3 force field has been proven to give a total potential energy of a carbon nanotube that is in good agreement with the more accurate tight-binding density-functional theory (DFT), which is computationally demanding and only suited to small molecular systems. Therefore, in this chapter, molecular simulations with MM3 force field are empolyed to study the SWNT with defects.

3.2 Simulation of SWNT under axial load

3.2.1 Method

To simulate SWNT compression, we carry out a sequence of small compression steps. For every step, we move the atoms at both ends of a carbon nanotube by a small amount (0.01 Å per step) in the axial direction towards the centre of SWNT. Then we optimise the deformed SWNT geometry with the Quasi-Newton method down to a root mean square (rms) deviation <0.1 kcal/mol (≈ 0.004 eV), while the potential energy increases around 0.5 eV after a step. During geometry optimisation, a springlike harmonic restraint is applied to the atoms at the ends to prevent the SWNT from restoring its initial structure (structure of the lowest potential energy):

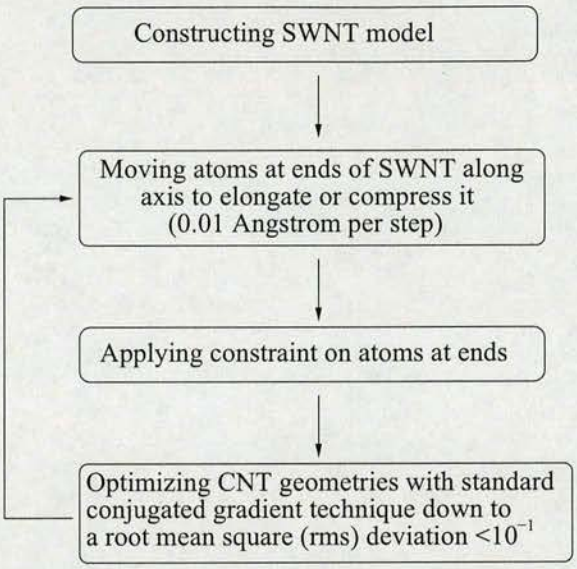

Figure 3.1: *Computation scheme for SWNT elongation and compression*

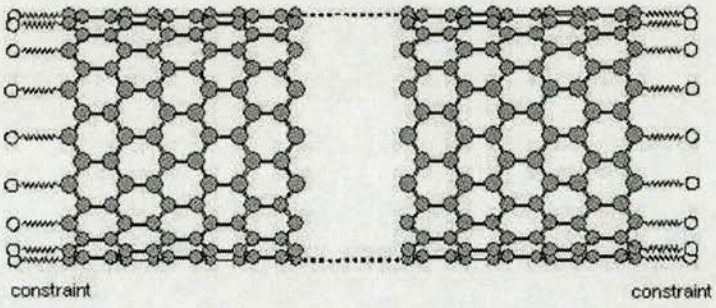

Figure 3.2: *SWNT under axial load*

$$\mathbf{F_c} = \begin{cases} k(\mathbf{r} - \mathbf{r}_0) & |\mathbf{r} - \mathbf{r}_0| > r_c, \\ \mathbf{0} & |\mathbf{r} - \mathbf{r}_0| < r_c, \end{cases} \tag{3.1}$$

where k= 20000 kcal/Å^2, and r_c=0.0005 Å. With the force constant k, the atoms at the ends are almost fixed to their positions. With the parameter r_c, we define a small sphere around $\mathbf{r}_0$ within which the constraint force is zero, to enable these atoms to move around $\mathbf{r}_0$.

In the simulation of carbon nanotube compression we do not directly increase the forces on the two ends of a carbon nanotube like in normal tensile experiments on materials. Instead we just gradually move the end atoms at fixed steps. From Equation 3.1, we can see that the constraints on the atoms at the ends are spring-like external forces. On the other hand, there must be forces

from the carbon nanotube to resist the deformation. As a result there is a force equilibrium at the ends between the external forces and those from the carbon nanotube. Together with the diameter of a SWNT, we can obtain the stress within the carbon nanotube. The calculation method of the stress will be discussed below in section 3.2.3.

3.2.2 Modified MM3 force field

The energetics of SWNT deformation under compressive loading is determined with MM with a modified MM3 force field. The total molecular potential energy E of a SWNT is expressed as a sum of several individual energy terms

$$E = E_s + E_\theta + E_\omega + E_{s\theta} + E_{\omega s} + E_{\theta\theta'} + E_{vdw} \ , \tag{3.2}$$

where E_ω, $E_{s\theta}$, $E_{\omega s}$ and $E_{\theta\theta'}$ are energies associated with torsion, stretch-bending interaction, torsion-stretch interaction and bend-bend interaction, and E_{vdw} denotes the energy associated with van der Waals interaction. Of these, the major contribution to the total molecule potential energy comes from the E_s and E_θ terms.

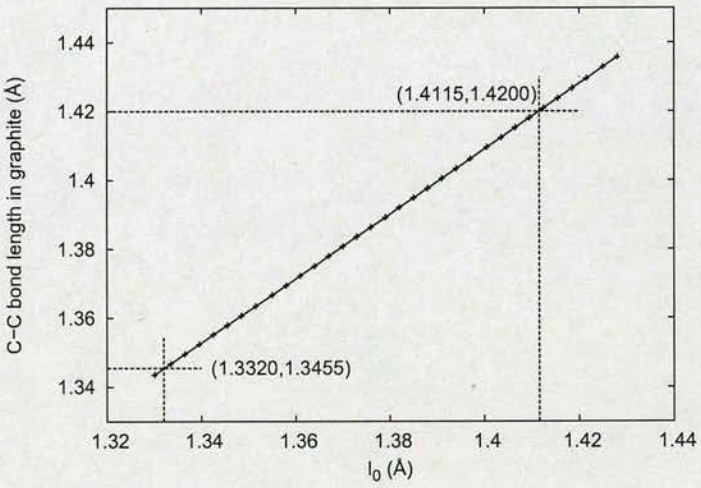

Figure 3.3: *The relationship between l_0 and C-C bond length of graphite*

In the original MM3 force field, the equilibrium bond length is about 1.3320 Å fitted from alkenes. With this bond parameter, the bond length of graphite will be equal to 1.3455 Å,

which is smaller than that measured experimentally. The equation for bond energy is

$$E_s = 71.94k_s(l - l_0)^2 \left[1 - 2.55(l - l_0) + (7/12)2.55(l - l_0)^2\right]. \tag{3.3}$$

To get a desirable equilibrium structure of carbon nanotubes in simulations, a series of simulations have carried out with different values of l_0, and the result is shown in Figure 3.3.

In some literature references [76, 77], the MM3 force field was modified for carbon nanotubes simulation by simply setting l_0 to the C-C bond length of the graphite. From our calculation, it is clear that if we want to obtain a desirable structure of graphite we should set l_0 to 1.4115 rather than 1.420 Å. Therefore, with the modified MM3 force field, the equilibrium bond length of graphite approximately equals 1.420 Å in agreement with the experimental result [78]. The

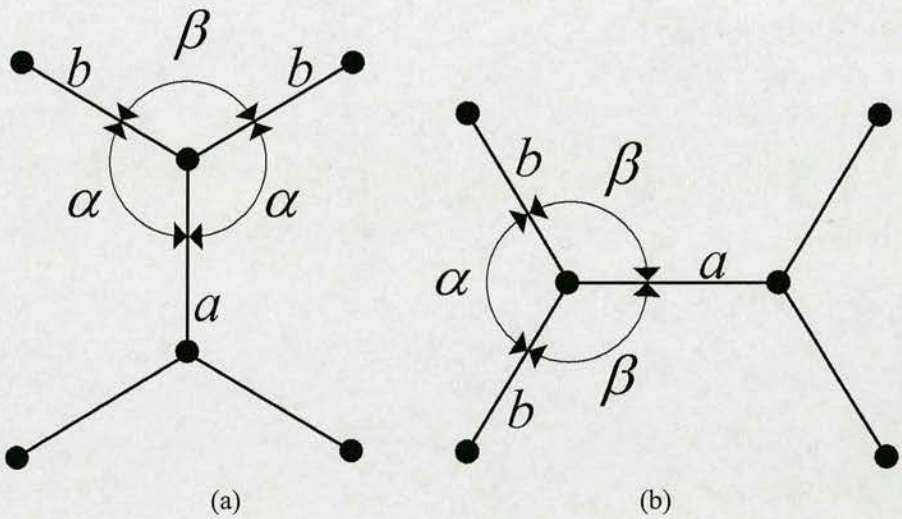

Figure 3.4: *Bond lengths and bond angles around a representative atom: (a) for armchair SWNT and (b) for zigzag SWNT*

carbon bond length is 1.42 Å and the bond angle is 120° for every carbon atom on graphite. Unlike a graphene, a carbon atom and its three nearest-neighbour atoms on a carbon nanotube form a tetrahedron because of the curvature effect. Therefore, the carbon bonds on a carbon nanotube may have different lengths and angles, depending on the bond orientation and the diameter of the carbon nanotube. Figures 3.5 and 3.6 show the results of bond lengths and angles prior to deformation for zigzag and armchair carbon nanotubes of different diameter. It is observed that for carbon nanotube diameters above 14 Å, the bond lengths and angles are essentially the same as those of graphite (within 1% difference) such that the carbon nanotube

curvature has little effect. However, for the carbon nanotubes with a diameter smaller than 14 Å, the effect of carbon nanotube curvature is significant.

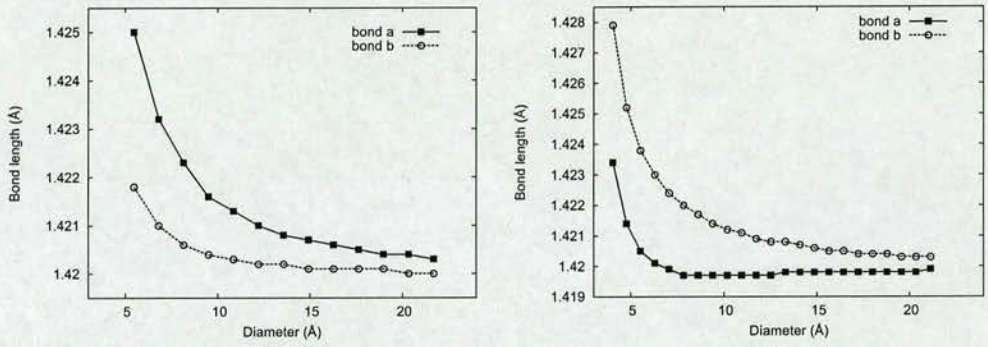

Figure 3.5: *Bond lengths around a representative atom: (a) for armchair (n,n) nanotube and (b) for zigzag (n,0) nanotube.*

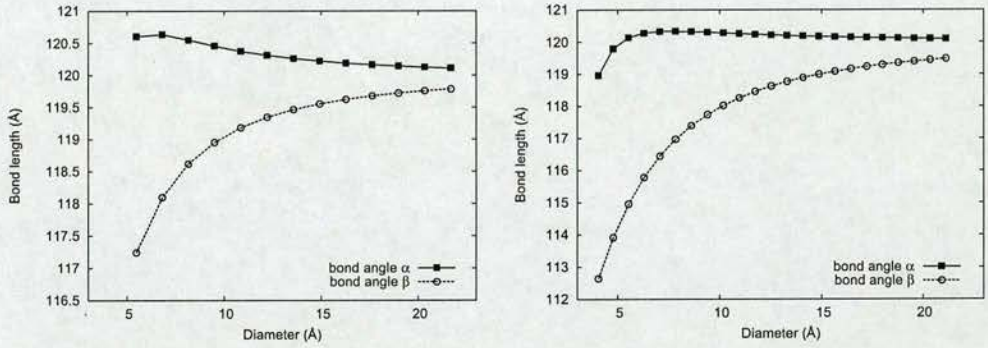

Figure 3.6: *Bond angles around a representative atom: (a) for armchair (n,n) SWNT and (b) for zigzag (n,0) SWNT.*

3.2.3 Potential and stress of SWNT

The energetics of the deformed SWNT are determined with MM using the TINKER program [79] with the modified MM3 force field.

For every deformed SWNT, we can calculate its total potential energy after relaxation. Figure 3.7 shows the variation of the total potential energy versus the tensile strain during tension or compression of zigzag (11, 0) SWNT. Under tensile load, the total potential energy of a SWNT increases monotonically, whereas under compressive load, after a similar constant increase the total potential energy of SWNT encounters a abrupt decrease when buckling occurs

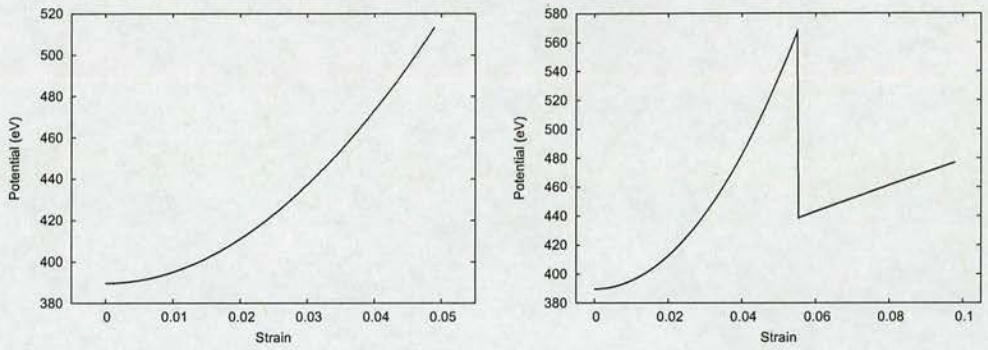

Figure 3.7: *Potential energy of SWNT under axial load: (a) elongation and (b) compression*

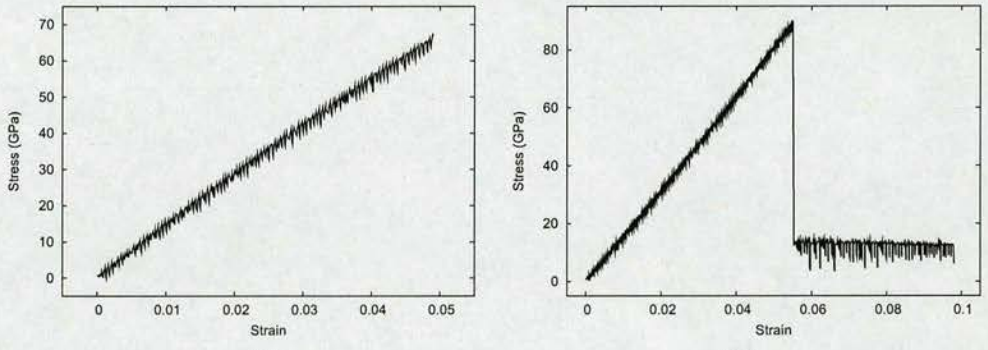

Figure 3.8: *Stress of SWNT under axial load: (a) elongation and (b) compression*

at a critical compressive strain. We cannot simulate failure of SWNT under tensile load using the MM3 force field because the bond connection in this force field cannot be changed during computation, consequently, there is no bond destruction and therefore no fracture. The simulation of fracture of SWNT requires the use of REBO and is discussed in the next chapter.

The total potential energy of a compressed SWNT can be expressed as [80]

$$\Pi = U - W, \tag{3.4}$$

where W is the virtual work of the axial load force F, and U is the total potential energy of the SWNT. The principle of minimum potential energy is written as

$$\delta\Pi = \delta(U - W) = \delta U - F\delta l = 0, \tag{3.5}$$

where δl is the variation in SWNT length. We can conclude $F = \delta U/\delta l$, at $\delta\Pi = 0$. Therefore, we can get the force applied to SWNT from the derivative of its total potential energy with respect to its length change during tension or compression. Figure 3.8 shows the variation of the stress versus the tensile strain during elongation and compression for a zigzag (11, 0) SWNT.

3.3 Young's modulus and Poisson's ratio of SWNT

A series of simulations of SWNT deformation have been carried out. To simulate tension of SWNT, we carry out stepwise elongation up to 500 steps, and the final engineering strain is about 0.05. Zigzag (n, 0) (n=6, 7, ..., 27) and armchair (n, n) (n=5, 6, ..., 16) SWNT are studied. The diameter range is from 4.8 to 21.7 Å, and the length is around 200 Å for all SWNT.

3.3.1 Calculation of Young's modulus and Poisson's ratio of SWNT

The Young's modulus (also known as the modulus of elasticity or elastic modulus) is a material property that describes elastic stiffness and is one of the most important mechanical properties in materials study. In our study, we investigate the longitudinal and surface Young's modulus of SWNT. The longitudinal Young's modulus of the SWNT can be defined as the slope of the engineering stress-strain curve. By envisaging the SWNT as a shell with diameter R and thickness t or a solid cylinder with radius R, the longitudinal Young's modulus of SWNT E_{11} or $\overline{E}_{11}$ can be written as

$$E_{11} = \frac{F}{2\pi R t \varepsilon_{11}} \quad \text{or} \quad \overline{E}_{11} = \frac{F}{\pi R^2 \varepsilon_{11}}. \tag{3.6}$$

The modulus based on the association with a solid cylinder is also called the effective modulus of SWNT, which is indicated by an overbar. The definition of the major Poisson's ratio of the SWNT does not require a thickness, it can be defined as

$$\mu_{12} = -\frac{\varepsilon_{22}}{\varepsilon_{11}}, \tag{3.7}$$

where ε_{11} and ε_{22} represent the axial strain and the radial strain of SWNT, respectively. The surface Young's modulus, denoted as E^s_{11}, is the ratio of the axial force per length over the

perimeter and the axial strain, ie.

$$E_{11}^{s} = \frac{F}{2\pi R\varepsilon_{11}}. \tag{3.8}$$

The relationships between the Young's moduli based on various definitions can be written as follows:

$$E_{11} = \frac{E_{11}^{s}}{t} \quad \text{and} \quad \overline{E}_{11} = \frac{E_{11}^{s}}{R/2}, \tag{3.9}$$

where ε is the engineering strain, and F is the force applied to the two ends of the SWNT.

3.3.2 Effective longitudinal Young's modulus of SWNT

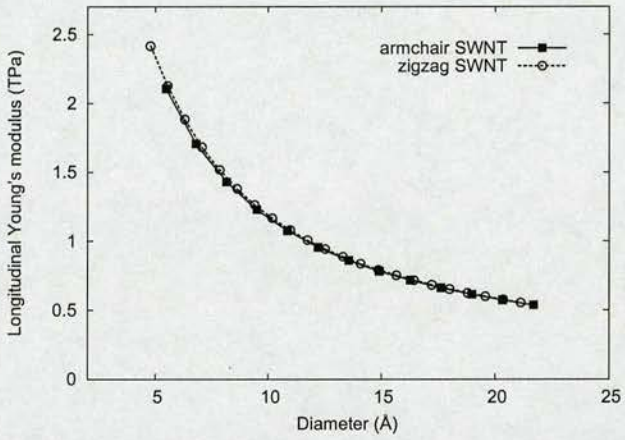

Figure 3.9: *Effective longitudinal Young's modulus of SWNT*

The effective longitudinal Young's modulus of SWNT of different diameter is plotted in Figure 3.9. It is very clear that the Young's modulus decreases with increasing diameter of SWNT because we use the whole cross section of the SWNT for stress calculation. The Young's moduli of simulated SWNT range from $0.5 \sim 2.4$ TPa, which agrees well with results $0.32 \sim 1.47$ TPa from AFM experiments [33]. The longitudinal Young's moduli of armchair and zigzag SWNT almost overlap, i.e., there is no significant difference in effective longitudinal Young's modulus caused by SWNT chirality.

3.3.3 Surface longitudinal Young's modulus of SWNT

We can directly calculate the surface longitudinal Young's modulus of SWNT from their effective longitudinal Young's modulus according to Equation 3.8. The variation of the surface longitudinal Young's modulus with diameter is plotted in Figure 3.10. It is clear that the sur-

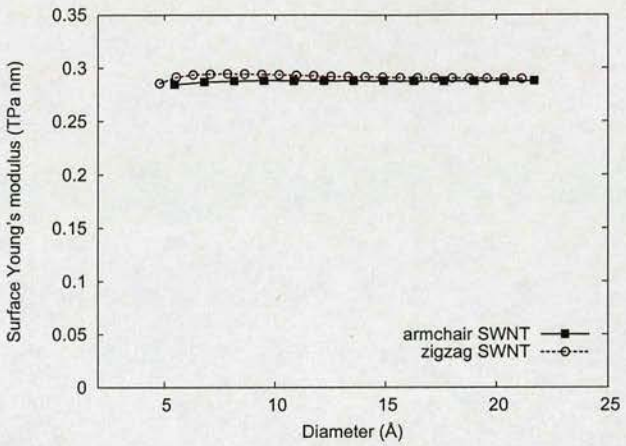

Figure 3.10: *Surface longitudinal Young's modulus of SWNT*

face longitudinal Young's modulus of SWNT is about 0.29 TPa·nm for all SWNT of different diameter and chirality, with variance about 3.0%.

In some studies of mechanical properties of SWNT, a fixed thickness of 3.4 Å is used to calculate the longitudinal Young's modulus E_{11} [45]:

$$E_{11} = E_{11}^{s} \times t, \tag{3.10}$$

where t=3.4 Å is the thickness of SWNT. With $E_{11}^{s} \approx$0.29 TPa·nm we obtain the Young's modulus E_{11} of 0.85 TPa for all SWNT according to Equation 3.10.

3.3.4 Poisson's ratio of SWNT

According to Equation 3.7, we can calculate the Poisson's ratio of SWNT under tensile load. The variation of Poisson's ratios of armchair (6,6) and zigzag (10,0) SWNT with strain is plotted in Figure 3.11. Apart from the numerical fluctuations at the onset of deformation, the Poisson's ratios decrease linearly with strain.

To compare the Poisson's ratio of SWNT of different diameter, we use the Poisson's ratio at a strain of 0.04. The Poisson's ratio of SWNT is shown in Figure 3.12. It is clearly seen that the Poisson's ratio of SWNT depends significantly on their diameter and chirality. For armchair SWNT, the Poisson's ratios are between 0.223 and 0.234, and gradually increase with their diameter. For zigzag SWNT studied, their Poisson's ratios are between 0.198 and 0.227,

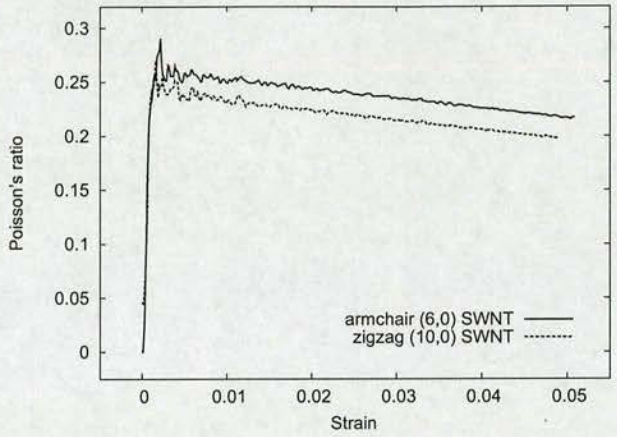

Figure 3.11: *Poisson's ratio of armchair (6,6) and zigzag (10,0) SWNT*

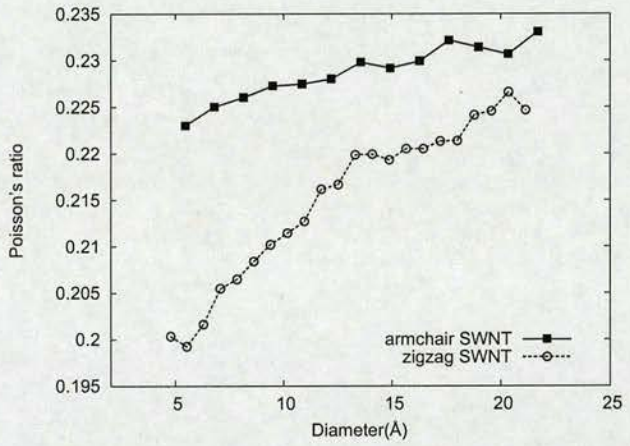

Figure 3.12: *Poisson's ratio of SWNT*

and increase more strongly with diameter. Generally, the Poisson's ratio of armchair SWNT is larger than that of zigzag SWNT, but the difference caused by chirality becomes smaller with increasing diameter.

The longitudinal Young's moduli of SWNT without defects between 0.5 and 2.4 TPa and Poisson's ratios around 0.23 are in a good agreement with the values reported in the literatures [31, 80, 81].

3.4 Buckling of SWNT

3.4.1 SWNT under compressive loading

Under compressive loads, SWNT fail in form of buckling. Initially deformation is homogeneous: the length decreases gradually, and the radius increases accordingly. When SWNT are compressed to some extent, without exception they will buckle. The continuum theory of shells explains that buckling occurs due to instabilities governed by elastic energy [38]. The energy of a shell can be expressed as a surface integral of the quadratic form of deformation and instability occurs because buckling tends to decrease energy above a critical strain. The continuum theory of buckling instabilities envisages small perturbations from the original shape which is decomposed into Fourier harmonics. SWNT are, however, at the limit of applicability of this type of analysis since the Fourier wavelengths are not large as compared to the inharmonic spacing. This is even more evident if localized perturbations (defects) are considered. Hence, a systematic study based on atomistic simulation can yield useful insights into the collapse process.

A series of simulations of compression of defect free SWNT have been carried out. The final strain is about 0.10. "Zigzag" (n, 0) (n=6, 7, . . ., 27) and "armchair" (n, n) (n=5, 6, . . ., 16) SWNT have been studied. The diameter range is from 4.8 to 21.7 Å, and the length is around 200 Å for all SWNT.

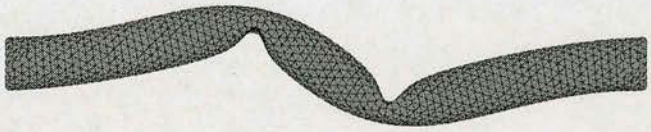

Figure 3.13: *Buckling of SWNT*

As we can see from Figure 3.13, the initially "perfect" circular structure of SWNT is elastically deformed and buckles under compression. We find that the buckle begins to appear at a critical applied strain, and radically changes the circular cross-sectional structure of the SWNT as the load increases.

3.4.2 Buckling strength of SWNT

From the study of potential energy of SWNT, we can see that there is an abrupt jump in stress when SWNT buckle. We can calculate the force F applied to SWNT from Equation 3.5, and if

we regard SWNT as solid cylinders, the buckling stress τ_c can be obtained as

$$\tau_c = \frac{F_c}{\pi R^2}, \tag{3.11}$$

where F_c is the peak force applied at the point of buckling, and R is the radius of SWNT.

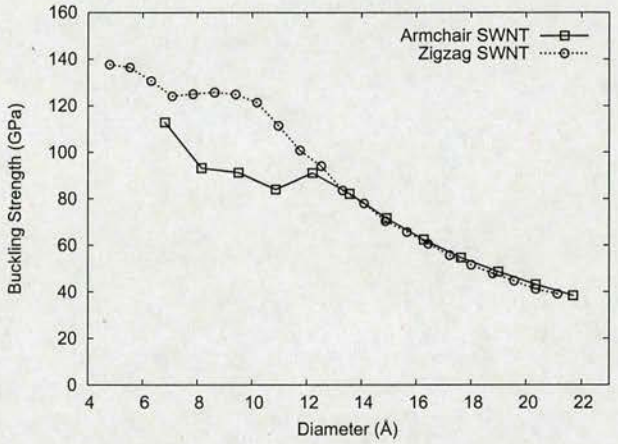

Figure 3.14: *Buckling strength of SWNT*

The buckling stress of all samples is shown in Figure 3.14. The buckling strength of a SWNT decreases with increasing SWNT diameter. For SWNT of small diameter, the buckling strength is as high as 140 GPa ((4,0) zigzag SWNT), and decreases to 40 GPa when the diameter is as large as 22 Å. For SWNT of diameter smaller than 14 Å, the buckling strength of zigzag SWNT is generally larger than that of armchair SWNT. For SWNT of diameter larger than 14 Å, the buckling strengths of armchair and zigzag SWNT are approximately equal, and the topology has little influence.

3.4.3 Buckling modes of SWNT under compressive load

From our simulations, we find that the buckling behaviour of a SWNT depends on their diameter. SWNT of small diameter bend like rigid beams, while those of larger diameter buckle like shells. We now study the configuration of SWNT in some detail to see their different failure modes under compressive load.

To investigate the details of configuration change during compression, we monitor the change of cross sections of SWNT with strain. The zigzag SWNT we used have all the same length, and each of them has 96 cross sections along its axis. We use the mean radius R_g to characterise

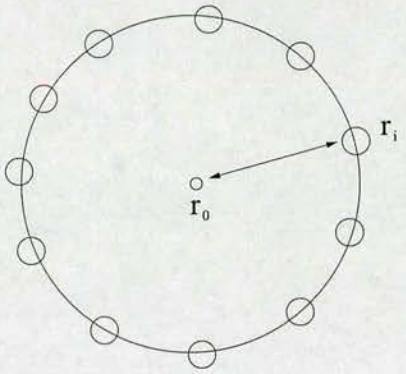

Figure 3.15: *Cross sections of SWNT*

the distribution of carbon atoms on a cross section as shown in Figure 3.15:

$$R_g = \sqrt{\frac{1}{N}\sum_{i=1}^{N}(\mathbf{r}_i - \mathbf{r}_0)^2}. \tag{3.12}$$

Here N is the number of atoms in the cross section, $\mathbf{r}_0$ the centre of gravity of the atoms, $\mathbf{r}_i$ the position of atom i.

Figure 3.16 and 3.17 show the buckling structures of two simulated SWNT with different diameter under compression. It is clear that both SWNT undergo a similar homogeneous deformation before they buckle, while the buckling structure of SWNT depends on their diameter. According to Markus J. Buehler *et al*, the buckling behaviour of SWNT can be classified into three buckling modes [44]:

The first mode is "Euler buckling", which happens to SWNT of small diameter. After a homogeneous deformation, at some critical strain the SWNT will bend like rigid beams, and at the same time there is an inhomogeneous change of their circular structure, which can be seen through calculation of their mean cross-sectional radius as shown in Figure 3.16. The mean radius can decrease by up to 8% in the parts of SWNT where the buckling happens.

The second mode is "shell buckling", which happens to SWNT of large diameter. Like "Euler buckling", SWNT of this buckling mode also undergo a homogeneous deformation in the early stage of compression. Then at some critical strain, the SWNT will buckle and their configurations deform radically in some parts, as localized "folds" develop. The configuration of SWNT after buckling in this mode is different from that in the first mode. The difference is clear if we

Zigzag(10,0) SWNT snapshot at strain≈8%

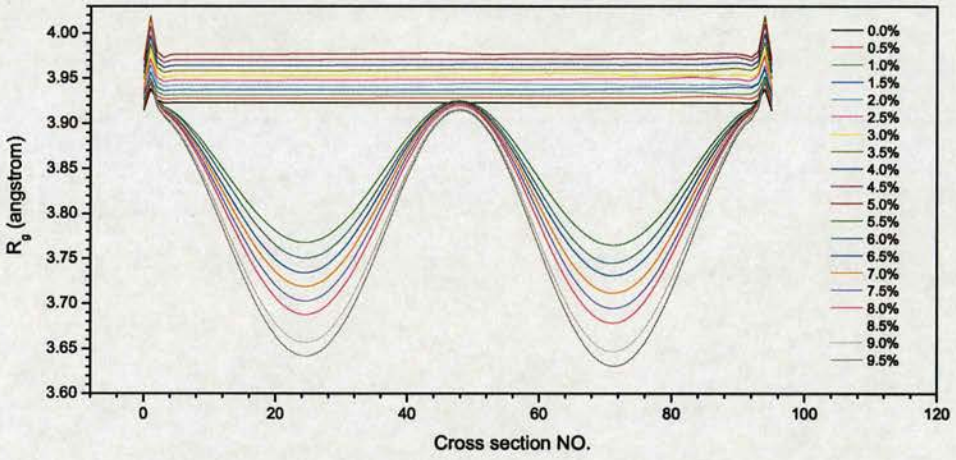

Figure 3.16: *Buckling section gyration radius of zigzag(10,0) SWNT d=7.85 Å*

Zigzag(25,0) SWNT snapshot at strain≈8%

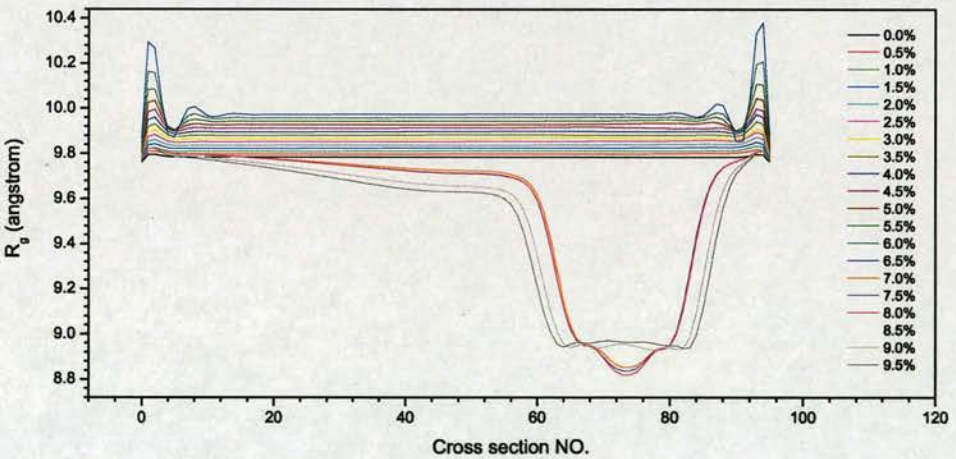

Figure 3.17: *Buckling section gyration radius of zigzag(25,0) SWNT d=19.6 Å*

compare Figure 3.16 with Figure 3.17.

Another buckling mode is "wire-like buckling", which is not seen from our simulations, because the SWNT we studied are only about 200 Å in length and the aspect ratios are from about 10 to 40 only. This buckling mode only happens to long SWNT of large aspect ratio. It is observed in simulations of long (4,4) and (8,8) armchair SWNT. The lengths of the SWNT range from 150 to 350 nm, which refers to aspect ratios up to 580. It is indicated that "wire-like buckling" not only appears in very thin SWNT, but also in SWNT with larger diameters provided the aspect ratio is sufficiently large [44]. In wire-like buckling, the SWNT do not develop cross-sectional heterogeneity but instead coil up like a spring.

Euler buckling

SWNT	(4,4)	(5,5)	(6,6)	(7,7)	(8,8)	(9,9)	(10,10)
Diameter (Å)	5.47	6.81	8.15	9.50	10.9	12.2	13.6

Shell buckling

SWNT	(11,11)	(12,12)	(13,13)	(14,14)	(15,15)	(16,16)
Diameter (Å)	14.9	16.3	17.6	19.0	20.3	21.7

Table 3.1: *Different buckling modes of armchair SWNT under compressive load*

Euler buckling

SWNT	(6,0)	(7,0)	(8,0)	(9,0)	(10,0)	(11,0)
Diameter (Å)	4.78	5.53	6.30	7.07	7.85	8.62
SWNT	(12,0)	(13,0)	(14,0)	(15,0)	(16,0)	(17,0)
Diameter (Å)	9.40	10.2	11.0	11.7	12.5	13.3

Shell buckling

SWNT	(18,0)	(19,0)	(20,0)	(21,0)	(22,0)
Diameter (Å)	14.1	14.9	15.6	16.4	17.2
SWNT	(23,0)	(24,0)	(25,0)	(26,0)	(27,0)
Diameter (Å)	18.0	18.7	19.6	20.4	21.1

Table 3.2: *Different buckling modes of ziagzag SWNT under compressive load*

It is also noticed that some SWNT of "Euler buckling" mode exhibit post-buckling instabilities if loading continues. The snapshots and mean radius of an armchair (6,6) SWNT under compressive load are shown in Figure 3.18. The SWNT buckles at a strain $\approx 4.0\%$, and at strain $\approx$ 6.5% undergoes a post-buckling instability leading to the emergence of the localised folds.

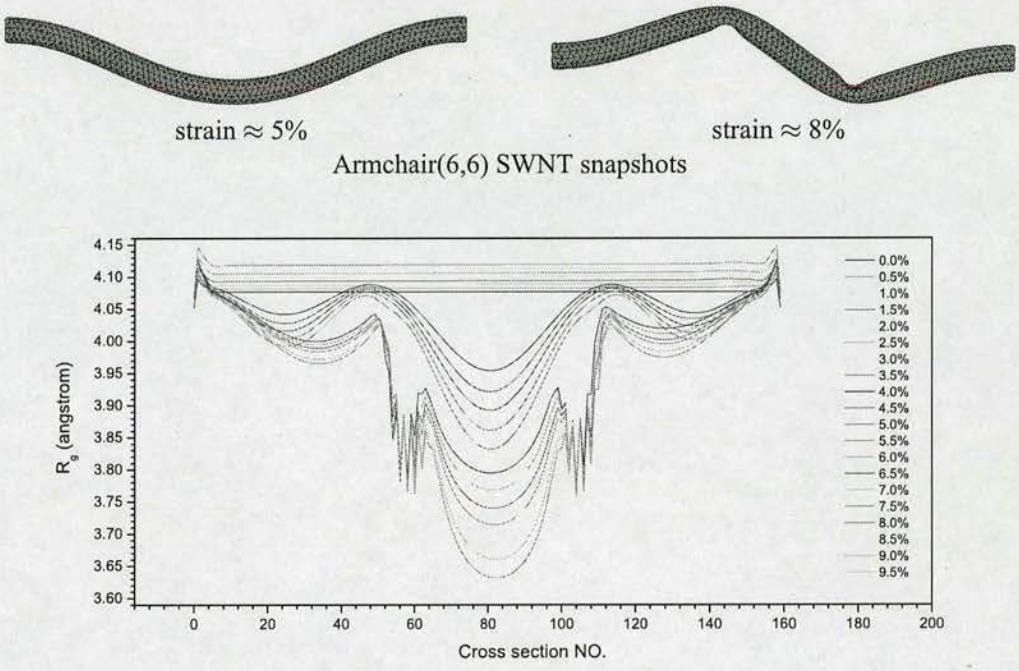

Figure 3.18: *Buckling section gyration radius of armchair (6,6) SWNT d=8.15 Å*

3.4.4 Critical strain of SWNT buckling

As shown in Figure 3.19, the critical strain of SWNT buckling is dependent on SWNT diameter and chirality. All of the SWNT in the study start to buckle at strains below 8.0%. From AFM experiments, it is estimated that the onset buckling strain of a carbon nanotube to be about 5.0% after analyzing a large number of buckled nanotubes embedded in polymer matrix [82]. For armchair SWNT, the critical strain increases with SWNT diameter, reaches the maximum at a diameter about 15 Å, and afterwards decreases with SWNT diameter. For zigzag SWNT, the critical strain also increases with SWNT diameter, reaches the maximum at a diameter around 13 Å, and afterwards decreases with SWNT diameter.

Generally, the critical strain of zigzag SWNT is larger than that of armchair SWNT, while for SWNT of diameter larger than 15 Å there is no significant difference in critical strain between armchair and zigzag SWNT.

We can qualitatively explain the variation of the buckling strain of SWNT in the context of elasticity theory. For a clamped rod with length L and flexural rigidity $D = EI$, the critical

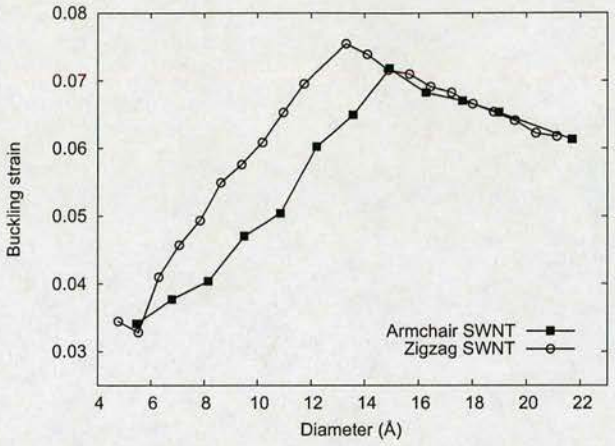

Figure 3.19: *Critical strain of SWNT buckling*

buckling load is [36, 44]

$$F_c = \pi^2 \frac{4D}{L^2}. \tag{3.13}$$

This critical load is inversely proportional to the square of the length and proportional to the flexural rigidity. The flexural rigidity is linearly proportional to the Young's modulus of the material, $D \propto E$, and is related to the radius of rod according to $D \propto R^3$ (geometrical moment of inertia). The critical load and critical strain are, therefore,

$$F_c \propto \frac{R^3}{L^2} \quad \text{and} \quad \varepsilon_c \propto \frac{R^2}{L^2}. \tag{3.14}$$

The critical strain of the "Euler buckling" buckling mode follows the Equation 3.14.

The second mode is "shell buckling", which happens to SWNT of diameter larger than about 14.0 Å (armchair SWNT 14.5 Å and zigzag SWNT 13.5 Å). As discussed in [36], the critical strain for "shell buckling" depends on shell radius R like

$$\varepsilon_s \propto \frac{1}{R}. \tag{3.15}$$

With Equation 3.14 and 3.15, we can see that the critical strain will increase with increasing SWNT diameter if the buckling mode is "wire-like buckling" or "Euler buckling", while for SWNT of large diameter the buckling mode is "shell buckling" and the critical strain will decrease with increasing diameter. Without further investigation, it is not clear if the critical strain will strictly observe the Equation 3.14 and 3.15. However, from Figure 3.19, we can see: for both armchair and zigzag SWNT, the critical strain linearly increases with increasing SWNT

diameter for SWNT of "Euler buckling" mode; the critical strain monotonically decreases with increasing diameter for SWNT of "shell buckling" mode, which agrees qualitively with the Equations 3.14 and 3.15.

3.5 Defects of SWNT

Most of studies on SWNT regard them as "ideal" carbon nanotubes. However, several years after the discovery of carbon nanotubes, people found out that defects on carbon nanotubes are very common and have great influence on their properties, especially mechanical properties [35, 50, 83–85]. There are several kinds of defects thought to occur to carbon nanotubes. For simplicity, we only studied three kinds of well-defined defects: functionalization defects caused by chemical functionalization [86–91], topological defects (5-7-7-5 defects) [28, 83, 92], and structural defects (vacancies) [93] as shown in Figure 3.20. For any model of defective SWNT, only one kind of defect was considered.

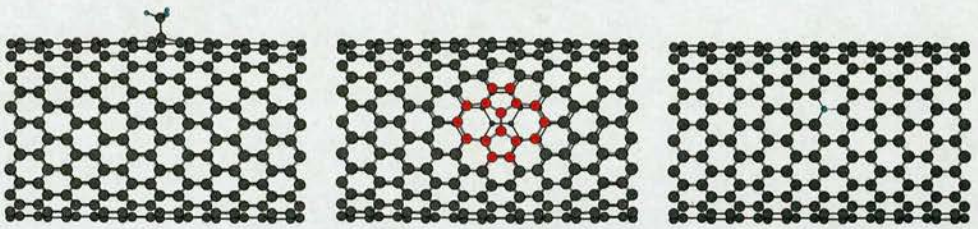

Figure 3.20: *Defects on SWNT (segment): (a) functionalization defect, (b) 5-7-7-5 defect, (c) vacancy*

To simulate SWNT with functionalization defect(s), we chemically attach one or more methyl groups to the SWNT, and accordingly the SWNT atom attached by methyl group changes its type of hybridisation from sp^2 to sp^3 as shown in Figure 3.20 (a).

To simulate SWNT with 5-7-7-5 defect(s), we just change the topological connections among the atoms. For one 5-7-7-5 defect, four adjacent hexagons are replaced by two pentagons and two heptagons as shown in Figure 3.20 (b).

To simulate SWNT with vacancy(ies), we take one or more carbon atoms from the SWNT. Each vacancy will directly have influence on the geometry of three adjacent hexagons as shown in Figure 3.20 (c).

The defects are regularly distributed on SWNT to avoid aggregation of defects. All the defect models are optimised via energy minimisation with MM to obtain stable initial configurations for further simulation.

3.6 Simulation of SWNT with defects under axial load

From our simulations, we find that defects have great influence on the buckling behaviour of SWNT, and the buckling always happens near the site of a defect. For example, we investigate the relationship between defect sites and buckling sites of zigzag (6,0) and (16,0) SWNT, which only contain a single defect.

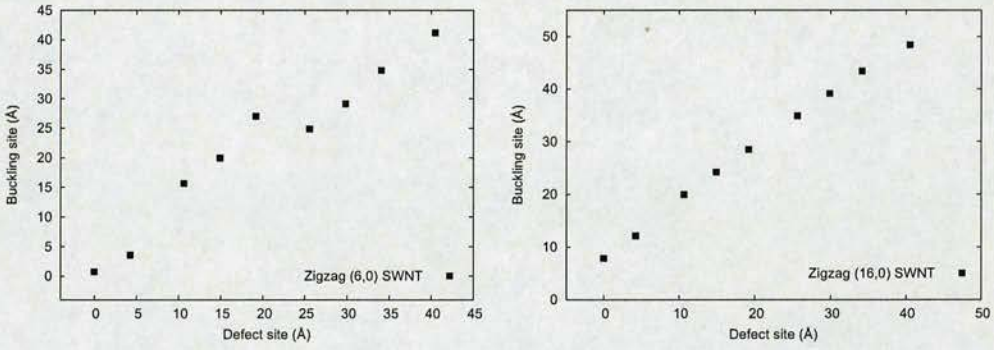

(a) (b)

Figure 3.21: *The relationship between defect site and buckling site: (a) zigzag (6,0) SWNT (diameter: 4.78 Å), (b) zigzag (16,0) SWNT (diameter: 12.5 Å).*

The defect site is the position where the defect is located on a SWNT when there is no deformation, and we use the distance from the site to the middle of the SWNT along its axis to specify the place. Since all the atoms of the SWNT will displace during deformation, the defect site will shift away from the middle of the SWNT. The buckling of SWNT will involve more than one atom, and it tends to happen around the defect site. We check the sections around the buckling site, we calculate the mean radius of the section with Equation 3.12. The mean radius has a maxium change around the centre of the buckling site. From Figure 3.21, it is clear that buckling tends to take place around the defect no matter where the defect is located (a defect site of 0 Åcorresponds to a defect in the middle of the SWNT).

As in the simulations of SWNT without defect, a series of simulations of elongation and compression has been carried out. To simulate the tension of SWNT, we carry out stepwise elongation up to 500 steps, and the final strain is about 0.05. To simulate compression of SWNT, we

carry out up to 1000 steps to make sure that buckling happens to every SWNT in study, and the final strain is about 0.10. The defected SWNT models used include zigzag (n, 0) (n=6, 7, . . ., 27) and armchair (n, n) (n=5, 6, . . ., 16) SWNT.

3.7 Influence of defects on Young's modulus and buckling strength of SWNT

3.7.1 Influence of defects on Young's modulus of SWNT

The Young's modulus and buckling strength of the SWNT are examined. Because the surface Young's modulus of SWNT can be calculated from their longitudinal Young's modulus and their diameter, in the following study, we only investigate their longitudinal Young's modulus, in short, denoted Young's modulus.

Figures 3.22, 3.23 and 3.24 show the Young's modulus of the SWNT with or without defects. Generally, introducing any of the three kinds of defects will slightly decrease the elastic modulus of SWNT, but if only a small amount ($< 2\%$) of SWNT atoms are functionalized, the elastic modulus of functionalized SWNT is a little higher than that of pristine SWNT. The variations of elastic moduli of zigzag and armchair SWNTs are almost the same.

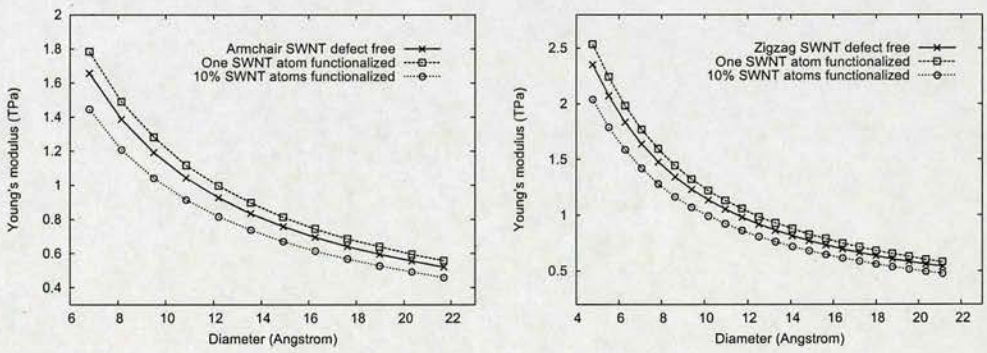

(a) (b)

(a) armchair SWNT, (b) zigzag SWNT

Figure 3.22: *Young's modulus of functionalized SWNT*

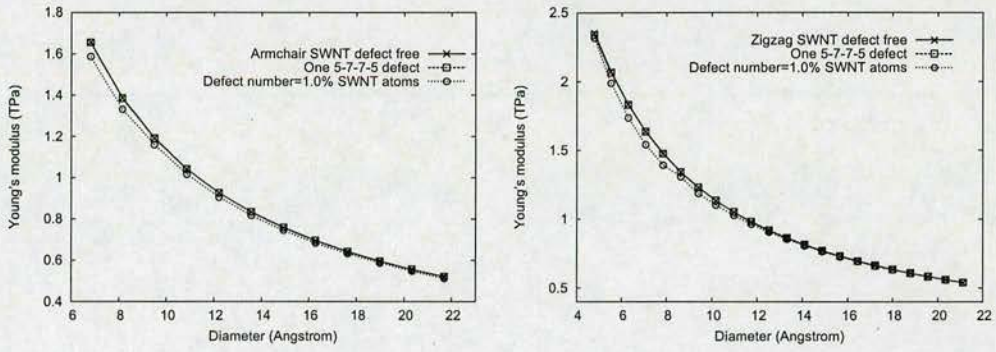

(a) (b)

(a) armchair SWNT, (b) zigzag SWNT

Figure 3.23: *Young's modulus of SWNT with 5-7-7-5 defects*

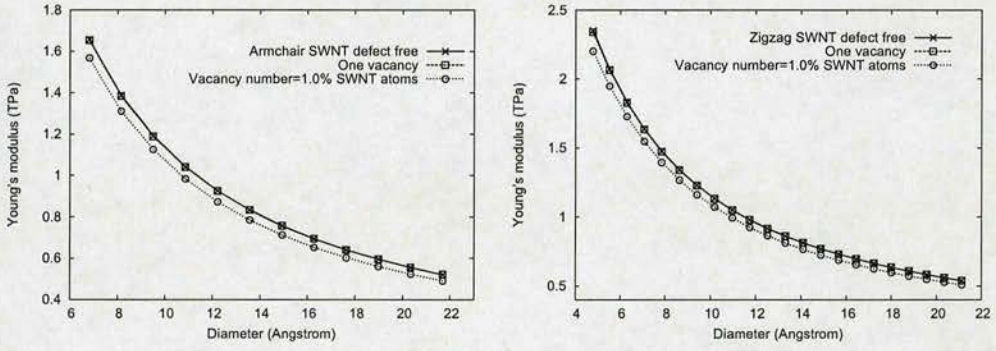

(a) (b)

(a) armchair SWNT, (b) zigzag SWNT

Figure 3.24: *Young's modulus of SWNT with vacancies*

3.7.2 Influence of defects on buckling strength of SWNT

Figures 3.25, 3.26 and 3.27 show the buckling stress of SWNT with or without defect(s). In contrast to Young's modulus, SWNT of different chirality usually have different buckling strength. It is clear that the buckling strength of SWNT is greatly decreased after introducing any one of the three kinds of defects investigated. For example, if 10% SWNT atoms are functionalized with methyl groups, the buckling strength will be decreased by 30% or more as shown in Figure 3.25. Even one defect can have significant influence on the buckling strength for SWNT with small diameter (<14 Å). For SWNTs with larger diameter (>14 Å), although their buckling stress is not so sensitive to one defect as that of SWNTs with smaller diameter, the buckling strength also deteriorates with increasing defect concentration.

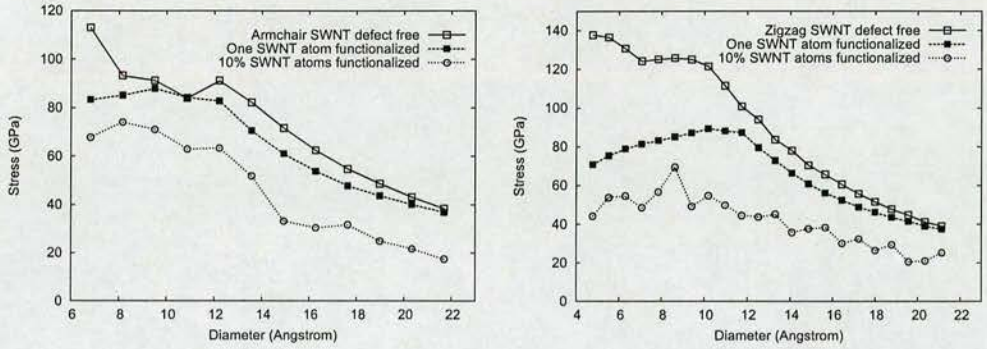

Figure 3.25: *Buckling stress of functionalized SWNT:(a) armchair SWNT, (b) zigzag SWNT*

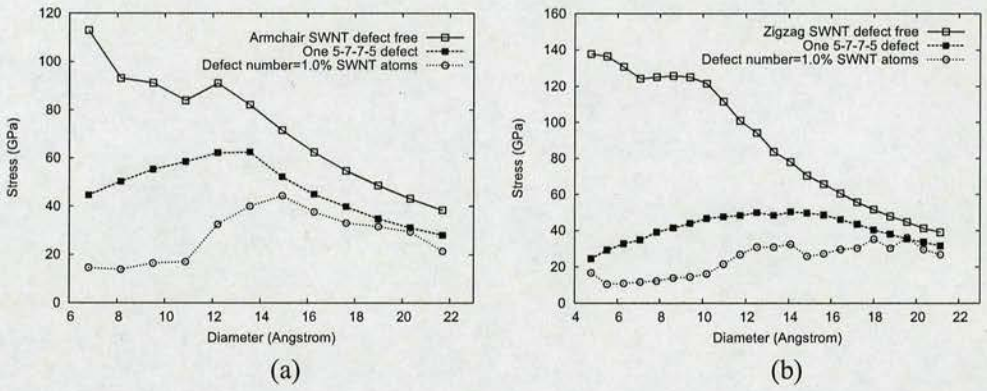

Figure 3.26: *Buckling stress of SWNT with 5-7-7-5 defect: (a) armchair SWNT, (b) zigzag SWNT*

3.7.3 Influence of number of defects

Multiple defects have a greater influence on Young's modulus of SWNT than a single defect because defects can act collectively. We use two SWNT with functionalization defects: armchair (10,10) and zigzag (16,0) SWNT. Both SWNT have around 3200 atoms. We chemically attach some methyl groups to the SWNT, and we make 9 samples containing different numbers of defects. The SWNT atoms percentage attached by such side groups are from 1.0%,2.0%,...,9.0%, and that means the number of defects varies from 32, 64, ..., 288.

Figure 3.28 shows results of Young's modulus and buckling strength of these SWNT. The Young's modulus of armchair (10,10) SWNT decreases from 0.82 to 0.74, and that of zigzag (16,0) SWNT decreases from 0.91 to 0.82. Both armchair (10,10) and zigzag (16,0) SWNT will become weaker in terms of Young's modulus if they have more defects.

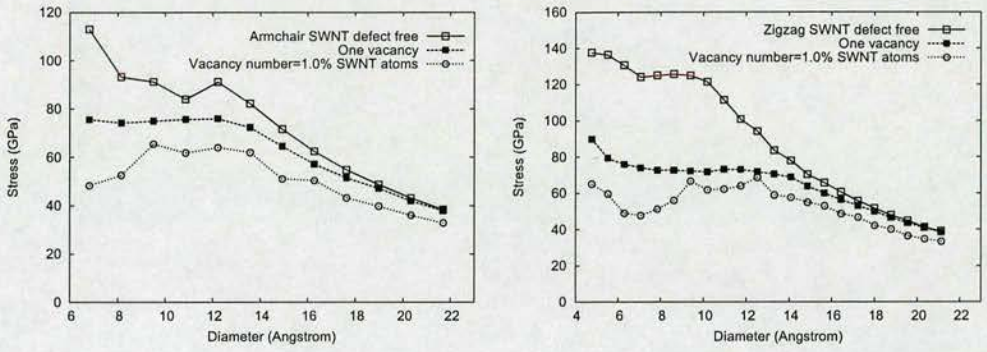

Figure 3.27: *Buckling stress of SWNT with vacancy: (a) armchar SWNT, (b) zigzag SWNT*

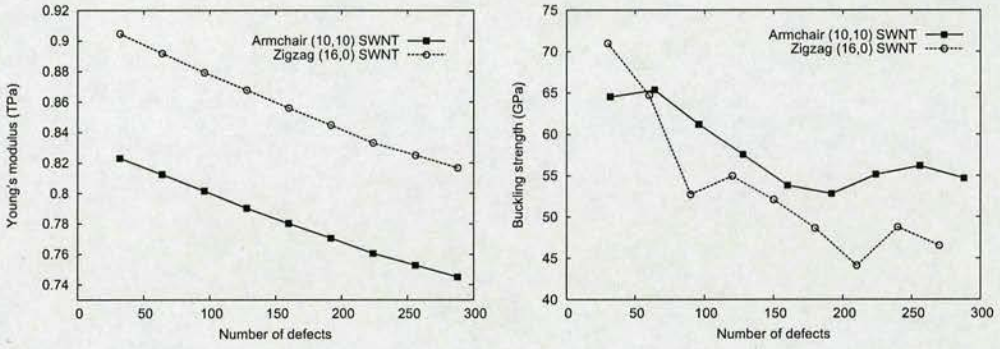

Figure 3.28: *Influence of number of defects (functionalisation defects): (a) Young's modulus, (b) buckling strength*

3.8 Summary

In this chapter, we compute the Young's modulus of SWNT under axial tensile loading and buckling strength under axial compressive loading. The computational results indicate that the longitudinal Young's modulus decreases with increasing nanotube diameter. We also investigate the influence of defects on the Young's modulus and buckling strength of SWNT. Three kinds of defects are studied: defects caused by chemical functionalization, topological defects (5-7-7-5 defects), and structural defects (vacancies). The results show that the Young's modulus of SWNT is slightly influenced by these defects, while the buckling stress is greatly decreased. For SWNT with small diameter (<14 Å), the buckling strength is especially sensitive to defects, and the buckling strength of all the SWNT deteriorates with increasing defect concentration.

Chapter 4
Size effect in tensile fracture of SWNT with defects

4.1 Introduction

Simulation of carbon nanotube fracture is aimed at understanding the influence of defects on fracture properties and effects of size-dependence of strength. Fracture involves phenomena occurring at a range of length scales. The defects we study are atomic defects, thus we need to understand the fracture at atomic scale. Basically, at the atomistic level, fracture happens in form of breaking of individual atomic bonds. Continuum analysis thus gives an incomplete picture, and experimental studies usually cannot reach the atomistic scale. Therefore, simulation studies are essential for investigating failure of defective carbon nanotubes.

4.2 Models

The carbon nanotubes used in our simulations are zigzag (8,0) SWNT. The length of the carbon nanotubes is about 100 Å and the diameter is about 6.4 Å. The same kinds of defects are studied in tensile failure of SWNT as in our previous study of buckling failure of SWNT. Instead of MM3 force field, we use Brenner's potential as the force field in our molecular mechanics calculations.

Zigzag (8,0) SWNT with functionalization defects

Number of defects (%× number of SWNT atoms)	1.5	3.0	4.5	6.0	7.5

Zigzag (8,0) SWNT with topological defects

Number of defects (%× number of SWNT atoms)	0.5	1.0	1.5	2.0	2.5

Zigzag (8,0) SWNT with vacancies

Number of defects (%× number of SWNT atoms)	1.5	3.0	4.5	6.0	7.5

Table 4.1: *Types of samples used in simulations*

As shown in Table 4.1, for each kind of defects, we use five different defect concentration. Since one topological defect will change the structure of four adjacent hexagons, we use lower defect concentrations than for the other two kinds of defects. All defects are randomly distributed. Therefore, the structure of every carbon nanotube has a random factor, which mimics the real distribution of defects on carbon nanotubes. For each defect concentration, we use 45 SWNT samples.

4.3 Modified Brenner's potential

4.3.1 Potential energy and stress of SWNT with original Brenner's potential

As in Chapter 3, we first elongate a defect free zigzag (8,0) SWNT step by step until it fractures, and we calculate the potential for every step. From the change of the potential energy with the strain, we can derive the stress applied to the carbon nanotube as shown in Figures 4.1 and 4.2.

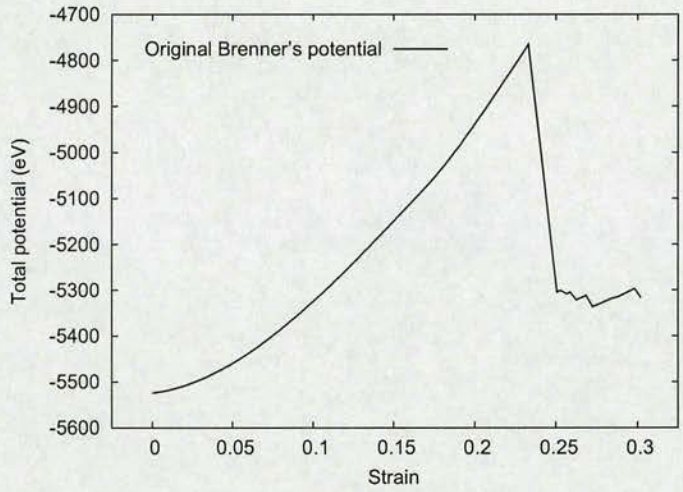

Figure 4.1: *Potential energy of SWNT under tensile load ((8,0) zigzag SWNT)*

As we can see, with the original Brenner's potential, the stress of carbon nanotubes under tensile load will have a unreasonable sharp increase before they fail (around strain equal to 0.17). To find the cause of this phenomenon, we monitor the change of bond length and angle of the carbon nanotube during elongation. For SWNT without defect, the initial elongation before fracture can be regarded as homogeneous deformation, therefore we can measure the bond length and angle as shown in Figure 4.3 to characterise the deformation of the carbon nanotube.

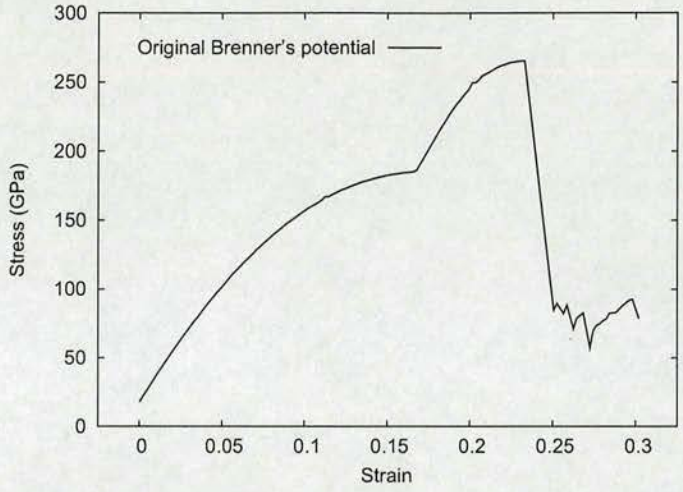

Figure 4.2: *Stress of SWNT under tensile load (zigzag (8,0) SWNT)*

4.3.2 Bond length and angle of SWNT with original Brenner's potential

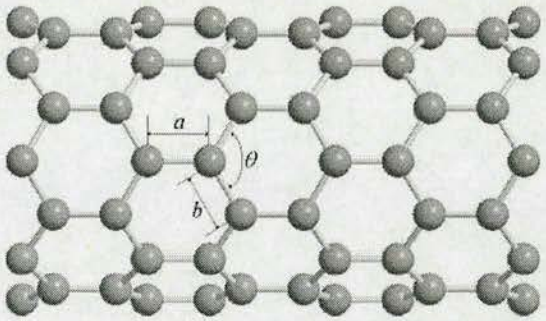

Figure 4.3: *Bond length and angle of SWNT*

The result is shown in Figure 4.4. In the beginning of the elongation, the length of bond a increases fast, while that of bond b increases only a little. When the length of bond a reaches the cut-off 1.7 Å, it increases very slowly since its increase will cause a high potential energy penalty, while the length of bond b instead increases faster than before. At strain equal to about 0.25, one or more bonds are broken, and then the length of bond a stops increasing, as fracture begins. It can be clearly seen that the sharp increase mentioned before is caused by the cut-off function of Brenner's potential.

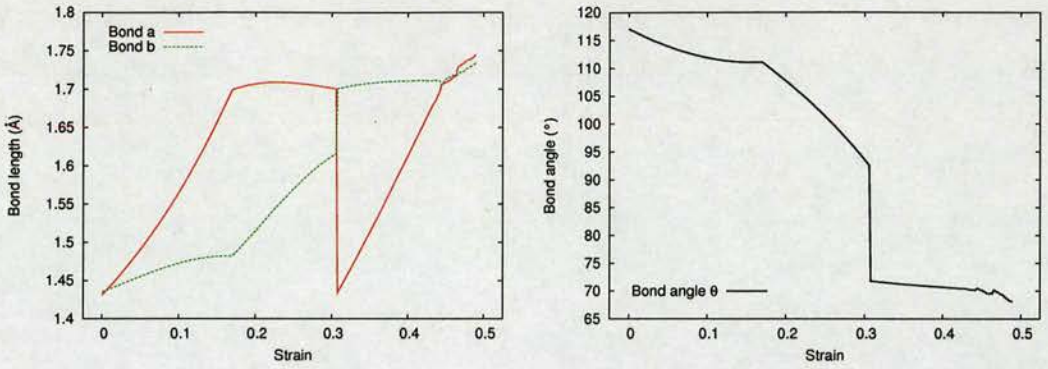

Figure 4.4: *Bond length and bond angle under tensile load with original Brenner's potential*

4.3.3 Potential energy and stress of SWNT with modified Brenner's potential

There are two ways to avoid this problem. The first is to use a different kind of potential to describe the bond energy of carbon nanotube such as Morse type potential. The other way is to modify Brenner's potential. As we found out that the abrupt increase of stress before failure is caused by the cut-off function of the potential, in our computation, we don't use cut-off function, instead, we extend the cut-off distance of Brenner's potential from 1.7 Å to 2.0 Å. The potential and stress of an carbon nanotube with the modified Brenner's potential are shown in Figure 4.5 and 4.6.

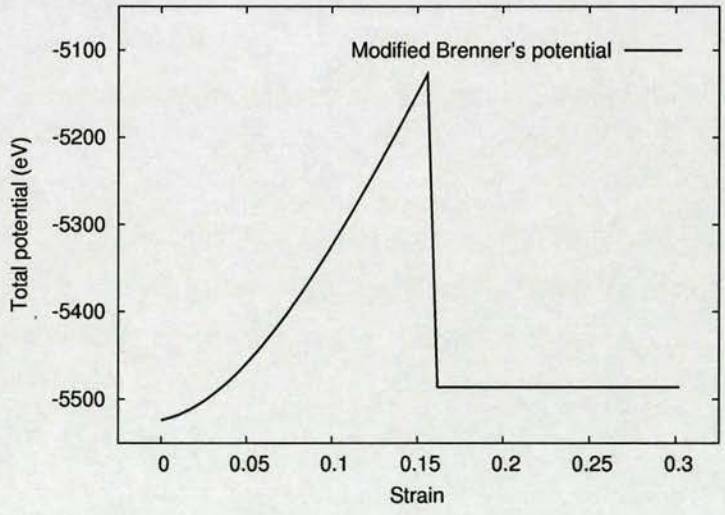

Figure 4.5: *Potential energy of SWNT under tensile load with modified Brenner's potential*

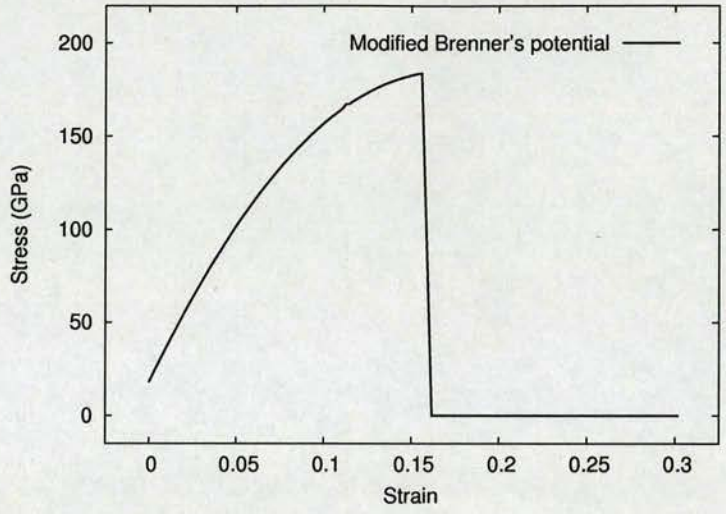

Figure 4.6: *Stress of SWNT under tensile load with modified Brenner's potential*

4.3.4 The influence of cut-off on potential energy and stress of SWNT

We can see that the potential and stress calculated with the modified Brenner's potential are the same as that with original Brenner's potential in the initial stage (strain < 0.16). Actually, if the cut-off distance is larger than 2.0 Å, and smaller than 2.5 Å, it does not change the final result of the potential and stress from the simulation. The results for different cut-off distances are show in Figure 4.7 and 4.8.

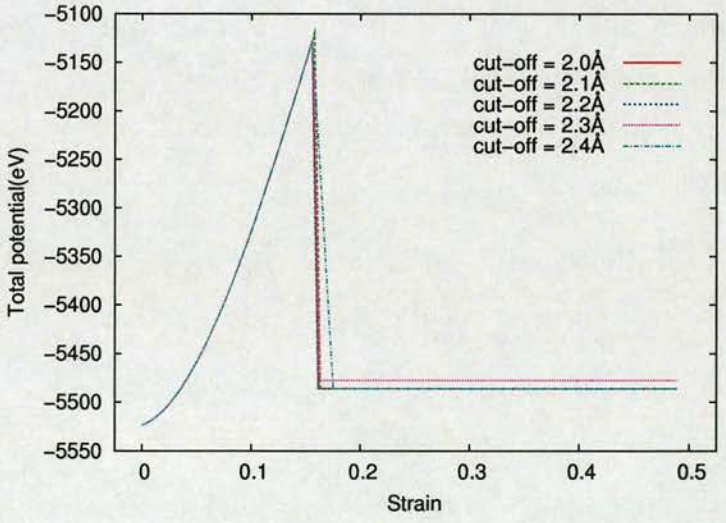

Figure 4.7: *Potential of SWNT under elongation with different cut-off distance*

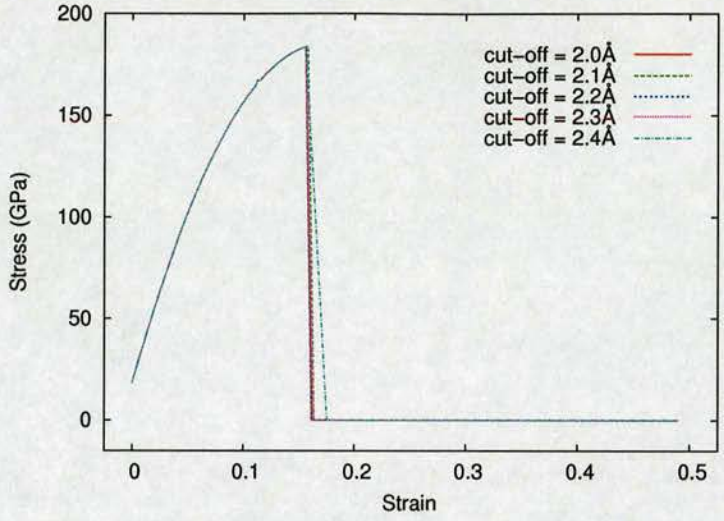

Figure 4.8: *Stress of SWNT under elongation with different cut-off distance*

4.3.5 Bond length and angle of SWNT with modified Brenner's potential

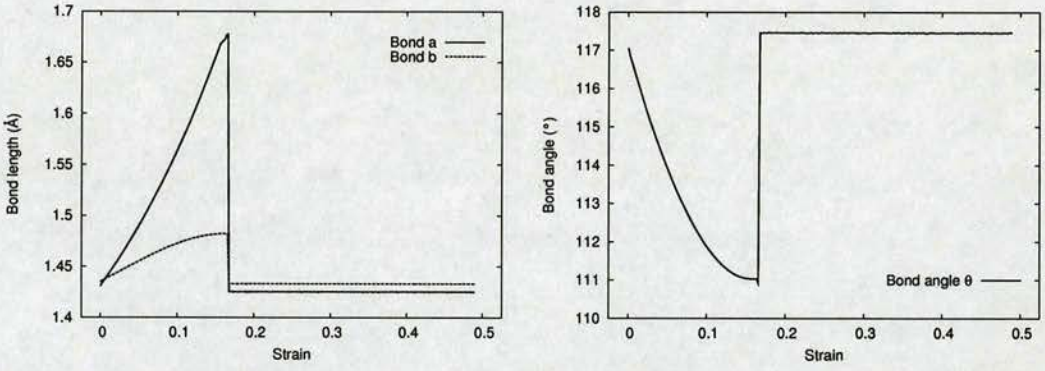

Figure 4.9: *Bond length and bond angle under tensile load with modified Brenner's potential*

Figures 4.2 and 4.6 show the stress of a carbon nanotube under tensile load both with original Brenner's potential and our modified Brenner's potential. It is clear that with the modified Brenner's potential the stress has no sharp increase before carbon nanotubes fail. More details about the changes of bond length and angle of carbon nanotubes under tensile load are illustrated in Figure 4.9. It is clear that there is irreversible bond destruction when SWNT fractures, and the remaining bonds will restore to their equilibrium structure. The structure of SWNT won't change much since the SWNT is broken into two parts and there is no more stress applied to it.

4.4 Tensile failure of SWNT with/without defect(s)

4.4.1 Elongation of SWNT

To simulate the elongation of carbon nanotubes, we move the end atoms in the axial direction away from the center of the carbon nanotube until it fails, calculate the potential energy after every step, and then derive the stress from the potential change. An illustration of the elongation of a defected carbon nanotube is given in Figure 4.10.

Figure 4.10: *Defected SWNT under tensile load*

4.4.2 Fracture strength of SWNT with defects

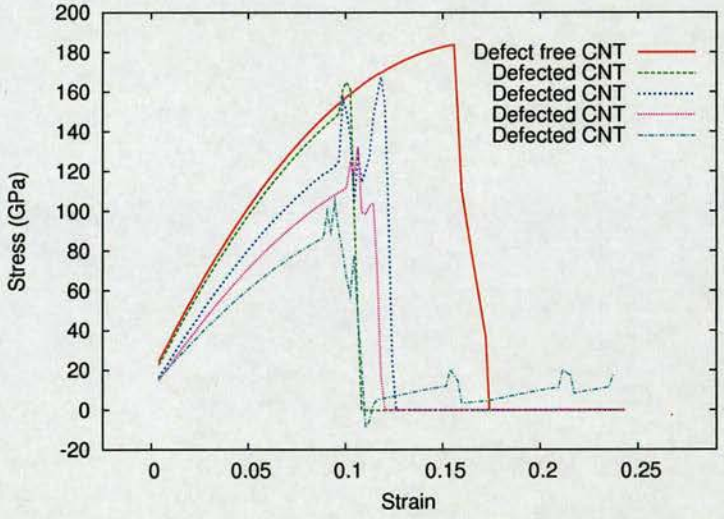

Figure 4.11: *Tensile failure of SWNT with/without defect(s) (Zigzag (8,0)) defect concentration* $\approx 7.5\%$

Since every defected carbon nanotube has a random distribution of defects, from our simulation, we find that the carbon nanotubes have different fracture strength for different samples as shown in Figure 4.11. Since the fracture strength of the defected carbon nanotubes has a wide distribution, the strength of defected carbon nanotubes can be described by a distribution with an average strength in terms of fracture statistics.

4.4.3 Fracture strength distribution of simulated SWNT

We can sort the fracture strength σ by magnitude from low to high. The probability distribution of fracture strength can be estimated as

$$P_s(\sigma^i) = (i - 0.5)/N, \tag{4.1}$$

where i is the ranking of the strength and N the number of samples. Simulation results are shown in Tables 4.2, 4.3 and 4.4. According to Equation 4.1, we can also obtain the probability distributions of fracture stresses of defected SWNT as shown in Figure 4.12, 4.13 and 4.14.

Fracture probability	0.011	0.033	0.056	...	0.944	0.967	0.989
Strength (GPa) 1.5% defects	110	122	125	...	169	170	174
Strength (GPa) 3.0% defects	97.5	108	109	...	164	165	167
Strength (GPa) 4.5% defects	91.5	94.9	101	...	154	154	155
Strength (GPa) 6.0% defects	89.8	90.6	94.4	...	151	151	153
Strength (GPa) 7.5% defects	67.0	85.0	87.2	...	142	148	148

Table 4.2: *Fracture probability of SWNT with functionalization defects*

Fracture probability	0.011	0.033	0.056	...	0.944	0.967	0.989
Strength (GPa) 0.5% defects	61.8	70.9	81.4	...	130	132	134
Strength (GPa) 1.0% defects	46.7	47.0	51.2	...	100	102	104
Strength (GPa) 1.5% defects	21.7	31.8	38.3	...	80.8	91.9	95.9
Strength (GPa) 2.0% defects	26.9	28.2	34.1	...	67.2	75.7	76.5
Strength (GPa) 2.5% defects	9.95	22.0	25.0	...	66.7	69.0	69.0

Table 4.3: *Fracture probability of SWNT with topological defects*

Fracture probability	0.011	0.033	0.056	...	0.944	0.967	0.989
Strength (GPa) 1.5% defects	110	122	125	...	169	170	174
Strength (GPa) 3.0% defects	97.5	108	109	...	164	165	167
Strength (GPa) 4.5% defects	91.5	94.9	101	...	154	154	155
Strength (GPa) 6.0% defects	89.8	90.6	94.4	...	151	151	153
Strength (GPa) 7.5% defects	67.0	85.0	87.2	...	142	148	148

Table 4.4: *Fracture probability of SWNT with vacancies*

From Table 4.2, 4.3 and 4.4, we see that generally all the three kinds of defect have great influence on SWNT fracture strength. A zigzag (8,0) SWNT without any defect has a fracture

strength of 190 GPa. After introducing each kind of defects, SWNT fracture strength has a broad distribution. If some defects on a SWNT are very close to each other, they tend to form a big defect. Therefore the SWNT will fracture very early, and have a low fracture strength. SWNT with a big defect will have lower fracture strength than those with a single or small defect. If we increase the defect concentration, the probability of forming a big defect will increase accordingly. As a result, the fracture strength will decrease, and the fracture strength distribution will shift to low strengths.

4.5 Weibull distribution fitting of fracture strength of SWNT

4.5.1 Weibull strength distribution

The Weibull distribution with a flexible two-parameter analytic formula has been found to successfully describe fracture data of brittle materials [94]. The Weibull strength distribution can be represented as [95]

$$F(x) = 1 - \exp\left[-\left(\frac{x}{x_0}\right)^m\right], \tag{4.2}$$

where x_0 is a normalised material strength and m is the Weibull modulus. The Weibull modulus is a measure of the relative width of the strength distribution which decreases with increasing m, and is also called the shape factor. Typical values of m are 5 for blackboard chalk, 10 for engineering ceramics and 100 for steel. Steel is therefore an example of a material that has a tensile strength that can be defined within a reasonably narrow range, in contrast to chalk.

4.5.2 Determination of the parameters in Weibull strength distribution

The determination of the parameters x_0 and m is not always straightfoward. In order to find the unknown parameters in a distribution function, the usual way is the linear regression (least-squares) procedure. However, the best estimate of these parameters is by the maximum likelihood method, which shows the smallest coefficient of variation (the ratio of the standard deviation and mean of a random quantity). The likelihood of a given probability density function is defined as $L = \Pi_{i=1}^{N} f(x_i)$, and thus its log-likelihood function is $\log L = \sum_{i=1}^{N} \log(x_i)$, where N is the number of strength data.

For our two-parameter Weibull distribution, the equation for determining these parameters from

N measured strength values x_i is [95]

$$\frac{\sum_{i=1}^{N} x_i^m \ln x_i}{\sum_{i=1}^{N} x_i^m} = \frac{1}{m} + \frac{1}{N}\sum_{i=1}^{N} \ln x_i, \tag{4.3}$$

where m can be obtained by an iterative procedure, and then the normalised material strength x_0 is calculated from

$$x_0^m = \frac{1}{N}\sum_{i=1}^{N} x_i^m. \tag{4.4}$$

With m and x_0, we can use Equation 4.2 to describe the fracture strength distribution of defected carbon nanotubes.

4.5.3 Weibull distribution fitting of SWNT strength from simulations

Figure 4.12, 4.13 and 4.14 show the results of Weibull distribution fitting. Apart from some low defect concentration samples, SWNT fracture strength distributions generally agree well with Weibull distributions. It should be pointed out that the Weibull distribution is not a good distribution to describe all sets of the data. For SWNT with low defect concentration (functionalization defect 1.5% and topological defect 0.5%), the distribution of fracture strength is not easily seen, and it might be clearer if we use more samples for these defect concentrations.

Zigzag (8,0) SWNT with functionalization defects

Number of defects (%× number of SWNT atoms)	1.5	3.0	4.5	6.0	7.5
Normalised materials strength (GPa)	163	148	138	131	116
Weibull modulus	15.7	10.3	8.47	7.91	6.62

Zigzag (8,0) SWNT with topological defects

Number of defects (%× number of SWNT atoms)	0.5	1.0	1.5	2.0	2.5
Normalised materials strength (GPa)	170	153	153	145	137
Weibull modulus	12.5	14.3	13.0	7.70	6.92

Zigzag (8,0) SWNT with vacancies

Number of defects (%× number of SWNT atoms)	1.5	3.0	4.5	6.0	7.5
Normalised materials strength (GPa)	114	85.6	65.8	56.2	48.9
Weibull modulus	8.81	5.76	4.56	5.31	3.75

Table 4.5: *normalised materials strength and Weibull modulus of SWNT with defects*

From Table 4.5, we can see that the normalised material strength of SWNT decreases with

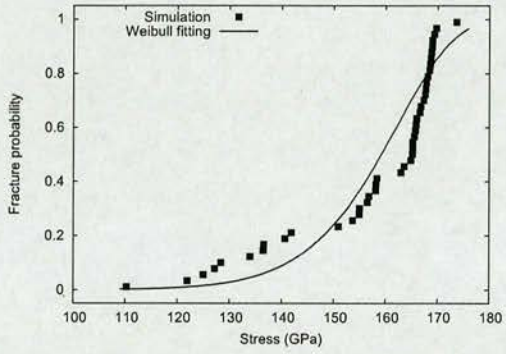

(a) mean number of defects $\approx$ 1.5%

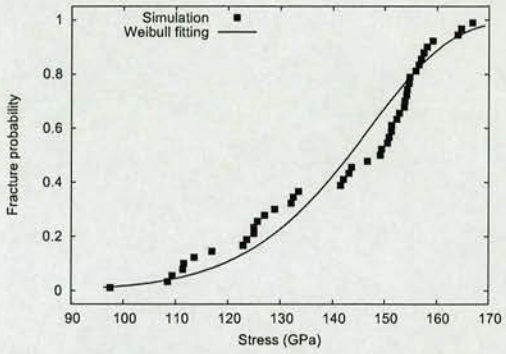

(b) mean number of defects $\approx$ 3.0%

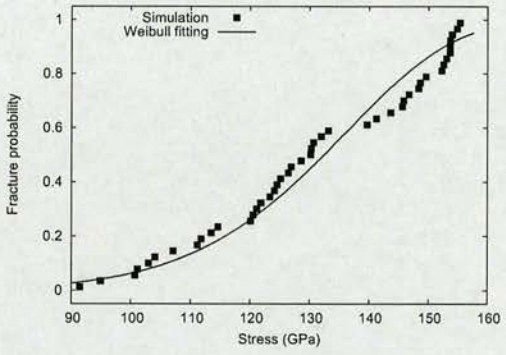

(c) mean number of defects $\approx$ 4.5%

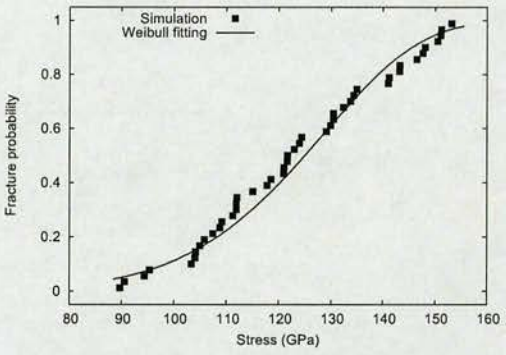

(d) mean number of defects $\approx$ 6.0%

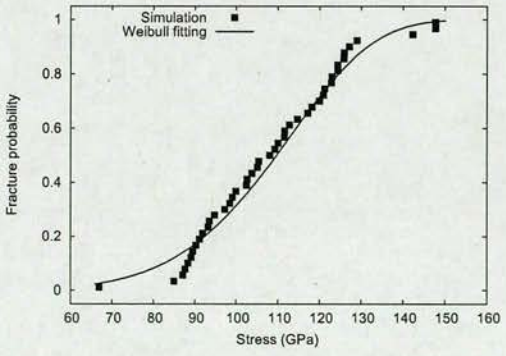

(e) mean number of defects $\approx$ 7.5%

Figure 4.12: *Weibull strength distribution of SWNT with functionalization defects*

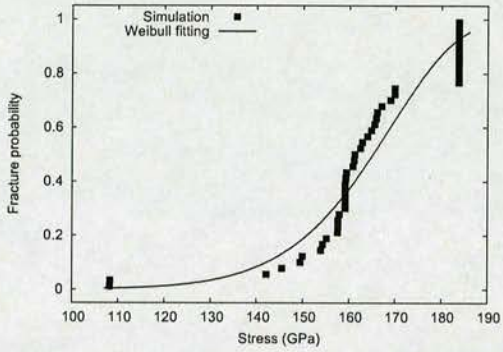

(a) mean number of defects $\approx$ 0.5%

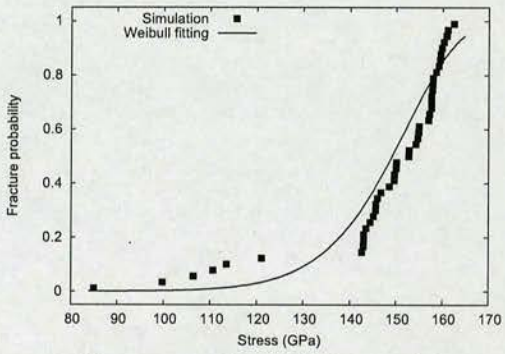

(b) mean number of defects $\approx$ 1.0%

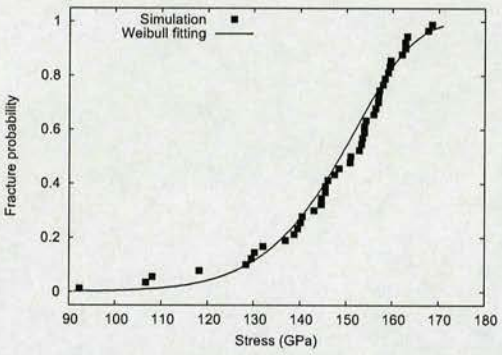

(c) mean number of defects $\approx$ 1.5%

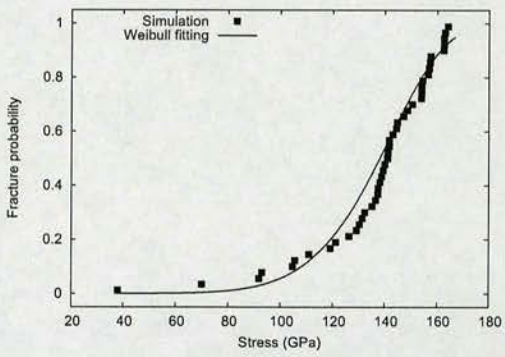

(d) mean number of defects $\approx$ 2.0%

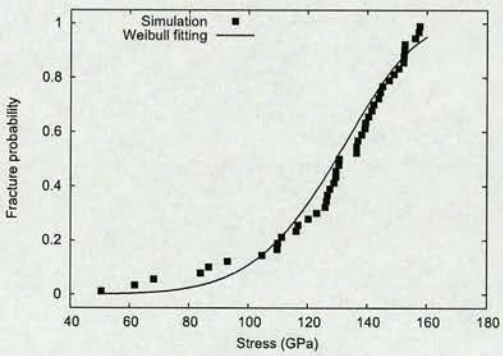

(e) mean number of defects $\approx$ 2.5%

Figure 4.13: *Weibull strength distribution of SWNT with topological defects*

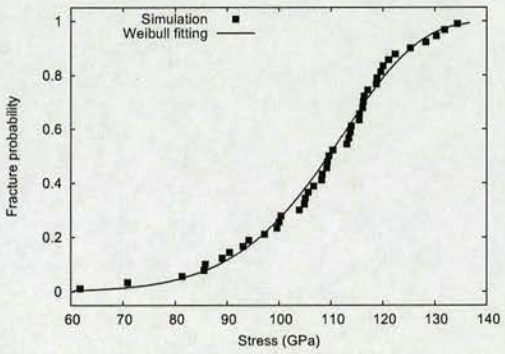

(a) mean number of defects $\approx$ 1.5%

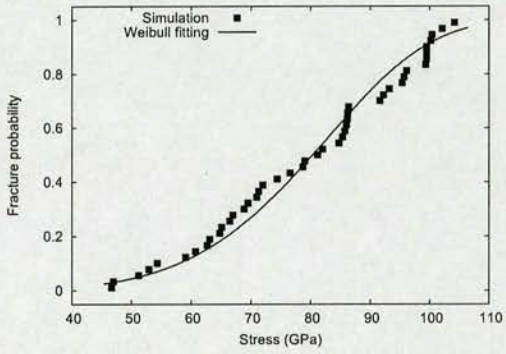

(b) mean number of defects $\approx$ 3.0%

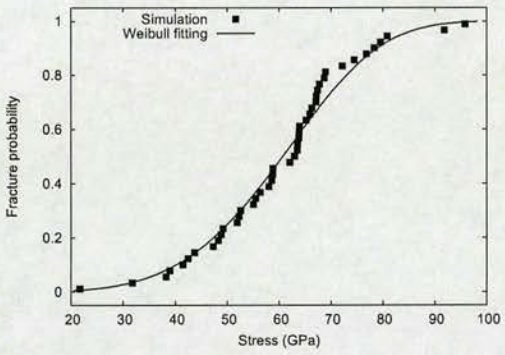

(c) mean number of defects $\approx$ 4.5%

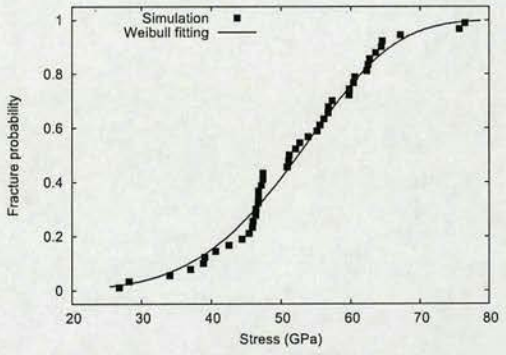

(d) mean number of defects $\approx$ 6.0%

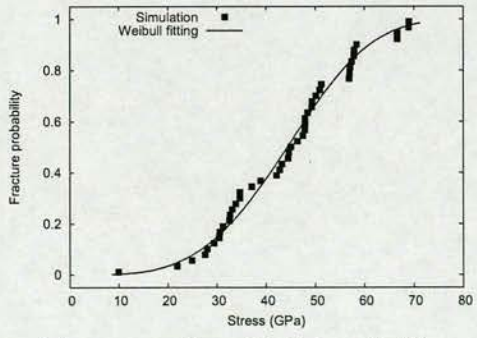

(e) mean number of defects $\approx$ 7.5%

Figure 4.14: *Weibull strength distribution of SWNT with vacancies*

increasing concentration of defects. For SWNT with functionalization defects, the defect concentration varies from 1.5% to 7.5%, and their normalised strength decreases from 162.9 to 115.9 GPa; For SWNT with topological defects, the defect concentration varies from 0.5% to 2.5%, and their normalised materials strength decreases from 170.1 to 136.6 GPa; For SWNT with vacancies, the defect concentration is from 1.5% to 7.5%, and their normalised strength decreases from 114.1 to 48.9 GPa.

The Weibull modulus also decreases with increasing defect concentration. This means the distribution of fracture strength becomes wider and wider with increasing defect concentration. For SWNT with functionalization defects, the defect concentration is from 1.5% to 7.5%, and their Weibull modulus decreases from 15.7 to 6.62. For SWNT with topological defects, the defect concentration is from 0.5% to 2.5%, and their Weibull modulus decreases from 12.5 to 6.92; For SWNT with vacancies, the defect concentration is from 1.5% to 7.5%, and their Weibull modulus decreases from 8.81 to 3.76. The Weibull modulus of SWNT with defects is between that of black chalks and that of ceramics.

4.6 Size effect of SWNT fracture strength

4.6.1 Weakest link model

In our simulations, carbon nanotubes are rather short, about 100 Å or so. In practical applications or experiments the carbon nanotubes used are about several μm or longer. An increase in sample size increases the probability of finding a larger defect and therefore implies a reduction in strength. In order to compare our simulation results with those from experiments, we have to take this size effect into account.

We can regard a short nanotube as a segment of a long carbon nanotube. Like a chain of many links, if the weakest link breaks, then the whole carbon nanotube will fail as shown in Figure 4.15. The strength S of a defected carbon nanotube is a random quantity and it thus has a distribution $L(x) = P(S < x)$. Now we divide a long carbon nanotube into n equal segments. Let the random strength of the ith segments be x_i. Since the whole carbon nanotube will break as soon as one part, the weakest one, breaks, the strength of the carbon nanotube equals the minimum W_n of x_i, $1 \leq i \leq n$, therefore $L(x) = P(W_n < x)$.

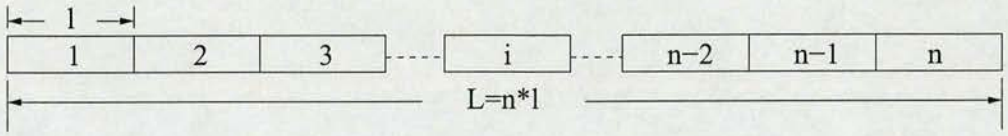

Figure 4.15: *Weakest-link model*

If the fracture strength distribution of each segment is $F(x) = P(x_i < x)$, we obtain

$$L(x) = P(W_n < x) = 1 - [1 - (1 - F(x))]^n . \tag{4.5}$$

The proof is as follows: Let $X_1, X_2, \ldots, X_n$ be independent and identically distributed random variables. With the notations

$$W_n = \min(X_1, X_2, \ldots, X_n); F_j(x) = P(X_j < x), \tag{4.6}$$

and

$$G_j(x) = 1 - F_j(x) = P(X_j \geq x) \tag{4.7}$$

$$G_n^*(x_1, x_2, \ldots, x_n) = P(X_1 \geq x_1, X_2 \geq x_2, \ldots, X_n \geq x_n). \tag{4.8}$$

We get

$$\begin{aligned} L(x) &= P(W_n < x) = 1 - P(W_n \geq x) = 1 - P(X_1 \geq x, X_2 \geq x, \ldots, X_n \geq x) \\ &= 1 - P(X_j \geq x)^n = 1 - [1 - F(x)]^n . \end{aligned} \tag{4.9}$$

4.6.2 Size effect in fracture strength of defected carbon nanotubes

From above, we know that the distribution of fracture strength of long carbon nanotube is

$$L(x) = 1 - [1 - F(x)]^n . \tag{4.10}$$

If F is a Weibull distribution, the strength distribution of a long carbon nanotube is also a Weibull distribution:

$$L(x) = 1 - [1 - F(x)]^n = 1 - \left[\exp\left(-\left(\frac{x}{x_0}\right)^m\right)\right]^n = 1 - \exp\left[-\left(\frac{x}{\frac{x_0}{\sqrt[m]{n}}}\right)^m\right]. \tag{4.11}$$

Therefore

$$L(x) = 1 - \exp\left[-\left(\frac{x}{x_{n0}}\right)^{m_n}\right], \tag{4.12}$$

where $m_n = m$, and $x_{n0} = \frac{x_0}{\sqrt[m]{n}}$.

As a result, if we know l_0 and x_0, we can obtain the normalised material strength of defected carbon nanotubes of different length from

$$x_{l0} \propto l^{-\frac{1}{m}} \text{ or } \quad \frac{x_{l0}}{x_0} = \left(\frac{l}{l_0}\right)^{-\frac{1}{m}}, \tag{4.13}$$

where l is the length of a carbon nanotube, and m the Weibull modulus. For example, if l_0 =10 nm and $l = 1\ \mu m$, $n = 100$ in Equation 4.12.

In our simulations, the original length of all SWNT is about 100 Å(0.01 μm), and from our simulations we can obtain their material modulus and normalised material strength. With Equation 4.13, we can obtain the normalised material strength of defected carbon nanotubes of different length. For example, we can use the results from SWNT with 6.0% functionalization defects, 2.0% topological defects and 1.5% vacancies. The normalised material strengths are 131, 145, 114 GPa, and the Weibull moduli are 7.91, 7.70, 8.81, accordingly. The results calculated with Equation 4.13 are shown in Figure 4.16.

Zigzag (8,0) SWNT with functionalization defects

SWNT length (μm)	0.01	0.05	0.20	1.0	2.5	5.0	10.0
Functionalized SWNT (GPa)	131	107	89.6	73.1	65.1	59.7	54.7
SWNT with topological defects (GPa)	145	117	98.2	79.7	70.7	64.6	59.1
SWNT with vacancies (GPa)	114	95.1	81.2	67.7	61.0	56.4	52.1

Table 4.6: *normalised strength of SWNT with defects:SWNT with functionalization defects contain 6.0% defects; SWNT with topological defects contain 2.0% defects; SWNT with vacancies contains 1.5% defects*

From Table 4.6, it is seen that for all the three kinds of defects, the SWNT fracture strengths decrease with increasing their length. For (8,0) zigzag SWNT with 6.0% functionalization defects, the normalised strength is 131 GPa if the length is 100 Å (0.01 μm), while 54.7 GPa if the length is 10 μm; For (8,0) zigzag SWNT with 2.0% topological defects, the normalised strength is 145 GPa if the length is 100 Å, while 59.1 GPa if the length is 10 μm; For (8,0) zigzag SWNT with 1.5% vacancies, the normalised strength is 114 GPa if the length is 100 Å,

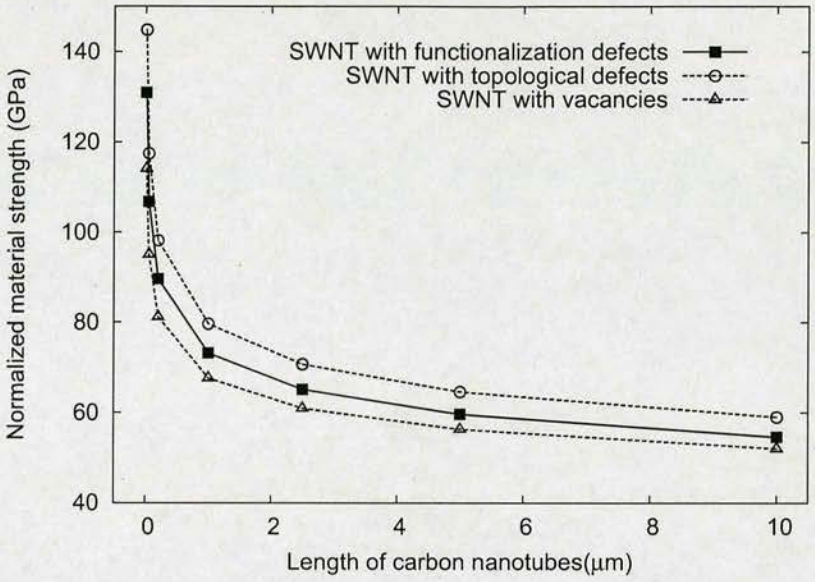

Figure 4.16: *normalised material strength of defected SWNT of different length: SWNT with functionalization defects contain 6.0% defects; SWNT with topological defects contain 2.0% defects; SWNT with vacancies contains 1.5% defects (The SWNT in experiment is about 10 μm long, and the fracture strength is from 13 ∼ 52 GPa)*

while 52.1 GPa if the length is 10 μm. Defects together with the size effect make long carbon nanotube weak, which reasonably explains the low SWNT fracture strength (13 $\sim$ 52 GPa) from experiments far below the theoretical prediction ($\sim$ 250 GPa) [33].

4.7 Summary

This chapter shows that the simulation of fracture of SWNT with and without defects. Size dependence of fracture strength of defected carbon nanotubes is studied with extreme order statistics, and a relationship between the length of SWNT and their fracture strength is established. This study reasonably explains differences between SWNT fracture strengths measured in experiments (13 $\sim$ 52 GPa) and those from theoretical calculations on defect free carbon nanotubes ($\sim$ 250 GPa). The results show that extreme order statistics with Weibull distribution function is a sound method to analyse the strength of defected carbon nanotubes. It can be developed into an important tool for helping to understand the influence of defects on fracture strength of carbon nanotubes.

Chapter 5
MD simulations of interactions between SWNT and polymers

5.1 Introduction

Polymer composites using carbon nanotubes as fiberlike reinforcers possess-at least in theory-great potential as ultrastrong lightweight materials and have therefore attracted much recent attention of theoretical scientists [96, 97]. The high strength and large aspect ratio of carbon nanotubes make them ideal candidates as ultrastrong reinforcers for composites. It has been reported that by using only 1 wt% MWNT reinforcement the elastic stiffness of polymer-matrix nanocomposites was improved by 40% over that of the bare polymer-matrix materials and strength values improved by nearly 25% [47]. By sandwiching carbon nanotubes between polymer layers, researchers have created a revolutionary material that is 6 times stronger than conventional carbon-fiber composites and exhibits hardness values comparable to some ultrahard ceramic materials used in engineering [98]. Recently, it has also been reported that carbon nanotubes composites using 60% carbon nanotubes exhibited a rupture strength of 1.8 GPa, which matches that of spider silk [99].

5.2 Interfacial interaction in polymer composites

From the research on microfiber-reinforced composites over the past few decades, it is well-established that the structure and properties of the fiber-matrix interface play a major role in determining mechanical performance and structural integrity of composite materials [100]. Several groups have reported investigations of the interfaces in carbon nanotube-reinforced polymer composites. For example, from experimental studies and molecular modelling of carbon nanotube-polystyrene and carbon nanotube-epoxy composites, it has been suggested that the interfacial shear stress of the carbon nanotube-polymer systems is at least an order of magnitude higher than that of conventional microfiber-reinforced composites [101]. In morphology analysis of fracture surfaces of carbon nanotube-epoxy composites, however, no broken carbon

nanotubes were observed. This indicates that the load transfer from polymer to carbon nanotube was not sufficient to fracture the carbon nanotubes. Instead, the failure of the composite appears to arise from pullout of the nanotubes and from mechanical fracture of the polymer matrix [82].

Good interfacial binding is a necessary condition for successful load transfer across the interface between carbon nanotubes and polymer matrix. An obvious strategy for improving interfacial binding is chemical functionalization by attaching polymeric side chains to the carbon nanotubes. In this manner, one may hope to improve the binding of nanotubes by interdigitation of the polymeric side chains into the polymer matrix. However, the extraordinary mechanical properties of carbon nanotubes depend on their specific chemical structure. Covalent functionalization introduces atomic defects and internal stresses into the nanotubes, which thereby deteriorates their mechanical properties as confirmed by our study in the previous chapters and work by other researchers [102, 103]. It is therefore desirable to explore the possibility of optimising noncovalent intermolecular interactions between carbon nanotubes and polymers in view of achieving strong interfacial binding in a composite [104–109]. Since carbon nanotubes exhibit an even charge distribution, there is hardly any electrostatic interaction between nanotubes and polymers, and therefore in the absence of defects on carbon nanotubes, the polymer-carbon nanotube interaction is solely due to van der Waals forces. The strength of the interfacial binding in this case depends on the geometrical conformation of the polymer with respect to the nanotube, and accordingly in the present study, we investigate the relationship between the conformation of different polymers and their adhesion to carbon nanotubes of different diameters.

5.3 Simulation method

5.3.1 Model

In the present study, we consider SWNT in "zigzag" configuration. The SWNT considered have a fixed length of 103.8 Å with diameters ranging from 3.9 to 53.6 Å. The simulated polymers were polystyrene (PS), poly(phenylacetylene)(PPA), poly(*p*-phenylenevinylene)(PPV), and poly(m-phenylenevinylene-*co*-2,5-dioctyloxy-p-phenylenevinylene)(PmPV). Since the number of atoms and monomers used is small (about 150 atoms per molecule which corresponds to 10 monomers for PS, PA, PPV, and 2 monomers for PmPV), our molecules are better described

as oligomers than polymers; however, we use the term "polymer" throughout the paper for simplicity, with the understanding that the results of our simulation describe the behaviour of a small part (block) of a "long" polymer. PS and PPA are molecules with side groups of aromatic rings. PS is rather flexible because its σ-bonds between repeating units allow easy rotation around the axis of the backbone, whereas PPA is much more rigid because of its completely conjugated backbone structure; PPV is a rigid linear molecule with a conjugated aromatic ring backbone structure, and PmPV is a substituted form of PPV with an added dihedral angle that makes the chain more flexible.

Conjugated polymers [110] have been reported to exhibit good binding with SWNT, and electron microscopy studies have demonstrated heavy coating of SWNT by several conjugated polymers including PmPV [107, 111–113]. This suggests the possibility of using SWNT for mechanical reinforcement of a PmPV matrix [114]. Polymers with increased affinity for physisorption on carbon nanotubes are good candidates in promoting enhanced interfacial binding between a polymer matrix and carbon nanotubes if they are used as parts (blocks) within a diblock copolymer that contains another block with affinity to the polymer matrix. Such an "amphiphilic" copolymer can be used in small quantities to increase both the dispersion in appropriate organic solvents during processing and the interfacial binding between the carbon nanotubes and the polymer matrix in the final product (carbon nanotube-polymer composite). In this way, one can avoid chemical functionalization that (a) is a nontrivial processing step and (b) induces defects in the carbon nanotube structure, compromising their superb mechanical properties. The potential of this approach has been confirmed by recent experiments [115]. The adsorption of the amphiphilic copolymer on the carbon nanotube is to occur in a selective solvent (bad solvent for the blocks which are to adhere on the carbon nanotube). Our simulation is related to the behaviour of these blocks when they are close to the carbon nanotube in an "ideal" bad solvent, as will be discussed in more detail below.

The molecular models have been built with the commercial Chem3D software, and the original atom coordinates of carbon nanotubes were generated from DL_POLY Java [116]. The structures are shown in Figure 5.1.

5.3.2 Parameters and thermostat algorithm for MD simulations

In the simulations, the velocity form of Brook's "Better Beeman" method is used to integrate the equations of motion with a basic time step of 1.0 fs. In order to speed up our simulation

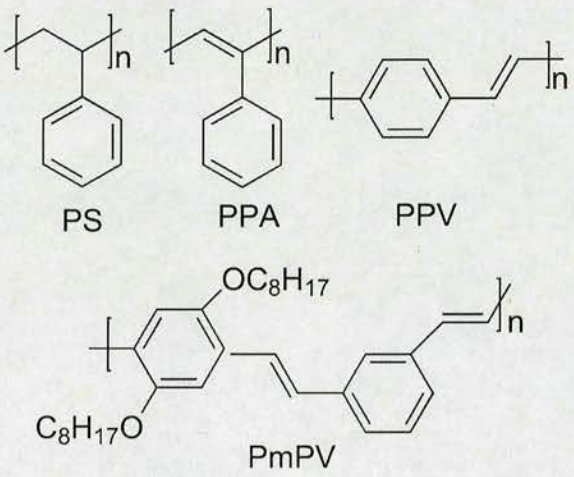

Figure 5.1: *Chemical structure of the investigated polymers*

and facilitate our later morphology analysis of polymers, we fix the position of SWNT atoms in our simulation, and only polymers are allowed to move freely. Carbon nanotubes have rigid structure, and they can keep intact under the conditions of our study.

To investigate the influence of fixing SWNT atoms and to assess the behaviour of different thermostat algorithms, we also simulate the interaction between a graphene sheet and polymers since the graphene sheet has the same local structure as the SWNT (we can regard a graphene sheet as a SWNT with infinite diameter). We set the temperature in these simulations at 500 K. Fixing SWNT atoms has little influence on the interaction between SWNT and polymer, as will be discussed below.

We use NVT simulations (constant number of atoms, constant volume and constant temperature). There are several thermostat algorithms used in MD simulations including Andersen algorithm, Berendsen algorithm and Nose-Hoover algorithm. MD simulations were carried out using the TINKER package [117] with MM3 force field [55]. More details about these algorithms are included in Appendix "Thermostat algorithms of molecular dynamics".

After finishing MD simulation, we obtain a trajectory which contains the time evolution of molecular structure. In this simulation, the trajectory records the molecular structure of the graphene and polystyrene every 1 ps, and totally 1500 ps long. We retrieve the molecular structures and calculate the total potential energy and intermolecular energy between the graphene and polystyrene. When we calculate the intermolecular energy between the graphene and polystyrene, we set the atoms of graphene and those of the polystyrene as two separate

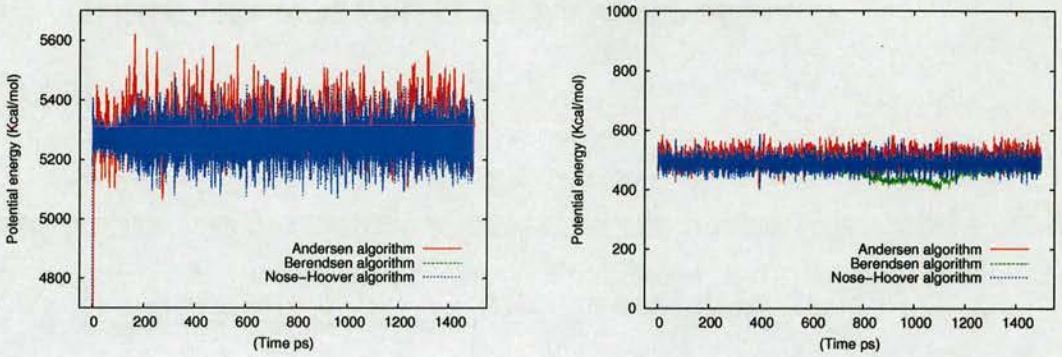

Figure 5.2: *Potential energy of graphene and polystyrene with different thermostat algorithms: (a) graphene unstrained, (b) graphene fixed*

groups, and only calculate the interaction between the two groups. These energy calculation can be implemented via **analyse** program with keyword *group* and *group-inter* in key file.

Figure 5.2 shows the potential energy of graphene and polystyrene with and without graphene atoms fixed. The total potential energy with graphene fixed is larger than that with graphene unstrained. That is because that when we keep graphene atoms fixed, the interaction within the graphene atoms are excluded in our computation, therefore the potential energy only includes the potential energy of the polystyrene molecule and the interaction between the graphene and the polystyrene.

The potential energy of the whole system itself has nothing to do the interaction between graphene and polymer. We check the influence of fixing atoms on the potential energy, and the differences with different thermostats to validate the stability of the thermostat with the graphene atoms fixed. Figure 5.2(a) shows that the total potential energy becomes stable quickly with reasonable variation for all the three thermostats when the graphene atoms are unconstrained, while if the graphene atoms are fixed, although Andersen and Nose-Hoover algorithms have stable potential energy, the potential energy calculated with Berensen algorithm is unstable.

For the intermolecular energy between the graphene and the polystyrene, we obtain the similar conclusions. Therefore, the Berendsen algorithm is not suitable if we keep SWNT fixed to study their interaction with polymers. The intermolecular energy between the graphene and the polystyrene is shown in Figure 5.3.

We calculate the averages of potential energy, intermolecular energy and temperature. Ta-

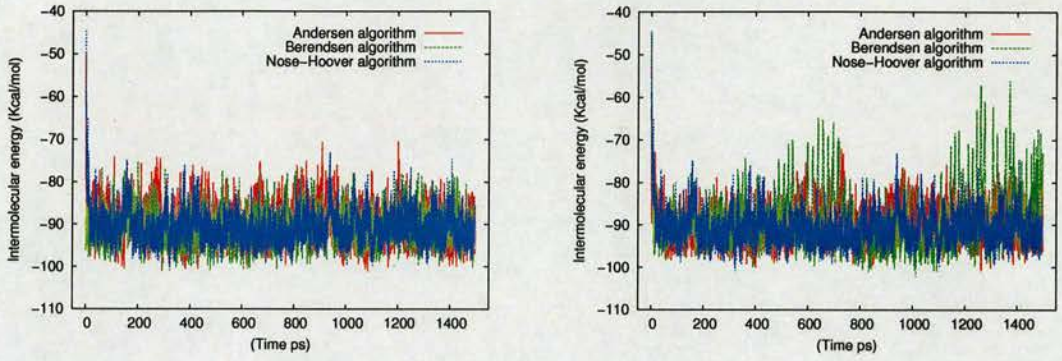

Figure 5.3: *Intermolecular interaction between graphene and polystyrene with different thermostat algorithms: (a) graphene unstrained, (b) graphene fixed*

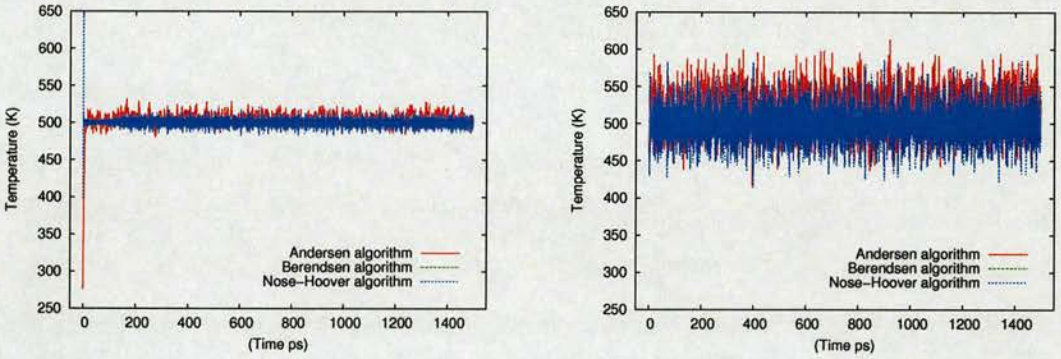

Figure 5.4: *Temperature of graphene and polystyrene with different thermostat algorithms: (a) graphene unstrained, (b) graphene fixed*

ble 5.1 shows the potential energy, intermolecular energy and temperature of simulations with different thermostat algorithms. Berendsen and Nose-Hoover algorithms have better control of temperature than Andersen algorithm. If we compare the intermolecular energy from simulation with Berendsen algorithm and that with Nose-Hoover algorithm, we can see that with fixed graphene, the energy only changes by 0.3% with Nose-Hoover, while 3% with Berendsen algorithm. The computation time of graphene fixed system is only 40% of that without any constraint. In simulation of interaction between SWNT and polymers, the efficiency improvement by fixing SWNT is dependent on the atoms number of SWNT, and normally around 30%.

If we take all these factors into account, we can see that Nose-Hoover has good temperature control and is the best thermostat algorithm for our study. Unless explicitly specified otherwise, all MD simulations were implemented at 400 K. A cutoff distance of 10 Å was used for nonbonded interaction.

Simulations of unstrained graphene and polystyrene

Method	Potential energy (kcal/mol)	Intermolecular energy (kcal/mol)	Temperature (K)
Andersen algorithm	2631	-89.75	505.6
Berendsen algorithm	2600	-90.67	500.0
Nose-Hoover algorithm	2600	-89.65	500.0

Simulations of fixed graphene and polystyrene

Method	Potential energy (kcal/mol)	Intermolecular energy (kcal/mol)	Temperature (K)
Andersen algorithm	263.1	-89.93	518.3
Berendsen algorithm	241.9	-86.90	500.0
Nose-Hoover algorithm	253.4	-89.93	500.0

Table 5.1: *Comparison of simulations with different thermostat algorithms*

5.3.3 Boundary conditions

We use a constant NVT simulation in vacuum, which implies that the simulated volume is actually infinite. The polymer chain is initially placed alongside the carbon nanotube such that part of the polymer is within the cutoff distance of the van der Waals interactions with carbon nanotube atoms, and subsequently the polymer adsorbs onto the nanotube due to the attractive force between the polymer and the carbon nanotube. For each carbon nanotube-polymer pair, different initial conditions are tested to ensure that the calculated adsorption energy does not depend on the initial conformation of the polymer. From the characteristics of the Nose-Hoover thermostat, we know that the MD simulation with this method produces a canonical distribution. However, it has to be noted that our simulation does not explore all the states of the ensemble because of the short simulation time (several nanoseconds). If the simulation time were long enough, then the polymer would move away eventually and very likely never interact with the carbon nanotube again. This is a direct consequence of the fact that we use infinite volume (no boundary conditions). However, this "escape" event is extremely rare, and it does not affect the results within our simulation time. We simulate the effect of an ideal bad solvent by doing the simulation in a vacuum, and the thermostat in our simulation can be thought of as mimicking the action of the bad solvent.

5.4 Interaction between SWNT and polymers

5.4.1 Simulation of interaction between SWNT and polymers

MD simulations are first carried out on a SWNT of 11.8 Å diameter and interacting with individual molecules of PS, PPA, PmPV, and PPV, respectively. The models are equilibrated for 2 ns to stabilise the interactions. After this, the total interaction energy between the SWNT and the polymers in equilibrium is calculated for 3 ns. In Figure 5.5, we present the intermolecular interaction energy for the four models as a function of time. The simulated polymers have comparable numbers of atoms (PS 162 atoms, PPA 142 atoms, PmPV 158 atoms, and PPV 142 atoms); hence the magnitude of the interaction energy gives a direct measure of the strength of their binding to the SWNT. The figure shows that although all of the polymers have an obvious attractive interaction with the nanotube, the specific monomer structure plays a very important role in determining adhesion to the SWNT. It is seen that PPV exhibits the strongest interaction with the SWNT, then PmPV, PPA, and PS. The polymers with aromatic rings in the backbone(PmPV and PPV) have stronger interactions with the SWNT than those with side group aromatic rings (PS and PPA).

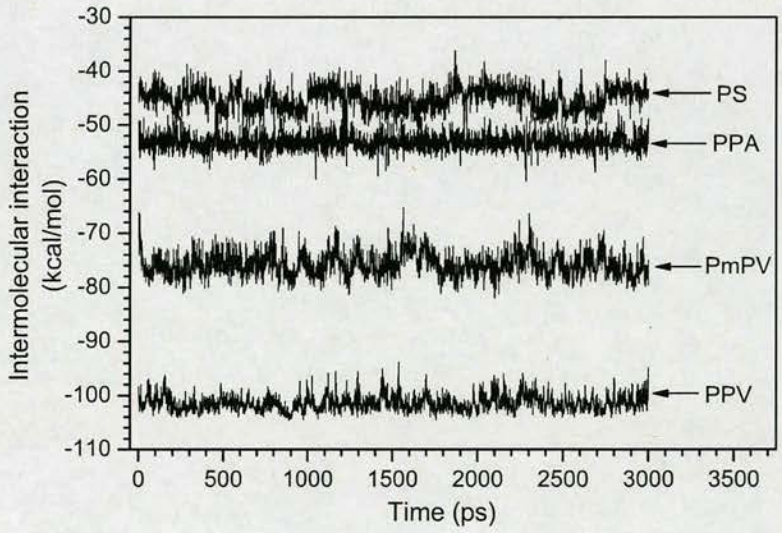

Figure 5.5: *Intermolecular interaction between SWNT and polymers*

5.4.2 Temperature dependence of the intermolecular interactions

To assess the temperature dependence of the intermolecular interaction between the polymers and the SWNT, MD simulations are carried out at different temperatures. The temperature is varied between 300 and 500 K in steps of 25K. Figure 5.6 shows the temperature dependence of the intermolecular interaction.

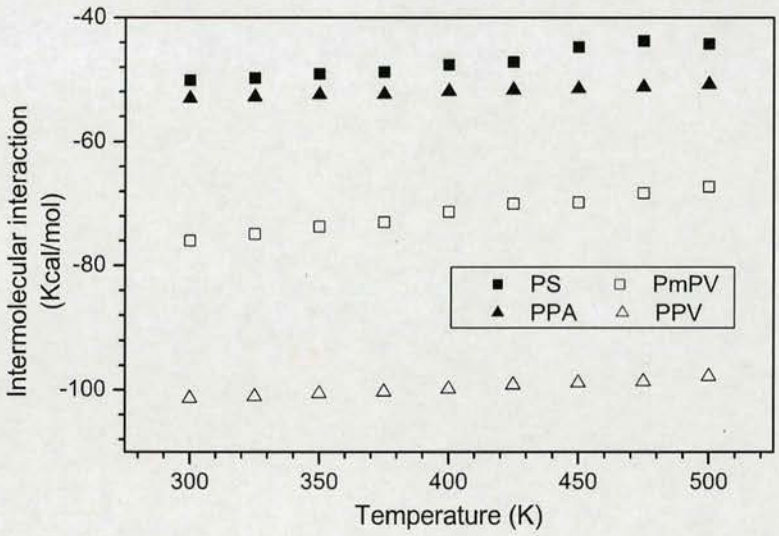

Figure 5.6: *Intermolecular interaction as a function of temperature*

In general, the temperature has limited influence on the interaction between SWNT and polymers. It is seen that for all considered polymers the attractive interaction with the carbon nanotube decreases only weakly with increasing temperature. With temperature increasing from 300 to 500K, the change of interaction energy is within 10%.

5.4.3 Influence of SWNT diameter on the intermolecular interactions

To determine the influence of the carbon nanotube diameter on polymer adhesion, MD simulations are carried out on SWNT with PS, PPA, PmPV, and PPV, respectively. The SWNT diameter in these simulations is varied from 3.9 to 53.5 Å. When the SWNT diameter is increased, the attractive interaction between the simulated polymers and the SWNT monotonically increases toward an asymptotic value given by the interaction of the polymer with a flat graphene surface (Figure 5.7). This indicates that the curvature of the graphene sheets that constitute the carbon

nanotubes diminishes polymer adhesion. The influence of SWNT diameter on interaction energy is evident for small SWNT, while for SWNT of diameter larger than 15 Å, the diameter dependency is very limited. For SWNT of large diameter, their surface is much closer to that of graphene, and their intermolecular interaction with SWNT is close to that with graphene. However, the effect of the polymer flexibility is important since the intermolecular interaction changes by ca. 100% for the flexible PS to ca. 50% for the stiff PPV.

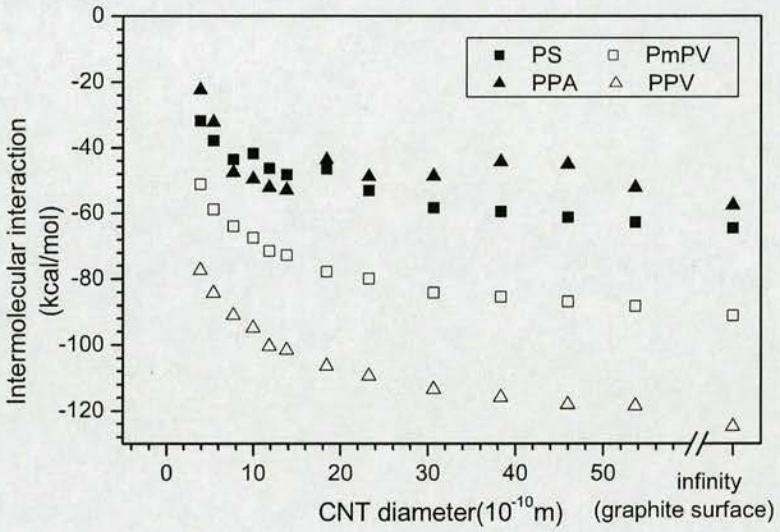

Figure 5.7: *Intermolecular interaction as a function of diameter*

5.5 Morphology of polymers on SWNT surface

When a polymer interacts with a graphene molecule or carbon nanotube, the alignment of parts of the polymer chain along the graphene or carbon nanotube surface may lead to conformational changes. For illustration, we simulate the interaction between graphene and polymers (PS and PmPV).

Figure 5.8 (a) and 5.9 (a) show the configurations of PS and PmPV alone in vacuum, while Figure 5.8 (b) and 5.9 (b) show the configurations of PS and PmPV when they interact with graphene. For PS, its configuration does not change very much, while for PmPV, by contrast, its configuration alters quite a lot when it interacts with graphene. The configuration of PmPV aligns very well on the graphene, and the aromatic structure on its backbone is parallel to the

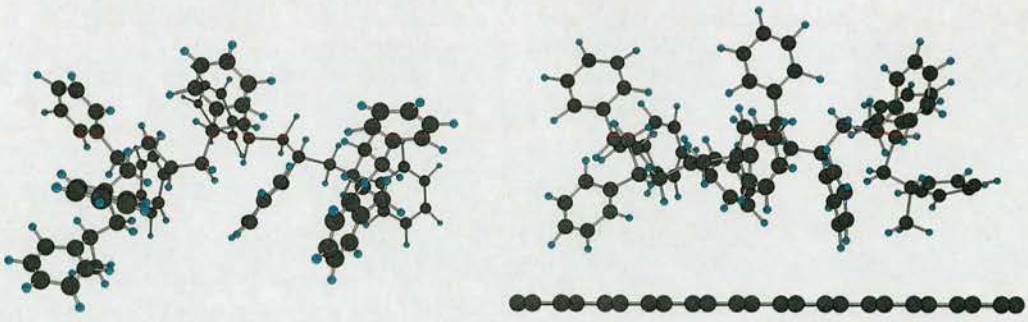

(a) (b)

Figure 5.8: *PS configurations: (a) before interacting with graphene, (b) interacting with graphene*

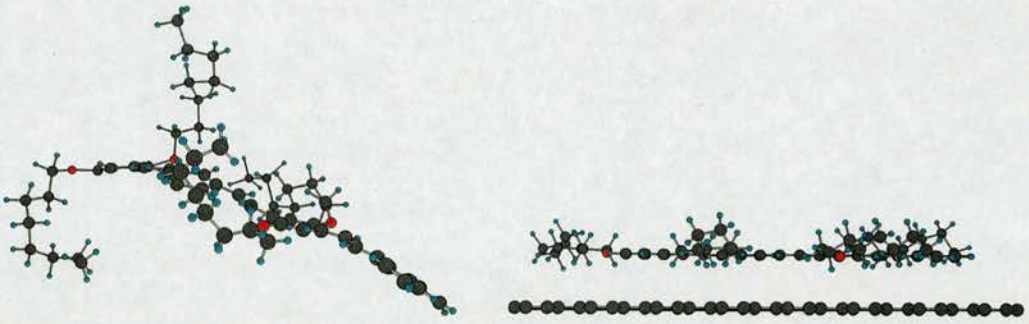

(a) (b)

Figure 5.9: *PmPV configurations: (a) before interacting with graphene, (b) interacting with graphene*

graphene surface. The side-chain aromatic structure of PS can not align well on the graphene, which limits its interaction.

In the following study, we investigate the morphological aspects of polymer-graphene and polymer-SWNT interactions both on the local level, where we focus on the arrangement of the aromatic rings of the polymer with respect to the hexagons that constitute the nanotube surface, and on the level of the global conformation of the polymer, which we characterise in terms of its radius of gyration.

5.5.1 Dihedral angles between graphene surface and polymer aromatic rings

To investigate the relative arrangement of polymer aromatic rings with respect to the graphene surface, we calculate the dihedral angles between the surface and the plane of the aromatic rings (Figure 5.15).

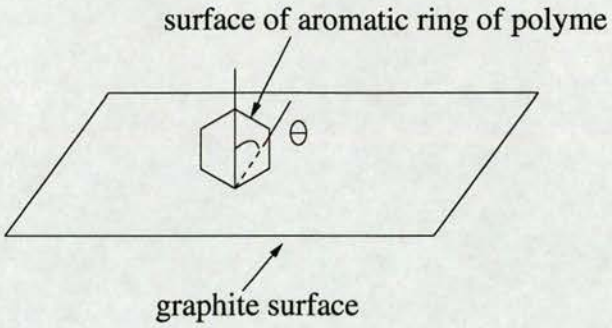

Figure 5.10: *Definition of the dihedral angle between the surface of graphene and the plane of a polymer aromatic ring*

The atomic configuration of the polymer was recorded in intervals of 1 ps during a simulation, and the dihedral angles between the planes of the polymer aromatic rings and the surface of the SWNT were determined as follows. To every aromatic ring on the polymer, we fit a plane function of the form

$$A_1x + B_1y + C_1z + D_1 = 0. \tag{5.1}$$

To the surface of graphene, we also fit a plane function of the form

$$A_2x + B_2y + C_2z + D_2 = 0. \tag{5.2}$$

The dihedral angle between the surface of the graphene and the plane of the polymer aromatic ring is then evaluated as

$$cos(\theta) = \frac{A_1A_2 + B_1B_2 + C_1C_2}{\sqrt{A_1^2 + B_1^2 + C_1^2}\sqrt{A_2^2 + B_2^2 + C_2^2}}. \tag{5.3}$$

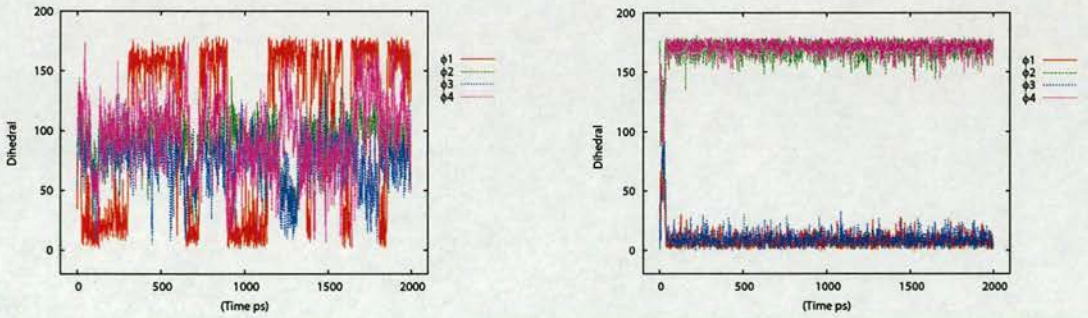

(a) (b)

Figure 5.11: *Dihedral between the surface of graphene and that of aromatic rings of polymer: (a)PS (4 repeating units, containing 4 aromatic rings), (b) PmPV (2 repeating units, containing 4 aromatic rings)*

We simulate the interaction between graphene and polymers. Both the PS and PmPV in the simulations contain 4 aromatic rings, the dihedral angles are denoted by $\theta 1$, $\theta 2$, $\theta 3$ and $\theta 4$ in order from one end to another end of polymer chains. Figure 5.11 shows variance of the dihedrals between graphene and polymers (PS and PmPV). The PS contains 4 aromatic rings. The dihedrals of PS vary very quickly all the time because PS has a σ bond on its backbone, which can rotate freely. The dihedrals of PmPV are quite stable apart from the beginning of the equilibrium procedure. Because PmPV has very strong interaction with graphene and its backbone is completely conjugated, its backbone to rotate will have to overcome a very high energy barrier, which is impossible within the short simulation time (2 ns).

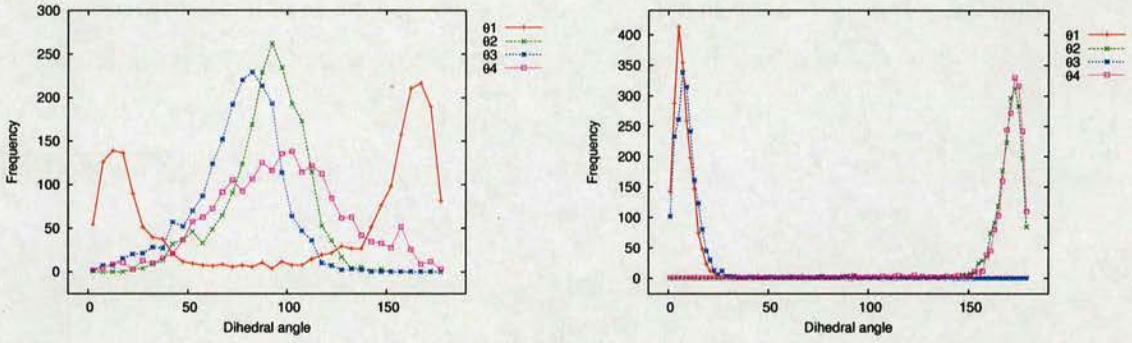

Figure 5.12: *Dihedral distribution: (a)PS (4 repeating units, containing 4 aromatic rings), (b) PmPV (2 repeating units, containing 4 aromatic rings)*

Furthermore, we can calculate the distribution of the dihedral angles. The result is shown in Figure 5.12. For PS, the dihedral between the first aromatic ring (in the first unit of PS) and the surface of graphene is around 0° or 180°, and the other dihedral angles are around 90°. The PmPV also contains 4 aromatic rings. All the dihedral angles between PmPV aromatic rings and the surface are around 0° or 180°. A dihedral equal to 0° or 180° means that the aromatic ring is parallel to the surface of graphene, while a dihedral equal to 90° means that the aromatic ring is perpendicular to the surface of graphene. Therefore, we can see that the aromatic rings of PS are mostly vertical to the graphene, while the aromatic rings of PmPV are mostly parallel to the graphene.

The dihedral angle distribution of longer polymers containing more such dihedrals is shown in Figure 5.13. It is evident that the length of the polymers has little influence on their alignment of polymers on the graphene surface. From the distributions of the dihedral angles, we can obtain the total probability distribution shown in Figure 5.14.

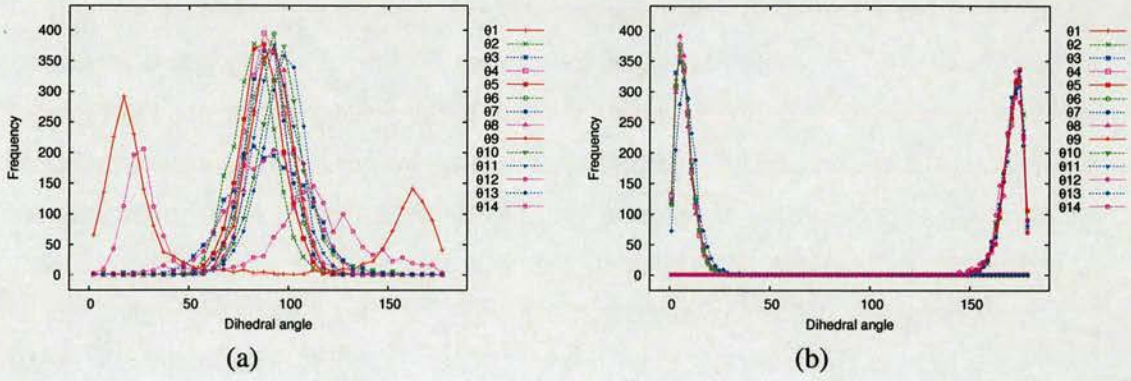

Figure 5.13: *Dihedral distribution: (a)PS (14 repeating units, containing 14 aromatic rings), (b) PmPV (7 repeating units, containing 14 aromatic rings)*

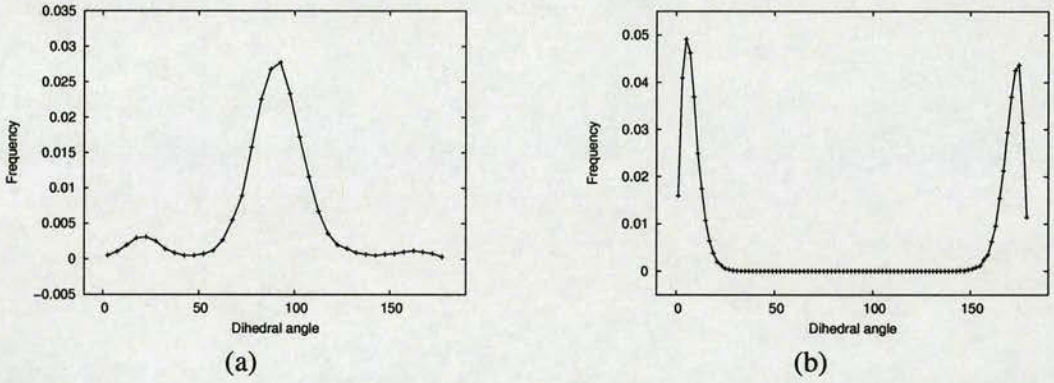

Figure 5.14: *Probability density of dihedral: (a)PS (14 repeating units, containing 14 aromatic rings), (b) PmPV (7 repeating units, containing 14 aromatic rings)*

5.5.2 Dihedral between surface of SWNT and that of polymer aromatic rings

The atomic arrangement of carbon nanotubes as that of graphene sheets, consists of hexagons. To measure a dihedral between an aromatic ring of a polymer and the surface of a SWNT, we first use the coordinates of the atoms of the aromatic ring to fit a plane function. Then, we determine the hexagon on the SWNT that is closest to the aromatic ring under consideration in terms of the distance between the centres of gravity, and we again fit another plane function.

We calculate the probability distribution of the dihedral angle in the same way as for the dihedral angles between polymer aromatic ring and graphene surface. The result is shown in Figure 5.16. It is seen that the dihedral angle distribution is like that for polymers interacting with graphene. Most of the dihedral angles of PS and PPA are distributed around 90°, while most of the dihedral angles of PmPV and PPV are distributed around 0° and 180°.

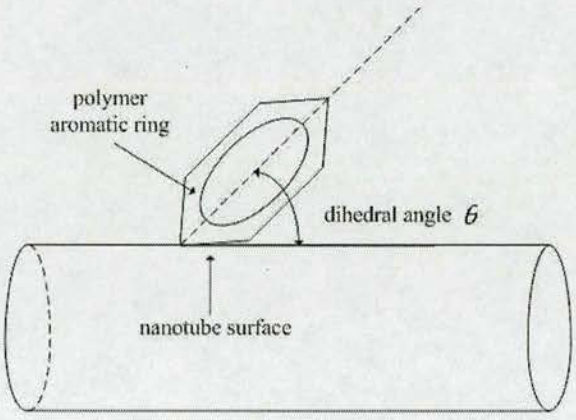

Figure 5.15: *Definition of the dihedral angle between the surface of a carbon nanotube and the plane of a polymer aromatic ring*

The polymers with aromatic rings on the backbone provide an instructive contrast to those with aromatic rings as side chains. Figure 5.16 shows that for the latter polymers (PS and PPA), the plane of the aromatic rings tends to be vertical to the surface of the SWNT, while for polymers with aromatic rings on the backbone (PmPV and PPV), these rings tend to align parallel to the nanotube surface. The different behaviour of the aromatic rings can be explained in terms of the overall polymer conformation. In case of PS and PPA, alignment of the polymer backbone parallel to the carbon nanotube surface is not compatible with surface alignment of the aromatic rings in the side chains (which then would require a significant twisting of bonds). The aromatic rings in the side chains instead rotate away from the carbon nanotube surface and align parallel to each other to optimise their mutual interaction. In PmPV and PPV, however, both the polymer backbone and aromatic rings in it align parallel to the surface, and this significantly increases the overall carbon nanotube-polymer interaction (cf. Figure 5.5). Such parallel stacking has been experimentally confirmed by atomic force microscopy (AFM) for a complex of the conjugated polymer and SWNT [118].

5.5.3 The change of mean radius of polymers

To characterise the effect of the adsorption on the overall size of the polymer, we use the change of its mean square root of gyration radius, R_g (mean radius change). The square of R_g equals the mean-square distance of the polymer atoms from the center of mass of the polymer chain,

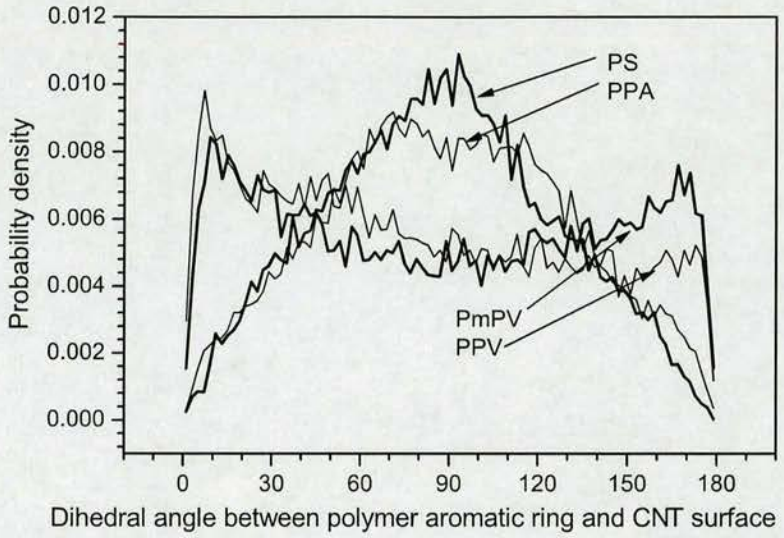

Figure 5.16: *Probability density of the dihedral between polymer aromatic ring and carbon nanotube surface*

$$\langle R_g^2 \rangle = \frac{1}{N} \langle \sum_{i=1}^{N} (\mathbf{r}_i - \mathbf{r}_c)^2 \rangle, \tag{5.4}$$

where $\mathbf{r}_i$ is the position of atom i, N is the number of atoms, and $\mathbf{r}_c$ is the center of gravity of the polymer.

From MD simulations of the polymers in the absence of carbon nanotubes, we determined the mean radius 6.64 Å for PS, 6.29 Å for PPA, 8.81 Å for PmPV, and 18.46 Å for PPV. We then calculated the change of the mean radius as the polymers interact with SWNT. Figure 5.17 shows the mean radius change as a function of SWNT diameter. It is clear that the mean radius of PmPV increases markedly as the flexible polymer backbone aligns well along the carbon nanotube. This increase becomes more pronounced with increasing SWNT diameter. A possible explanation for this observation is that the side chains "wrap" around the nanotube, which means that their contribution to the mean radius increases with increasing nanotube radius.

However, no significant increase in the mean radius is found for the other polymers. For PPV, the reason is the rigidity of the polymer backbone, which does not markedly "stretch out" when

aligning along the carbon nanotube surface. For PS and PPA, however, the change in radius is small because their general interaction with the carbon nanotube surface is weak and the polymer configurations remain almost unperturbed by the carbon nanotube.

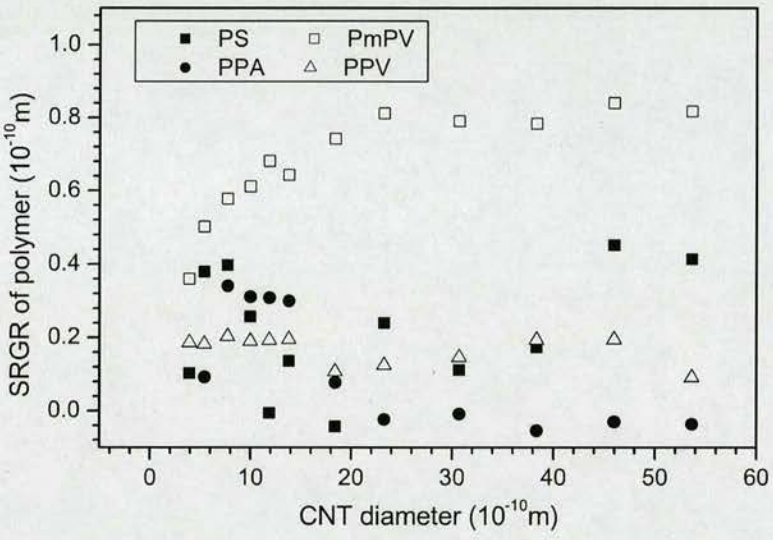

Figure 5.17: *Change of the mean radius after the interaction with a carbon nanotube*

5.6 "Wrapping" of SWNT by polymers

5.6.1 Simulation of interaction between SWNT and aggregated polymers

We denote as wrapping the enveloping of the surface of carbon nanotubes by polymers. As we know, polymers with aromatic rings on their backbone have strong interaction with carbon nanotubes. The same kind of isomorphism is responsible for the strong tendency of carbon nanotubes to "stick together", which provides a major obstacle to their processing. Polymer wrapping of carbon nanotubes has received attention as a means of preventing the carbon nanotubes from aggregating into bundles and thereby improving their dispersion into a composite matrix [15]. Polymer wrapping of carbon nanotubes may also be a promising way for manipulating and organising carbon nanotubes into ordered structures and even of their noncovalent functionalization. Recently, experiments [107, 111] have been reported for the wrapping of SWNT with PmPV, and Chen et al. [108] found that a molecule containing a planar phenyl group can irreversibly adsorb to the surface of a SWNT and successfully immobilise proteins,

DNA, and smaller biomolecules on the nanotube sidewalls.

5.6.2 Polymer wrapping of SWNT

We carry out a series of MD simulations to investigate the wrapping process. To assess the efficiency of polymer wrapping, we consider the competitive interaction between two aggregated polymer chains and a SWNT. Initially, we put two polymers of same kind close to each other and let the complex evolve for 2 ns. This leads to aggregation of the polymers due to their van der Waals interaction. Next, we place the aggregated polymers close to the wall of SWNT and run a MD simulation for another 3 ns.

Figure 5.18 shows snapshots of polymers and SWNT observed at different time steps of the simulation. In the beginning, the intertwisted polymers move toward the SWNT. For PmPV and PPV, which have aromatic rings on the backbone, these aromatic rings gradually align parallel to the nanotube surface; in this way, the polymer backbones separate from each other and assume conformations parallel to the long axis of the carbon nanotube. After 50 ps, the polymers wrapped on the surface of the SWNT and equilibrium was achieved, and the conformation of polymers around SWNT did not change much afterwards.

5.6.3 Intermolecular interaction between SWNT and aggregated polymers

The intermolecular energy between the polymers, and intermolecular energy between the polymers and the SWNT were monitored during the wrapping process. Figure 5.19 shows the intermolecular energy for PS, PPA, PmPV, and PPV. Initially, for all the polymers the intermolecular energy between the two polymer chains gradually deceases. For PPA, PmPV, and PPV, the interaction decreases almost to zero after a while, and the two chains become completely separated. For PS, however, the interaction between the polymers and the SWNT is not strong enough to separate the two polymer chains, which remain intertwisted all the time.

5.7 Summary

Our MD simulations of the interaction of PS, PPA, PmPV, and PPV with SWNT in a vacuum indicate that, although all these polymers exhibit obvious attractive interactions with carbon nanotubes, the interaction between SWNT and polymers is strongly influenced by the specific

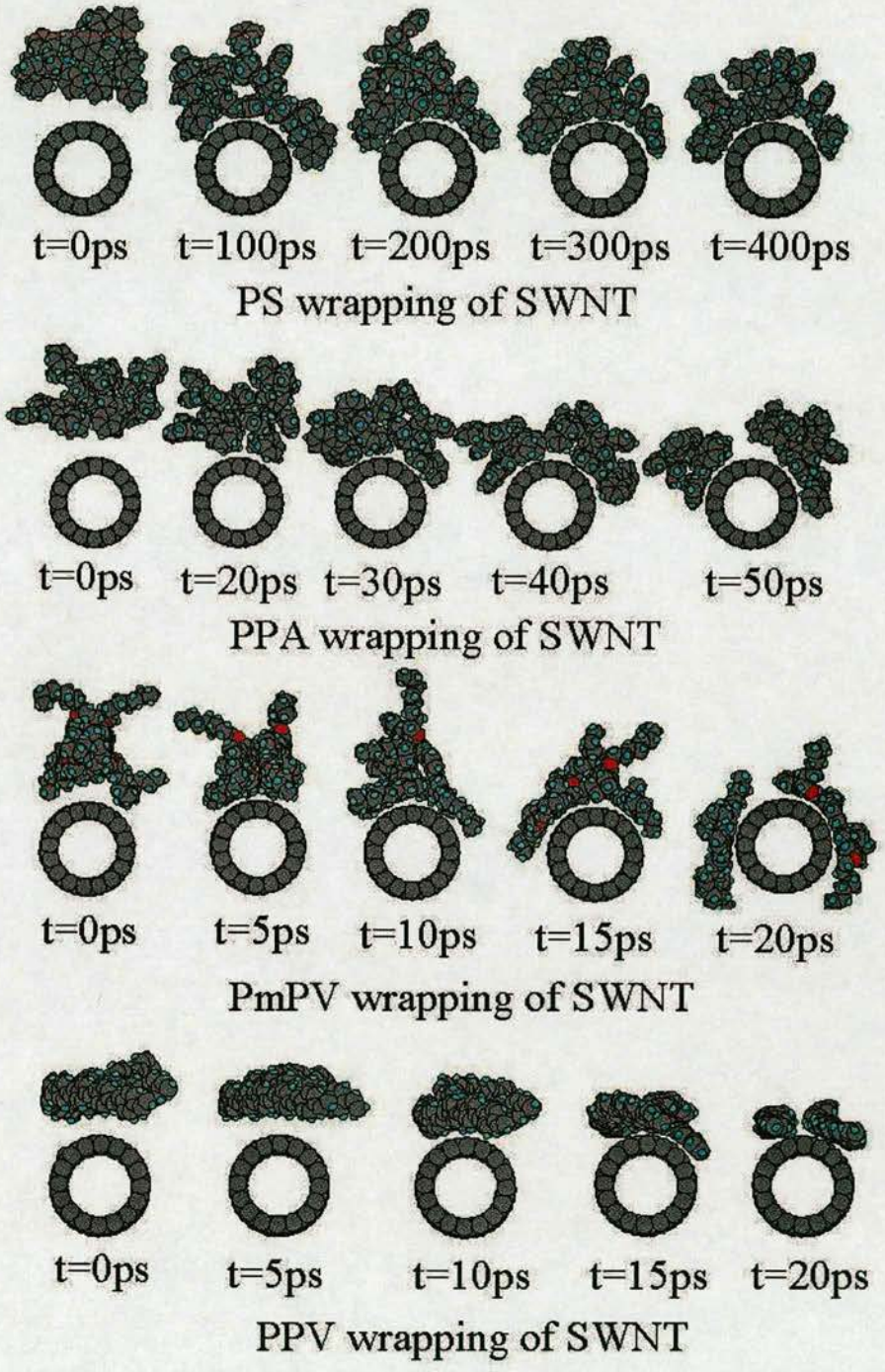

Figure 5.18: *MD simulation snapshots of the wrapping of a SWNT of 11.8 Å in diameter by different polymers (section view)*

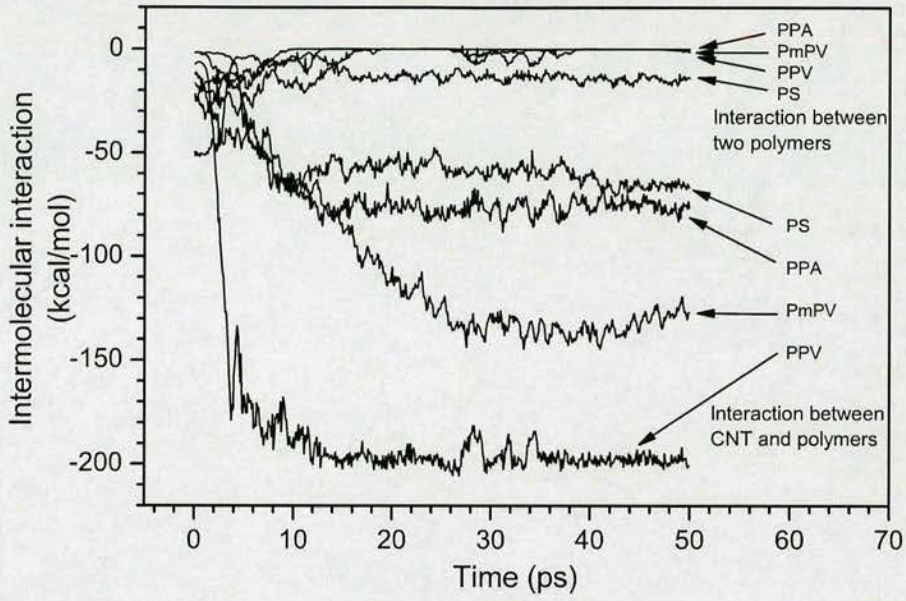

Figure 5.19: *Time evolution of polymer-polymer and polymers-carbon nanotube interactions during wrapping*

monomer structure of the polymers. For polymer chains of comparable molecular weight but different monomer structure, intermolecular interaction energies are found to differ by up to a factor of 4. Carbon nanotube-polymer interactions are the strongest for conjugated polymers with aromatic rings on the polymer backbone, as these rings are able to align parallel to the nanotube surface and thereby provide strong interfacial adhesion. In the presence of well-separated carbon nanotubes, different polymer chains get disentangled and align along the carbon nanotubes to cover the nanotube surface (wrapping). This is a general observation for all investigated polymers; however, the effect is most pronounced for PmPV, which combines certain flexibility in the backbone structure, flexible side chains, and strong interaction with the nanotube surface.

Chapter 6
Conclusions

This chapter briefly summaries the main results of this thesis, and the future directions on the subject are given and discussed.

6.1 Summary

6.1.1 Mechanical properties of SWNT with/without defects

We investigate mechanical properties of SWNT under axial loading, namely the Young's modulus of SWNT under axial tensile/compressive loading and buckling strength under axial compressive loading. The computational results indicate that the longitudinal Young's modulus decreases in inverse proportion with increasing nanotube diameter. We also investigate the influence of defects on the Young's modulus and buckling strength of SWNT. Three kinds of defects are studied: defects caused by chemical functionalization, topological defects (5-7-7-5 defects) and structural defects (vacancies). The results show that the Young's modulus of SWNT is but slightly influenced by these defects, while the buckling stress is greatly decreased. For SWNT with small diameters ($<$14 Å), the buckling strength is especially sensitive to defects, and the buckling strength of all the SWNT deteriorates with increasing defect concentration.

6.1.2 Size dependence of fracture strength of SWNT with defects

We investigate the size dependence of defected SWNT fracture strength under tensile loading. The size dependence of fracture strength is studied with extreme order statistics, and a relationship between the length of SWNT and their fracture strength is established. This study reasonably explains differences between fracture strengths measured in experiments (13 $\sim$ 52 GPa) and those from theoretical calculations on defect free carbon nanotubes ($\sim$ 250 GPa). The results also indicate that extreme order statistics may be an important tool for helping to understand the influence of defects on fracture strength of carbon nanotubes.

6.1.3 Interaction between SWNT and polymers

We investigate the interaction between SWNT and polymers. MD simulations of the interaction of PS, PPA, PmPV, and PPV with SWNT in a vacuum indicate that, although all these polymers exhibit obvious attractive interactions with carbon nanotubes, the interaction between SWNT and polymers is strongly influenced by the specific monomer structure of the polymers. For polymer chains of comparable molecular weight but different monomer structure, intermolecular interaction energies are found to differ by up to a factor of 4. Carbon nanotube-polymer interactions are the strongest for conjugated polymers with aromatic rings on the polymer backbone, as these rings are able to align parallel to the nanotube surface and thereby provide strong interfacial adhesion. In the presence of well-separated carbon nanotubes, different polymer chains get disentangled and align along the carbon nanotubes to cover the nanotube surface (wrapping). This is a general observation for all investigated polymers; however, the effect is most pronounced for PmPV, which combines certain flexibility in the backbone structure, flexible side chains, and strong interaction with the nanotube surface.

6.2 Future work

All the effort in this thesis is a part of systematic study on carbon nanotube-reinforced polymer composites. This is clearly not the end of the subject, and more experimental work is needed to validate the results from computer simulations. It also would be interesting to investigate the following areas with computer simulation:

6.2.1 Computer simulation of full-size defected carbon nanotubes

The carbon nanotubes we used in our study are very short (only 100 or 200 Å). Real carbon nanotubes can be 1000 times longer than this. Although we use extreme order statistics to extend the fracture strength distribution of defected carbon nanotubes from a small scale of 0.1 μm to a scale of 10 μm, some specific phenomena can not be observed. For example, "wire-like buckling", only happens to carbon nanotubes of large aspect ratio. For such purpose, it is necessary to study full-size carbon nanotubes, however, it is difficult to simulate long nanotubes since they may contain more than 100,000 atoms.

Continuum models have already been proposed to speed up such simulations. Continuum mod-

els of carbon nanotubes incorporate interaction potentials into continuum constitutive laws by homogenization through the Cauchy-Born rule and can reproduce the corresponding atomistic models with reasonable accuracy for smooth deformations. But most studies with these models are focused on mechanical properties of perfect nanotubes and the influence of defects is not considered. Continuum modes themselves are usually unable to deal with atomic defects. One possible way is to use molecular mechanics to investigate the defects of a nanotube, while continuum models are used for the remaining defect free parts, and with a multiscale method the two different methods are incorporated into one simulation. An effective multiscale method for linking atomistic scale and continuum elements would be the major issue in such a study.

6.2.2 Computer simulation of carbon nanotubes dispersion

Our study indicates that some polymers have strong attractive interaction with well-separated carbon nanotubes. However, the interaction between carbon nanotubes and polymers might not be strong enough to prevent carbon nanotubes from aggregating. The aggregation of carbon nanotubes will greatly damage their reinforcing ability in polymer composites. To functionalize carbon nanotubes chemically may improve their interaction strength with polymers but, as we indicated before, the defects introduced will greatly decrease the strength of the nanotubes, and, as a result, the composites can not be reinforced as well as we expected. Simulations of large nanotube-polymer aggregates would involve numerous molecules and may be problematic because of computational cost.

Since the focus of a study of nanotube reinforced polymers is not on local interaction between a nanotube and a matrix material, but on the effect of the global arrangement of the nanotubes in the polymer matrix, finite element simulation might play an important role in finding strategies for improving the dispersion of nanotubes into polymer matrices, and requisite constitutive properties describing the nanotubes can be derived from molecular simulations. Nanotubes can be presented with volume elements including the effects of the surrounding matrix material. In this study interfaces between the nanotubes and matrices might pose serious challenges to this method because at the nanoscale or microscale, the interface is not a continuous surface. Thus, simulation results near the interfaces should be interpreted carefully.

Appendix A
Ensembles and ensemble averages in MD simulations

A.1 Ensembles

An ensemble is a collection of systems which have different microscopic states but represent an identical macroscopic or thermodynamic state. There exist different ensembles with different characteristics.

- Microcanonical ensemble (NVE): The thermodynamic state characterized by a fixed number of atoms, N, a fixed volume, V, and a fixed energy, E. This corresponds to an ensemble of isolated systems.
- Canonical Ensemble (NVT): This is a collection of all systems whose thermodynamic state is characterized by a fixed number of atoms, N, fixed volume, V, and fixed temperature, T.
- Isobaric-Isothermal Ensemble (NPT): This ensemble is characterized by a fixed number of atoms, N, a fixed pressure, P, and a fixed temperature, T.
- Grand canonical Ensemble (μVT): The thermodynamic state for this ensemble is characterized by a fixed chemical potential, μ, a fixed volume, V, and fixed temperature, T.

The study of molecular properties as a function of temperature and pressure, rather than volume and energy, is of general importance. Thus, microcanonical ensembles are inappropriate for simulating certain systems which require constant pressure and/or temperature conditions and allow the energy and volume to fluctuate. In such cases, canonical ensembles (NVT), isobaric-isothermal ensembles (NPT) and grand canonical ensembles may be more appropriate.

A.2 Ensemble averages in MD simulations

In statistical mechanics, average values are defined as ensemble averages. The ensemble average is given by

$$\langle A \rangle_{ensemble} = \iint dp^N dr^N A\left(p^N, r^N\right) \rho\left(p^N, r^N\right) \tag{A.1}$$

where $A\left(p^N, r^N\right)$ is the observable of interest and it is expressed as a function of the momenta, p, and the positions, r, of the system. The integration is over all possible variable of r and p.

The probability density of the ensemble is given by

$$\rho\left(p^N, r^N\right) = \frac{1}{Q} \exp\left[-H\left(p^N, r^N\right)/k_B T\right] \tag{A.2}$$

where H is the Hamiltonian, T is the temperature, k_B is Boltzmann's constant and Q is the partition function

$$Q = \iint dp^N dr^N \exp\left[-H\left(p^N, r^N\right)/k_B T\right] \tag{A.3}$$

This integral is generally extremely difficult to calculate because one must evaluate all possible states of the system. In a molecular dynamics simulation, the points in the ensemble are calculated sequentially in time, so to calculate an ensemble average, the molecular dynamics simulations must pass through all possible states corresponding to the particular thermodynamic constraints.

Another way, as done in an MD simulation, is to determine a time average of A, which is expressed as

$$< A >_{time} = \lim_{\tau \to \infty} \frac{1}{\tau} \int_{t=0}^{\tau} A\left(p^N(t), r^N(t)\right) dt \approx \frac{1}{M} \sum_{t=1}^{M} A\left(p^N, r^N\right) \tag{A.4}$$

where τ is the simulation time, M is the number of time steps in the simulation and $A\left(p^N, r^N\right)$ is the instantaneous value of A.

The dilemma appears to be that one can calculate time averages by molecular dynamics simulation, but the experimental observables are assumed to be ensemble averages. Resolving this leads us to one of the most fundamental axioms of statistical mechanics, the ergodic hypothesis, which states that the time average equals the ensemble average.

$$< A >_{ensemble} = < A >_{time} \tag{A.5}$$

The basic idea is that if one allows the system to evolve in time indefinitely, that the system will eventually pass through all possible states. One goal, therefore, of a molecular dynamics simulation is to generate enough representative conformations such that this equality is satisfied. If this is the case, experimentally relevant information concerning structural, dynamic and thermodynamic properties may then be calculated using a feasible amount of computer resources. Because the simulations are of fixed duration, one must be certain to sample a sufficient amount of phase space. For example, average potential energy

$$V =< V >= \frac{1}{M} \sum_{i=1}^{M} V_i \tag{A.6}$$

where M is the number of configurations in the molecular dynamics trajectory and V_i is the potential energy of each configuration.

A molecular dynamics simulation must be sufficiently long so that enough representative conformations have been sampled.

Appendix B
Thermostat algorithms of molecular dynamics

A modification of the Newtonian MD scheme with the purpose of generating a thermodynamical ensemble at constant temperature is called a thermostat algorithm. The use of a thermostat algorithm requires the definition of an instantaneous temperature. This temperature will be compared to the reference temperature T_0 of the heat bath to which the system is coupled.

B.1 Andersen thermostat

The Andersen thermostat [54], also known as stochastic collision method, is able to generate a rigorous canonical ensemble. In this method, a particle is randomly chosen at intervals and its velocity is reassigned by random selection from the Maxwell-Boltzmann distribution. This is equivalent to the system being in a contact with a heat bath that randomly emits "thermal particles" which collide with the system and so the overall effect is equivalent to a series of microcanonical simulations, each performed at a slightly different energy. The distribution of the energies of these "mini microcanonical" simulations will be a Gaussian function. By calculating the energy change due to a collision, Andersen showed that the mean rate (ν) at which each particle should suffer a stochastic collision is given by:

$$\nu = \frac{2\alpha\kappa}{2k_B\rho^{1/3}N^{2/3}} \tag{B.1}$$

where α is a dimensionless constant, κ is the thermal conductivity,N is the number of the particles and ρ is the number density of the particles. If the thermal conductivity is not known then a suitable value of ν can be obtained from the intermolecular collision frequency ν_c:

$$\nu = \frac{\nu_c}{N^{2/3}} \tag{B.2}$$

If the collision rate is too low then the system does not sample from a canonical distribution of energies. If it is too high then the temperature control algorithm dominates and the system does

not show the expected fluctuations in kinetic energy.

B.2 Berendsen thermostat

The Berendsen thermostat [54] is a simple and popular method to control system temperature. In this method, the system is coupled to an external heat bath that is fixed at the desired temperature. The bath acts as a source of thermal energy, supplying or removing heat from the system as appropriate. The velocities are scaled at each step, such that the rate of change of temperature is proportional to the difference in temperature between the bath and the system:

$$\frac{dT(t)}{dt} = \frac{1}{\tau}\left[T_{bath} - T(t)\right] \tag{B.3}$$

τ is a coupling parameter whose magnitude determines how tightly the bath and the system are coupled. This method gives an exponential decay of the system towards the desired temperature. The change in temperature between successive time steps is

$$\Delta T = \frac{\delta t}{\tau}\left[T_{bath} - T(t)\right] \tag{B.4}$$

The scaling factor for the velocities is thus:

$$\lambda^2 = 1 + \frac{\delta t}{\tau}\left[\frac{T_{bath}}{T(t)} - 1\right] \tag{B.5}$$

If τ is large, then the coupling coupling will be weak. If τ is small, the coupling will be strong and when the coupling parameter equals the time step ($\tau = \delta t$) then the algorithm is equivalent to a simple velocity scaling method.

B.3 Nose-Hoover thermostat

The Nose-Hoover thermostat [66] introduces an additional degree of freedom into the system's Hamiltonian, for which equation of motion can be derived. These equations for the additional degrees of freedom are integrated together with "usual" equations for spatial coordinates and momenta to reduce the effect of an external system. Two sets of variables p_i, q_i and π_i, ρ_i are

introduced. These virtual variables are derived from the so-called Sundman's transformation:

$$s = \frac{d\tau}{dt} \tag{B.6}$$

where τ is the virtual time, t is the real time and s is the resulting scaling factor, which also treated as a dynamical variable. The transformation from the virtual variables π_i, ρ_i to the real ones p_i, q_i is performed according to:

$$p_i = \pi_i; q_i = \rho_i \tag{B.7}$$

The introduction of the effective mass M_s connects also a momentum to the additional degree of freedom π_s. The resulting Hamiltonian, expressed in terms of the virtual coordinates can be written as:

$$H^* = \sum_{i=1}^{N} \frac{\pi_i^2}{2ms} + U(\rho_1, \rho_2, \ldots, \rho_N) + \frac{\pi_s^2}{2M_s} + gk_bT\ln(s) \tag{B.8}$$

where $g = 3N + 1$ is the number degrees of freedom of the extended system(N particles $+1$ the new degree of freedom). It was shown, that this Hamiltonian H^* leads to a density of probability in phase space, corresponding to the canonical ensemble.

The equations of motion obtained from the Hamiltonian are:

$$\frac{d\vec{\rho}_i}{d\tau} = \frac{\partial H^*}{\partial \vec{\pi}_i} = \frac{\vec{\pi}_i}{ms^2} \tag{B.9}$$

$$\frac{d\vec{\rho}_i}{d\tau} = -\frac{\partial H^*}{\partial \vec{\rho}_i} = -\frac{\partial U}{\partial \vec{\rho}_i} \tag{B.10}$$

$$\frac{ds}{d\tau} = \frac{\partial H^*}{\partial \rho_s} = \frac{\pi_s}{M_s} \tag{B.11}$$

$$\frac{d\pi_s}{d\tau} = -\frac{\partial H^*}{\partial s} = \frac{gk_bT}{s} + \sum_{i=1}^{N} \frac{\pi_i^2}{2ms} \tag{B.12}$$

Then we obtain

$$\frac{d\vec{q}_i}{dt} = \frac{\vec{p}_i}{m_i} \tag{B.13}$$

$$\frac{d\vec{p}_i}{d\tau} = -\frac{\partial U}{\partial \vec{q}_i} - \zeta \vec{p}_i \tag{B.14}$$

$$\frac{\partial \ln(s)}{\partial t} = \zeta \tag{B.15}$$

$$\frac{d\zeta}{dt} = \frac{1}{M_s}\left(\sum_{i=1}^{N} \frac{p_i^2}{2m_i} - gk_bT\right); p_i \equiv |\vec{p}_i| \tag{B.16}$$

These equations describe the Nose-Hoover thermostat. The parameter M_s is a thermal inertia parameter, which determines rate of the heat transfer. The value of this parameter must be set carefully, because if it is chosen to be too small the phase space of the system will not be canonical, and it is chosen to be too large the temperature control will not be efficient.

Appendix C
Molecular simulation packages

In our simulation, we mainly use TINKER with MM3 force field and Brenner's code with REBO potential (Brenner's potential) to implement our simulations. The official home page for the TINKER code is located at `http://dasher.wustl.edu/tinker/`, and there is also a detailed guide on how to use it. For Brenner's code, the source code can be obtained from the website:
`http://www.bayesianinvestor.com/brenner/` but there is no formal documentation. However, useful information about the code can be obtained from the website:
`http://www.eng.fsu.edu/~dommelen/research/nano/brenner/index.html`[1]

TINKER was developed by the Department of Biochemistry and Molecular Biophysics, Washington University, School of Medicine. Like other open source codes, it is free and the user has access to its source code, which makes it a desirable tool for research. TINKER is designed to be an easily used and flexible system of programs and routines for molecular mechanics and dynamics as well as other energy-based and structural manipulation calculations. Rather than incorporating all the functionality in one monolithic program, TINKER provides a set of relatively small programs that interoperate to perform complex computations.

C.1 The TINKER simulation package

Totally, there are more than 50 programs in TINKER packages. We will talk about several programs frequently used in our simulations.

- **analyze**

  This program provides information about a specific molecular structure (.xyz file). The user also supplies the type of analysis. Optional outputs including: (1) total potential

[1] All the information is correct as of September 2005

energy of the system, (2) breakdown of the energy by potential function type or over individual atoms, (3) computation of the total dipole moment and its components, moments of inertia and radius of gyration, (4) listing of the parameters used to compute selected interaction energies, (5) energies associated with specified individual interactions.

- **dynamic**

  This program performs a MD computation. It starts either from a specified input molecular structure (.xyz file) or from a structure-velocity-acceleration set saved from a previous dynamics trajectory (.dyn file). MD trajectories are propagated using either a modified Beeman or a velocity Verlet integration method. Coordinate sets of molecular system along the trajectory can be saved as sequentially numbered cycle files or directly to a TINKER archive (.arc file).

- **minimize**

  This program performs a minimization of an input structure over Cartesian coordinates. The user supplies coordinates of molecular system (.xyz file) and a target rms gradient value at which the minimization will terminate. Output consists of minimization statistics written to the screen or redirected to an output file, and the new coordinates written to updated structure files (.xyz files) or to cycle files.

- **xyzedit**

  This program performs a variety of manipulations on an input structure (.xyz file). It has a lot of interactively selectable options including deleting or inserting atoms, appending another .xyz file to current one, and assigning connectivities based on distance, etc. Multiply options can be applied sequentially to an input file. At the end of the editing process, a new version of the original coordinate set (.xyz file) is written as output.

The most important file in TINKER is the keyword parameter file, which always has the extension ".key". It contains values for any of a wide variety of switches and parameters that are used to change the course of the computation from the default. All programs of TINKER look first for a key file, and in the absence of a key file will query the user for needed information. The keywords in a key file can reset a wide variety of algorithmic and procedural options. Some options are often used in simulations:

- ***cutoff***

  This keyword sets the cutoff distance value for all nonbonded potential energy interac-

tions. The energy for any of the nonbonded potentials of a pair of sites beyond the cutoff distance will be set to zero.

- ***group***

  This keyword defines an atom group as a substructure within a molecular structure. Together with keywords ***group-inter*** or ***group-intra***, it can only calculate inter-group or intra-group interactions. For example, if we calculate the interaction between a carbon nanotube and a polymer, we can use the keyword ***group*** to define two groups, one for the carbon nanotube, another for the polymer, and together with keyword ***group-inter***. With these contents in keyword file we can use program **analyze** to calculate the total potential energy of the carbon nanotube and the polymer, which actually is the interaction energy between the carbon nanotube and the polymer.

- ***inactive***

  This keyword sets the list of inactive atoms during a TINKER computation. Individual potential energy terms are not computed when all atoms involved in the term are inactive. The Cartesian coordinates of inactive atoms are not allowed to change.

- ***parameters***

  This keyword provides the name of the force field parameter file to be used for a TINKER calculation. For example, if MM3 force field is used, we should set the parameter value to "mm3".

- ***restrain-position***

  This keyword provides the ability to restrain an individual atom to a specified coordinate position with a harmonic restraint force.

- ***thermostat***

  This keyword selects a thermostat algorithm for use during molecular dynamics. Three modifier are available corresponding to Berendsen bath coupling, Andersen stochastic collision, and Nose-Hoover extended dynamics methods.

The detailed usages of these program and keywords are included in the *user's guide* of TINKER: `http://dasher.wustl.edu/tinker/guide.html`

C.2 Brenner's code

Brenner's code is developed by D.W. Brenner, J.A. Harrison S.B. Sinnott and O. Shenderova [61]. It includes a suite of molecular dynamics and interatomic force routines. The user supplies two files with this computation program. The first is the structure file (coord.d) and the second a parameter file (input.d). The structure file gives the coordinates of the atoms, and the parameter file specifies the parameters controlling computation. The parameter file reads as follows:

1000 1 6 1 / # steps, # steps between data, thermostat, xmol writes — *first line*

0.6955 0.500 0.0 / Random # seed, neighbor list , temperature(K) — *second line*

1 / =1 REBO (C,H,Si,Ge), =2 tight-binding for C — *third line*

6 12.0 51.2 2.28 / carbon Lennard-Jones parameters — *fourth line*

1 1.0 8.6 2.81 / hydrogen

-14 28.0 51.2 2.28 / silicon = carbon

-10 20.0 47.0 2.72 / Neon

-18 40.0 119.8 3.41 / Argon

-36 131.0 164.0 3.83 / Krypton

In every line, the contents after "/" are ignored by the program, and have nothing to do with the computation.

In first line of the parameter file, the first parameter is the total number of time steps to take, the second parameter specifies the number of steps to take before doing basic output, and the third parameter is used to chose the thermostat algorithm, which we set to 6 since we only use molecular mechanics to minimize the energy of a system. In this case of energy minimization, the first two parameters in the first line don't have any influence on the computation.

In the second line, the first parameter is the random seed for the random number generator in the program, the second is the allowed maximum displacement of the atoms before we rebuild the neighborhood list of all atoms (neighborhood list is used to speed-up the calculation of interactions of the atoms). The third parameter is the temperature in Kelvin, at which the user implements molecular dynamics simulation.

In the third line, there is selection of potential: set to 1 for REBO (Brenner's potential); set to 2 for tight-binding.

The rest of the parameter file specifies atom number (type), atom mass, and two parameters for VDW interaction. If the first character is '-', the parameter in this line is commented, not used in simulation.

References

[1] S. Iijima, "Helical microtubules of graphitic carbon," *Nature*, vol. 354, no. 6348, pp. 56–58, 1991.

[2] D. Qian, G. J. Wagner, W. K. Liu, M.-F. Yu, and R. S. Ruoff, "Mechanics of carbon nanotubes," *Applied Mechanics Reviews*, vol. 55, no. 6, p. 495, 2002.

[3] M. S. Dresselhaus, G. Dresselhaus, and R. Saito, "Physics of carbon nanotubes," *Carbon*, vol. 33, no. 7, p. 883, 1995.

[4] J. W. Mintmire, B. I. Dunlap, and C. T. White, "Are fullerene tubules metallic," *Physical Review Letters*, vol. 68, no. 5, pp. 631–634, 1992.

[5] R. Saito, M. Fujita, G. Dresselhaus, and M. S. Dresselhaus, "Electronic structure of chiral graphene tubules," *Applied Physics Letters*, vol. 60, no. 18, p. 2204, 1992.

[6] J. W. Mintmire and C. T. White, "Electronic and structural properties of carbon nanotubes," *Carbon*, vol. 33, no. 7, p. 893, 1995.

[7] J. W. G. Wilder, L. C. Venema, A. G. Rinzler, R. E. Smalley, and C. Dekker, "Electronic structure of atomically resolved carbon nanotubes," *Nature*, vol. 391, no. 6662, p. 59, 1998.

[8] T. W. Odom, J.-L. Huang, P. Kim, and C. M. Lieber, "Atomic structure and electronic properties of single-walled carbon nanotubes," *Nature*, vol. 391, no. 6662, p. 62, 1998.

[9] X. Tang, A. Kleinhammes, H. Shimoda, L. Fleming, K. Y. Bennoune, S. Sinha, C. Bower, O. Zhou, and Y. Wu, "Electronic structures of single-walled carbon nanotubes determined by nmr," *Science*, vol. 288, no. 5465, pp. 492–4, 2000.

[10] P. G. Collins, M. S. Arnold, and P. Avouris, "Engineering carbon nanotubes and nanotube circuits using electrical breakdown," *Science*, vol. 292, no. 5517, pp. 706–9, 2001.

[11] M. Ouyang, J.-L. Huang, C. L. Cheung, and C. M. Lieber, "Energy gaps in "metallic" single-walled carbon nanotubes," *Science*, vol. 292, no. 5517, pp. 702–705, 2001.

[12] L. F. Sun, S. S. Xie, W. Liu, W. Y. Zhou, Z. Q. Liu, D. S. Tang, G. Wang, and L. X. Qian, "Materials: Creating the narrowest carbon nanotubes," *Nature*, vol. 403, no. 6768, p. 384, 2000.

[13] L. C. Qin, X. Zhao, K. Hirahara, Y. Miyamoto, Y. Ando, and S. Iijima, "The smallest carbon nanotube," *Nature*, vol. 408, no. 6808, p. 50, 2000.

[14] X. Zhao, Y. Liu, S. Inoue, T. Suzuki, R. O. Jones, and Y. Ando, "Smallest carbon nanotube is 3 a in diameter," *Phys Rev Lett*, vol. 92, no. 12, p. 125502, 2004.

[15] Y. L. Li, I. A. Kinloch, and A. H. Windle, "Direct spinning of carbon nanotube fibers from chemical vapor deposition synthesis," *Science*, vol. 304, no. 5668, pp. 276–8, 2004.

[16] H. Dai, "Carbon nanotubes: synthesis, integration, and properties," *Acc Chem Res*, vol. 35, no. 12, pp. 1035–44, 2002.

[17] Y. Ando and S. Iijima, "Preparation of carbon nanotubes by arc-discharge evaporation," *Japanese Journal of Applied Physics, Part 2: Letters*, vol. 32, no. 1A-B, pp. 107–109, 1993.

[18] P. M. Ajayan, "Nanotubes from carbon," *Chem Rev*, vol. 99, no. 7, pp. 1787–1800, 1999.

[19] Z. F. Ren, Z. P. Huang, J. W. Xu, J. H. Wang, P. Bush, M. P. Siegal, and P. N. Provencio, "Synthesis of large arrays of well-aligned carbon nanotubes on glass," *Science*, vol. 282, no. 5391, pp. 1105–7, 1998.

[20] P. Mauron, C. Emmenegger, A. Zuttel, C. Nutzenadel, P. Sudan, and L. Schlapbach, "Synthesis of oriented nanotube films by chemical vapor deposition," *Carbon*, vol. 40, no. 8, p. 1339, 2002.

[21] H. Liao and J. H. Hafner, "Low-temperature single-wall carbon nanotube synthesis by thermal chemical vapor deposition," *Journal of Physical Chemistry B*, vol. 108, no. 22, p. 6941, 2004.

[22] R. Andrews, D. Jacques, D. Qian, and T. Rantell, "Multiwall carbon nanotubes: synthesis and application," *Acc Chem Res*, vol. 35, no. 12, pp. 1008–17, 2002.

[23] C. Journet, W. K. Maser, P. Bernier, A. Loiseau, M. L. de la Chapelle, S. Lefrant, P. Deniard, R. Lee, and J. E. Fischer, "Large-scale production of single-walled carbon nanotubes by the electric-arc technique," *Nature*, vol. 388, no. 6644, p. 756, 1997.

[24] A. Thess, R. Lee, P. Nikolaev, H. Dai, P. Petit, J. Robert, C. Xu, Y. H. Lee, S. G. Kim, A. G. Rinzler, D. T. Colbert, G. E. Scuseria, D. Tomanek, J. E. Fischer, and R. E. Smalley, "Crystalline ropes of metallic carbon nanotubes," *Science*, vol. 273, no. 5274, pp. 483–7, 1996.

[25] K. Hata, D. N. Futaba, K. Mizuno, T. Namai, M. Yumura, and S. Iijima, "Water-assisted highly efficient synthesis of impurity-free single-walled carbon nanotubes," *Science*, vol. 306, no. 5700, pp. 1362–4, 2004.

[26] H. W. Zhu, C. L. Xu, D. H. Wu, B. Q. Wei, R. Vajtai, and P. M. Ajayan, "Direct synthesis of long single-walled carbon nanotube strands," *Science*, vol. 296, no. 5569, pp. 884–6, 2002.

[27] L. M. Ericson, H. Fan, H. Peng, V. A. Davis, W. Zhou, J. Sulpizio, Y. Wang, R. Booker, J. Vavro, C. Guthy, A. N. Parra-Vasquez, M. J. Kim, S. Ramesh, R. K. Saini, C. Kittrell, G. Lavin, H. Schmidt, W. W. Adams, W. E. Billups, M. Pasquali, W. F. Hwang, R. H. Hauge, J. E. Fischer, and R. E. Smalley, "Macroscopic, neat, single-walled carbon nanotube fibers," *Science*, vol. 305, no. 5689, pp. 1447–50, 2004.

[28] Q. Zhao, M. B. Nardelli, and J. Bernholc, "Ultimate strength of carbon nanotubes: A theoretical study," *Physical Review B (Condensed Matter and Materials Physics)*, vol. 65, no. 14, p. 144105, 2002.

[29] M. M. J. Treacy, T. W. Ebbesen, and J. M. Gibson, "Exceptionally high young's modulus observed for individual carbon nanotubes," *Nature*, vol. 381, no. 6584, pp. 678–680, 1996.

[30] P. Poncharal, Z. L. Wang, D. Ugarte, and W. A. de Heer, "Electrostatic deflections and electromechanical resonances of carbon nanotubes," *Science*, vol. 283, no. 5407, pp. 1513–6, 1999.

[31] A. Krishnan, E. Dujardin, T. W. Ebbesen, P. N. Yianilos, and M. M. J. Treacy, "Young's modulus of single-walled nanotubes," *Physical Review B*, vol. 58, no. 20, pp. 14013–14019, 1998.

[32] E. W. Wong, P. E. Sheehan, and C. M. Lieber, "Nanobeam mechanics: Elasticity, strength, and toughness of nanorods and nanotubes," *Science Science*, vol. 277, no. 5334, pp. 1971–1975, 1997.

[33] M. F. Yu, B. S. Files, S. Arepalli, and R. S. Ruoff, "Tensile loading of ropes of single wall carbon nanotubes and their mechanical properties," *Phys Rev Lett*, vol. 84, no. 24, pp. 5552–5, 2000.

[34] M. F. Yu, O. Lourie, M. J. Dyer, K. Moloni, T. F. Kelly, and R. S. Ruoff, "Strength and breaking mechanism of multiwalled carbon nanotubes under tensile load," *Science*, vol. 287, no. 5453, pp. 637–40, 2000.

[35] O. Zhou, R. M. Fleming, D. W. Murphy, C. H. Chen, R. C. Haddon, A. P. Ramirez, and S. H. Glarum, "Defects in carbon nanostructures," *Science*, vol. 263, no. 5154, pp. 1744–1747, 1994.

[36] B. I. Yakobson, C. J. Brabec, and J. Bernholc, "Nanomechanics of carbon tubes: Instabilities beyond linear response," *Physical Review Letters Phys. Rev. Lett.*, vol. 76, no. 14, pp. 2511–2514, 1996.

[37] M. R. Falvo, G. J. Clary, I. Taylor, R. M., V. Chi, J. Brooks, F. P., S. Washburn, and R. Superfine, "Bending and buckling of carbon nanotubes under large strain," *Nature*, vol. 389, no. 6651, p. 582, 1997.

[38] O. Lourie, D. M. Cox, and H. D. Wagner, "Buckling and collapse of embedded carbon nanotubes," *Physical Review Letters*, vol. 81, no. 8, pp. 1638–1641, 1998.

[39] C. Wang, C. Ru, and A. Mioduchowski, "Axially compressed buckling of pressured multiwall carbon nanotubes," *International Journal of Solids and Structures*, vol. 40, no. 15, p. 868, 2003.

[40] L. Sudak, "Column buckling of multiwalled carbon nanotubes using nonlocal continuum mechanics," *Journal of Applied Physics*, vol. 94, no. 11, p. 7281, 2003.

[41] A. Pantano, M. C. Boyce, and D. M. Parks, "Nonlinear structural mechanics based modeling of carbon nanotube deformation," *Phys Rev Lett*, vol. 91, no. 14, p. 145504, 2003.

[42] Y. Wang, X. Wang Xiu, and X. Ni, "Atomistic simulation of the torsion deformation of carbon nanotubes," 2004.

[43] Q. Han and G. Lu, "Torsional buckling of a double-walled carbon nanotube embedded in an elastic medium," *European Journal of Mechanics, A/Solids*, vol. 22, no. 6, p. 875, 2003.

[44] M. Buehler, K. Yong, and G. Huajian, "Deformation mechanisms of very long single-wall carbon nanotubes subject to compressive loading," *Transactions of the ASME. Journal of Engineering Materials and Technology*, vol. 126, no. 3, p. 245, 2004.

[45] A. Sears and R. Batra, "Macroscopic properties of carbon nanotubes from molecular-mechanics simulations," *Physical Review B (Condensed Matter and Materials Physics)*, vol. 69, no. 23, p. 235406, 2004.

[46] M. Ouyang, J. L. Huang, C. L. Cheung, and C. M. Lieber, "Atomically resolved single-walled carbon nanotube intramolecular junctions," *Science*, vol. 291, no. 5501, pp. 97–100, 2001.

[47] D. Qian, E. C. Dickey, R. Andrews, and T. Rantell, "Load transfer and deformation mechanisms in carbon nanotube- polystyrene composites," *Applied Physics Letters*, vol. 76, no. 20, pp. 2868–2870, 2000.

[48] D. B. Mawhinney, V. Naumenko, A. Kuznetsova, J. T. Yates Jr., J. Liu, and R. E. Smalley, "Surface defect site density on single walled carbon nanotubes by titration," *Chemical Physics Letters*, vol. 324, no. 1-3, pp. 213–216, 2000.

[49] J. C. Charlier, P. Lambin, and T. W. Ebbesen, "Electronic properties of carbon nanotubes with polygonized cross sections," *Physical Review B Phys. Rev. B*, vol. 54, no. 12, pp. R8377–R8380, 1996.

[50] M. B. Nardelli, J. L. Fattebert, D. Orlikowski, C. Roland, Q. Zhao, and J. Bernholc, "Mechanical properties, defects and electronic behavior of carbon nanotubes," *Carbon Carbon*, vol. 38, no. 11-12, pp. 1703–1711, 2000.

[51] S. A. Curran, A. V. Ellis, A. Vijayaraghavan, and P. M. Ajayan, "Functionalization of carbon nanotubes using phenosafranin," *J Chem Phys*, vol. 120, no. 10, pp. 4886–9, 2004.

[52] C. A. Dyke and J. M. Tour, "Solvent-free functionalization of carbon nanotubes," *J Am Chem Soc*, vol. 125, no. 5, pp. 1156–7, 2003.

[53] J. Zhu, J. Kim, H. Peng, J. L. Margrave, V. N. Khabashesku, and E. V. Barrera, "Improving the dispersion and integration of single-walled carbon nanotubes in epoxy composites through functionalization," *Nano Letters*, vol. 3, no. 8, p. 1107, 2003.

[54] A. R. Leach, *Molecular Modelling: Principles and Applications*. Harlow: Addison Wesley Longman Limited, 1996.

[55] N. L. Allinger, Y. H. Yuh, and J. H. Lii, "Molecular mechanics - the mm3 force-field for hydrocarbons.1," *Journal of the American Chemical Society*, vol. 111, no. 23, pp. 8551–8566, 1989.

[56] G. C. Abell, "Empirical chemical pseudopotential theory of molecular and metallic bonding," *Physical Review B*, vol. 31, no. 10, pp. 6184–6196, 1985.

[57] J. Tersoff, "New empirical-model for the structural-properties of silicon," *Physical Review Letters*, vol. 56, no. 6, pp. 632–635, 1986.

[58] J. Tersoff, "New empirical-approach for the structure and energy of covalent systems," *Physical Review B*, vol. 37, no. 12, pp. 6991–7000, 1988.

[59] J. Tersoff, "Empirical interatomic potential for carbon, with applications to amorphous-carbon," *Physical Review Letters*, vol. 61, no. 25, pp. 2879–2882, 1988.

[60] D. W. Brenner, "Empirical potential for hydrocarbons for use in simulating the chemical vapor-deposition of diamond films," *Physical Review B*, vol. 42, no. 15, pp. 9458–9471, 1990.

[61] D. W. Brenner, O. A. Shenderova, J. A. Harrison, S. J. Stuart, B. Ni, and S. B. Sinnott, "A second-generation reactive empirical bond order (rebo) potential energy expression for hydrocarbons," *Journal of Physics: Condensed Matter*, no. 4, p. 783, 2002.

[62] D. Xie and T. Schlick, "Efficient implementation of the truncated-Newton algorithm for large-scale chemistry applications," *SIAM Journal on Optimization*, vol. 10, pp. 132 – 154, NOV 29 1999.

[63] T. Schlick, *Molecular Modeling and Simulation An Interdisciplinary Guide*. New York: Springer, 2002.

[64] D. Beeman, "Some multistep methods for use in molecular-dynamics calculations," *Journal Of Computational Physics*, vol. 20, no. 2, pp. 130–139, 1976.

[65] J. Grotendorst, D. Marx, and A. Muramatsu, *Quantum Simulations of Complex Many-Body Systems: From Theory to Algorithms*, vol. 10 of *NIC Series*. John von Neumaan Institute for Computing, Julich, 2002.

[66] D. J. Evans and B. L. Holian, "The nose–hoover thermostat," *The Journal of Chemical Physics*, vol. 83, no. 8, pp. 4069–4074, 1985.

[67] J. Tersoff and R. S. Ruoff, "Structural properties of a carbon-nanotube crystal," *Physical Review Letters*, vol. 73, no. 5, pp. 676–679, 1994.

[68] Y. Ma, Y. Xia, M. Zhao, M. Ying, X. Liu, and P. Liu, "Collision of hydrogen atom with single-walled carbon nanotube: Adsorption, insertion, and healing," *The Journal of Chemical Physics*, vol. 115, no. 17, pp. 8152–8156, 2001.

[69] S.-P. Chan, G. Chen, X. G. Gong, and Z.-F. Liu, "Chemisorption of hydrogen molecules on carbon nanotubes under high pressure," *Physical Review Letters*, vol. 87, no. 20, p. 205502, 2001.

[70] Z. H. Yao, C. C. Zhu, M. Cheng, and J. H. Liu, "Mechanical properties of carbon nanotube by molecular dynamics simulation," *Computational Materials Science*, vol. 22, no. 3-4, pp. 180–184, 2001.

[71] T. Hertel, R. E. Walkup, and P. Avouris, "Deformation of carbon nanotubes by surface van der waals forces," *Physical Review B*, vol. 58, no. 20, pp. 13870–13873, 1998.

[72] V. Lordi and N. Yao, "Molecular mechanics of binding in carbon-nanotube-polymer composites," *Journal of Materials Research*, vol. 15, no. 12, pp. 2770–2779, 2000.

[73] Z. Y. Liang, J. H. Gou, C. Zhang, B. Wang, and L. Kramer, "Investigation of molecular interactions between (10,10) single- walled nanotube and epon 862 resin/detda curing agent molecules," *Materials Science and Engineering a-Structural Materials Properties Microstructure and Processing*, vol. 365, no. 1-2, pp. 228–234, 2004.

[74] X. Gao and K. Li, "Finite deformation continuum model for single-walled carbon nanotubes," *International Journal of Solids and Structures*, vol. 40, no. 26, p. 7329, 2003.

[75] T. Natsuki, K. Tantrakarn, and M. Endo, "Prediction of elastic properties for single-walled carbon nanotubes," *Carbon*, vol. 42, no. 1, p. 39, 2004.

[76] A. Rochefort, P. Avouris, F. Lesage, and D. R. Salahub, "Electrical and mechanical properties of distorted carbon nanotubes," *Physical Review B*, vol. 60, no. 19, pp. 13824–13830, 1999.

[77] A. Rochefort, "Electronic and transport properties of carbon nanotube peapods," *Physical Review B*, vol. 67, no. 11, p. 115401, 2003.

[78] M. Cote, J. C. Grossman, M. L. Cohen, and S. G. Louie, "Theoretical study of a three-dimensional all-sp(2) structure," *Physical Review B*, vol. 58, no. 2, pp. 664–668, 1998.

[79] Y. Kong and J. W. Ponder, "Calculation of the reaction field due to off-center point multipoles," *Journal of Chemical Physics*, vol. 107, no. 2, pp. 481–492, 1997.

[80] L. X. Shen and J. Li, "Transversely isotropic elastic properties of single-walled carbon nanotubes," *Physical Review B*, vol. 69, no. 4, p. 045414, 2004.

[81] Y. Jin and F. G. Yuan, "Simulation of elastic properties of single-walled carbon nanotubes," *Composites Science and Technology*, vol. 63, no. 11, pp. 1507–1515, 2003.

[82] C. Bower, R. Rosen, L. Jin, J. Han, and O. Zhou, "Deformation of carbon nanotubes in nanotube-polymer composites," *Applied Physics Letters*, vol. 74, pp. 3317–3319, May 31 1999.

[83] T. W. Ebbesen and T. Takada, "Topological and sp3 defect structures in nanotubes," *Carbon*, vol. 33, no. 7, p. 973, 1995.

[84] H. J. Choi, J. Ihm, S. G. Louie, and M. L. Cohen, "Defects, quasibound states, and quantum conductance in metallic carbon nanotubes," *Phys Rev Lett*, vol. 84, no. 13, pp. 2917–20, 2000.

[85] J. C. Charlier, "Defects in carbon nanotubes," *Acc Chem Res*, vol. 35, no. 12, pp. 1063–9, 2002.

[86] M. P. Mattson, R. C. Haddon, and A. M. Rao, "Molecular functionalization of carbon nanotubes and use as substrates for neuronal growth," *J Mol Neurosci*, vol. 14, no. 3, pp. 175–82, 2000.

[87] J. L. Bahr, J. Yang, D. V. Kosynkin, M. J. Bronikowski, R. E. Smalley, and J. M. Tour, "Functionalization of carbon nanotubes by electrochemical reduction of aryl diazonium salts: a bucky paper electrode," *J Am Chem Soc*, vol. 123, no. 27, pp. 6536–42, 2001.

[88] M. Holzinger, O. Vostrowsky, A. Hirsch, F. Hennrich, M. Kappes, R. Weiss, and F. Jellen, "Sidewall functionalization of carbon nanotubes this work was supported by the european union under the 5th framework research training network 1999, hprnt 1999-00011 funcars," *Angew Chem Int Ed Engl*, vol. 40, no. 21, pp. 4002–4005, 2001.

[89] K. Fu, W. Huang, Y. Lin, D. Zhang, T. W. Hanks, A. M. Rao, and Y. P. Sun, "Functionalization of carbon nanotubes with bovine serum albumin in homogeneous aqueous solution," *J Nanosci Nanotechnol*, vol. 2, no. 5, pp. 457–61, 2002.

[90] X. Lu, F. Tian, N. Wang, and Q. Zhang, "Organic functionalization of the sidewalls of carbon nanotubes by diels-alder reactions: a theoretical prediction," *Org Lett*, vol. 4, no. 24, pp. 4313–5, 2002.

[91] H. Peng, L. B. Alemany, J. L. Margrave, and V. N. Khabashesku, "Sidewall carboxylic acid functionalization of single-walled carbon nanotubes," *J Am Chem Soc*, vol. 125, no. 49, pp. 15174–82, 2003.

[92] M. Grujicic, G. Cao, and R. Singh, "The effect of topological defects and oxygen adsorption on the electronic transport properties of single-walled carbon-nanotubes," *Applied Surface Science*, vol. 211, no. 1-4, p. 166, 2003.

[93] A. J. Lu and B. C. Pan, "Nature of single vacancy in achiral carbon nanotubes," *Phys Rev Lett*, vol. 92, no. 10, p. 105504, 2004.

[94] G. N. Hassold and D. J. Srolovitz, "Brittle-fracture in materials with random defects," *Physical Review B*, vol. 39, no. 13, pp. 9273–9281, 1989.

[95] C. Lu, R. Danzer, and F. D. Fischer, "Fracture statistics of brittle materials: Weibull or normal distribution," *Physical Review E (Statistical, Nonlinear, and Soft Matter Physics)*, vol. 65, no. 6, pp. 067102–4, 2002.

[96] S. Frankland, V. Harik, G. Odegard, D. Brenner, and T. Gates, "The stress-strain behavior of polymer-nanotube composites from molecular dynamics simulation," *Composites Science and Technology*, vol. 63, no. 11, p. 1655, 2003.

[97] G. Odegard, T. Gates, K. Wise, C. Park, and E. Siochi, "Constitutive modeling of nanotube-reinforced polymer composites," *Composites Science and Technology*, vol. 63, no. 11, p. 1671, 2003.

[98] A. A. Mamedov, N. A. Kotov, M. Prato, D. M. Guldi, J. P. Wicksted, and A. Hirsch, "Molecular design of strong single-wall carbon nanotube/polyelectrolyte multilayer composites," *Nat Mater*, vol. 1, no. 3, pp. 190–4, 2002.

[99] A. B. Dalton, S. Collins, E. Munoz, J. M. Razal, V. H. Ebron, J. P. Ferraris, J. N. Coleman, B. G. Kim, and R. H. Baughman, "Super-tough carbon-nanotube fibres," *Nature*, vol. 423, no. 6941, p. 703, 2003.

[100] D. Hull and T. W. Clyne, *An introduction to composite materials*. Cambridge: Cambridge University Press, 2nd ed. ed., 1996.

[101] M. Wong, M. Paramsothy, X. Xu, Y. Ren, S. Li, and K. Liao, "Physical interactions at carbon nanotube-polymer interface," *Polymer*, vol. 44, no. 25, p. 7757, 2003.

[102] H. Daniel Wagner, "Nanotube-polymer adhesion: a mechanics approach," *Chemical Physics Letters*, vol. 361, no. 1-2, p. 57, 2002.

[103] Z. G. Mao, A. Garg, and S. B. Sinnott, "Molecular dynamics simulations of the filling and decorating of carbon nanotubules," *Nanotechnology*, vol. 10, no. 3, pp. 273–277, 1999.

[104] B. Z. Tang and H. Y. Xu, "Preparation, alignment, and optical properties of soluble poly(phenylacetylene)-wrapped carbon nanotubes," *Macromolecules*, vol. 32, no. 8, pp. 2569–2576, 1999.

[105] K. Liao and S. Li, "Interfacial characteristics of a carbon nanotube-polystyrene composite system," *Applied Physics Letters*, vol. 79, no. 25, pp. 4225–4227, 2001.

[106] M. J. O'Connell, P. Boul, L. M. Ericson, C. Huffman, Y. H. Wang, E. Haroz, C. Kuper, J. Tour, K. D. Ausman, and R. E. Smalley, "Reversible water-solubilization of single-walled carbon nanotubes by polymer wrapping," *Chemical Physics Letters*, vol. 342, no. 3-4, pp. 265–271, 2001.

[107] D. W. Steuerman, A. Star, R. Narizzano, H. Choi, R. S. Ries, C. Nicolini, J. F. Stoddart, and J. R. Heath, "Interactions between conjugated polymers and single-walled carbon nanotubes," *Journal of Physical Chemistry B*, vol. 106, no. 12, pp. 3124–3130, 2002.

[108] R. J. Chen, Y. G. Zhan, D. W. Wang, and H. J. Dai, "Noncovalent sidewall functionalization of single-walled carbon nanotubes for protein immobilization," *Journal of the American Chemical Society*, vol. 123, no. 16, pp. 3838–3839, 2001.

[109] E. Kymakis and G. A. J. Amaratunga, "Single-wall carbon nanotube/conjugated polymer photovoltaic devices," *Applied Physics Letters*, vol. 80, no. 1, pp. 112–114, 2002.

[110] J. Kim, "Assemblies of conjugated polymers. intermolecular and intramolecular effects on the photophysical properties of conjugated polymers," *Pure And Applied Chemistry*, vol. 74, no. 11, pp. 2031–2044, 2002.

[111] A. Star, J. F. Stoddart, D. Steuerman, M. Diehl, A. Boukai, E. W. Wong, X. Yang, S. W. Chung, H. Choi, and J. R. Heath, "Preparation and properties of polymer-wrapped single-walled carbon nanotubes," *Angew Chem Int Ed Engl*, vol. 40, no. 9, pp. 1721–1725, 2001.

[112] A. B. Dalton, C. Stephan, J. N. Coleman, B. McCarthy, P. M. Ajayan, S. Lefrant, P. Bernier, W. J. Blau, and H. J. Byrne, "Selective interaction of a semiconjugated organic polymer with single-wall nanotubes," *Journal of Physical Chemistry B*, vol. 104, no. 43, pp. 10012–10016, 2000.

[113] J. Chen, H. Y. Liu, W. A. Weimer, M. D. Halls, D. H. Waldeck, and G. C. Walker, "Noncovalent engineering of carbon nanotube surfaces by rigid, functional conjugated polymers," *Journal Of The American Chemical Society*, vol. 124, no. 31, pp. 9034–9035, 2002.

[114] B. McCarthy, J. N. Coleman, R. Czerw, A. B. Dalton, M. I. H. Panhuis, A. Maiti, A. Drury, P. Bernier, J. B. Nagy, B. Lahr, H. J. Byrne, D. L. Carroll, and W. J. Blau, "A microscopic and spectroscopic study of interactions between carbon nanotubes and a conjugated polymer," *Journal of Physical Chemistry B*, vol. 106, no. 9, pp. 2210–2216, 2002.

[115] Q. Li, M. Zaiser, and V. Koutsos, "Carbon nanotube/epoxy resin composites using a block copolymer as a dispersing agent," *Physica Status Solidi a Applied Research*, vol. 201, no. 13, pp. R89–R91, 2004.

[116] W. Smith and T. R. Forester, "Dl_poly_2.0: A general-purpose parallel molecular dynamics simulation package," *Journal of Molecular Graphics*, vol. 14, no. 3, pp. 136–141, 1996.

[117] J. W. Ponder and F. M. Richards, "An efficient newton-like method for molecular mechanics energy minimization of large molecules," *Journal of Computational Chemistry*, vol. 8, no. 7, pp. 1016–1024, 1987.

[118] E. S. Steigerwalt and C. M. Lukehart, "Preparation of graphitic carbon nanofibers with the use of water-soluble supports," *J Nanosci Nanotechnol*, vol. 2, no. 1, pp. 25–8, 2002.